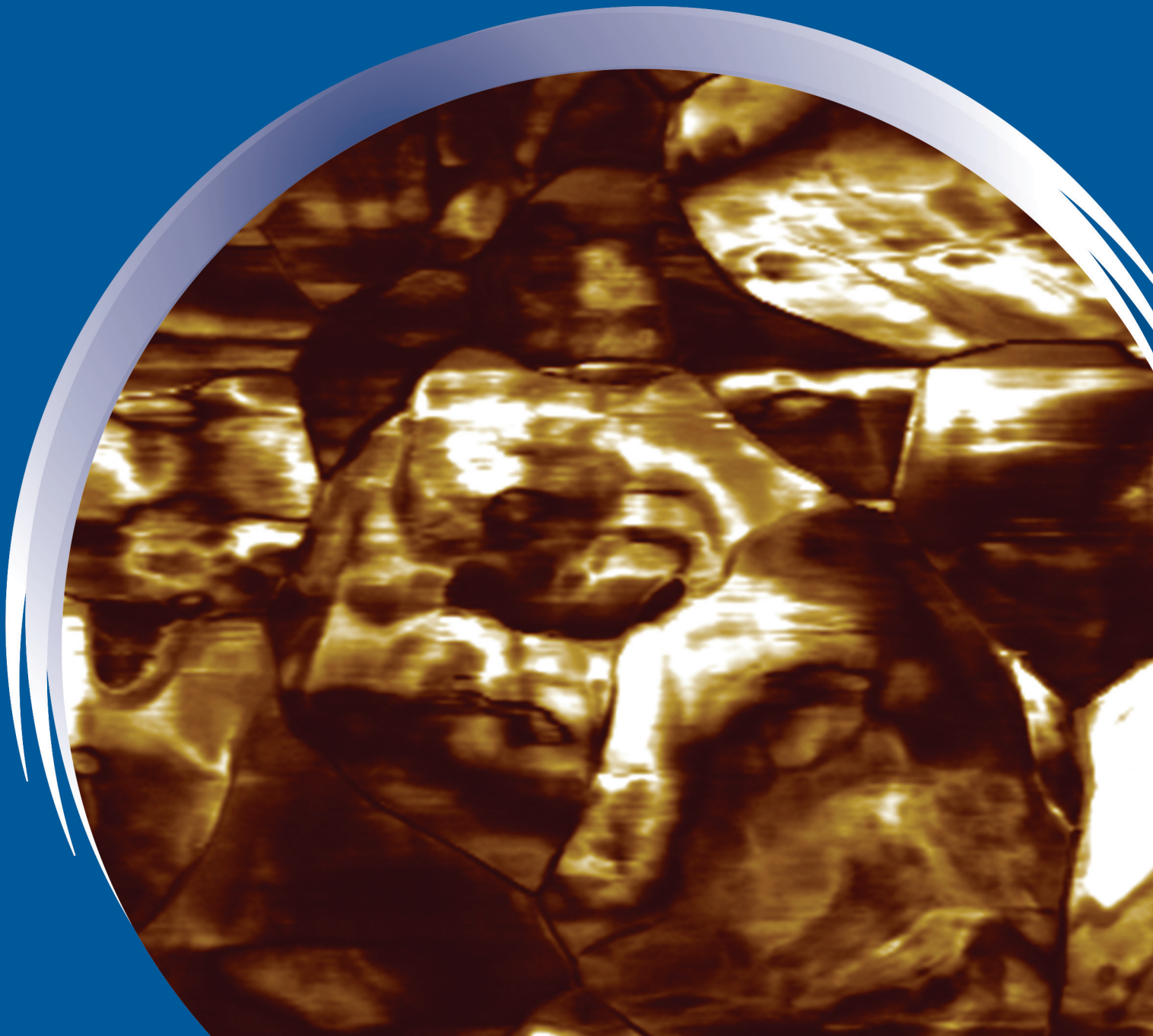


ISSN 0352-9045

# *Informacije* MIDEM

*Journal of Microelectronics,  
Electronic Components and Materials*  
**Vol. 47, No. 2(2017), June 2017**

*Revija za mikroelektroniko,  
elektronske sestavne dele in materiale*  
**letnik 47, številka 2(2017), Junij 2017**



# Informacije MIDEM 2-2017

Journal of Microelectronics, Electronic Components and Materials

VOLUME 47, NO. 2(162), LJUBLJANA, JUNE 2017 | LETNIK 47, NO. 2(162), LJUBLJANA, JUNIJ 2017

Published quarterly (March, June, September, December) by Society for Microelectronics, Electronic Components and Materials - MIDEM.  
Copyright © 2016. All rights reserved. | Revija izhaja trimesečno (marec, junij, september, december). Izdaja Strokovno društvo za mikroelektroniko, elektronske sestavne dele in materiale – Društvo MIDEM. Copyright © 2016. Vse pravice pridržane.

## Editor in Chief | Glavni in odgovorni urednik

Marko Topič, University of Ljubljana (UL), Faculty of Electrical Engineering, Slovenia

## Editor of Electronic Edition | Urednik elektronske izdaje

Kristijan Brecl, UL, Faculty of Electrical Engineering, Slovenia

## Associate Editors | Odgovorni področni uredniki

Vanja Ambrožič, UL, Faculty of Electrical Engineering, Slovenia

Arpad Bürmen, UL, Faculty of Electrical Engineering, Slovenia

Danjela Kuščer Hrovatin, Jožef Stefan Institute, Slovenia

Matija Pirc, UL, Faculty of Electrical Engineering, Slovenia

Matjaž Vidmar, UL, Faculty of Electrical Engineering, Slovenia

## Editorial Board | Uredniški odbor

Mohamed Akil, ESIEE PARIS, France

Giuseppe Buja, University of Padova, Italy

Gian-Franco Dalla Betta, University of Trento, Italy

Martyn Fice, University College London, United Kingdom

Ciprian Iliescu, Institute of Bioengineering and Nanotechnology, A\*STAR, Singapore

Malgorzata Jakubowska, Warsaw University of Technology, Poland

Marc Lethiecq, University of Tours, France

Teresa Orłowska-Kowalska, Wrocław University of Technology, Poland

Luca Palmieri, University of Padova, Italy

## International Advisory Board | Časopisni svet

Janez Trontelj, UL, Faculty of Electrical Engineering, Slovenia - Chairman

Cor Claeys, IMEC, Leuven, Belgium

Denis Donlagič, University of Maribor, Faculty of Elec. Eng. and Computer Science, Slovenia

Zvonko Fazarinc, CIS, Stanford University, Stanford, USA

Leszek J. Golonka, Technical University Wrocław, Wrocław, Poland

Jean-Marie Haussonne, EIC-LUSAC, Octeville, France

Barbara Malič, Jožef Stefan Institute, Slovenia

Miran Mozetič, Jožef Stefan Institute, Slovenia

Stane Pejovnik, UL, Faculty of Chemistry and Chemical Technology, Slovenia

Giorgio Pignatelli, University of Perugia, Italy

Giovanni Soncini, University of Trento, Trento, Italy

Iztok Šorli, MIKROIKS d.o.o., Ljubljana, Slovenia

Hong Wang, Xi'an Jiaotong University, China

## Headquarters | Naslov uredništva

Uredništvo Informacije MIDEM

MIDEM pri MIKROIKS

Stegne 11, 1521 Ljubljana, Slovenia

T. +386 (0)1 513 37 68

F. + 386 (0)1 513 37 71

E. info@midem-drustvo.si

www.midem-drustvo.si

Annual subscription rate is 160 EUR, separate issue is 40 EUR. MIDEM members and Society sponsors receive current issues for free. Scientific Council for Technical Sciences of Slovenian Research Agency has recognized Informacije MIDEM as scientific Journal for microelectronics, electronic components and materials. Publishing of the Journal is cofinanced by Slovenian Research Agency and by Society sponsors. Scientific and professional papers published in the journal are indexed and abstracted in COBISS and INSPEC databases. The Journal is indexed by ISI® for Sci Search®, Research Alert® and Material Science Citation Index™. |

Letna naročnina je 160 EUR, cena posamezne številke pa 40 EUR. Člani in sponzorji MIDEM prejema posamezne številke brezplačno. Znanstveni svet za tehnične vede je podal pozitivno mnenje o reviji kot znanstveno-strokovni reviji za mikroelektroniko, elektronske sestavne dele in materiale. Izdajo revije sofinancirajo ARRS in sponzorji društva. Znanstveno-strokovne prispevke objavljene v Informacijah MIDEM zajemamo v podatkovne baze COBISS in INSPEC. Prispevke iz revije zajema ISI® v naslednje svoje produkte: Sci Search®, Research Alert® in Materials Science Citation Index™.

## Content | Vsebina

### Original scientific paper

### Izvirni znanstveni članki

A. Pajkanović, M. Videnović-Misić, G. M. Stojanović: Design and Characterization of a 130 nm CMOS Ultra-Wideband Low-Noise Amplifier	59	A. Pajkanović, M. Videnović-Misić, G. M. Stojanović: Načrtovanje in karakterizacija 130 nm CMOS širokopasovnega ojačevalnika z nizkim šumom
H. Uršič, A. Benčan, E. Khomyakova, S. Drnovšek, I. F. Mercioniu, K. Makarovič, D. Belavič, C. Schreiner, R. Ciobanu, P. Fanjul Bolado, B. Malič: Pb(Mg,Nb)O <sub>3</sub> -PbTiO <sub>3</sub> Thick Films on Metalized Low-temperature Co-fired Ceramic Substrates	71	H. Uršič, A. Benčan, E. Khomyakova, S. Drnovšek, I. F. Mercioniu, K. Makarovič, D. Belavič, C. Schreiner, R. Ciobanu, P. Fanjul Bolado, B. Malič: Debele plasti Pb(Mg,Nb)O <sub>3</sub> -PbTiO <sub>3</sub> na podlagah iz keramike z nizko temperature žganja
D. Šekuljica, S. Badessi, M. Ferrante, M. Vidmar: Considerations about the use of the Moon in X-band antenna G/T measurements	79	D. Šekuljica, S. Badessi, M. Ferrante, M. Vidmar: Ugotovitve o uporabi Lune pri G/T meritvah antenskih sistemov frekvenčnega pasu X.
A. Amsaveni, P.T Vanathi: Reversible Data Hiding Based on Radon and Integer Lifting Wavelet Transform	91	A. Amsaveni, P.T Vanathi: Reverzibilno skrivanje podatkov na osnovi Radonove in diskretne valčne transformacije
S. M. Kahar, V. C. Hong, L. C. Chuan, S. C B Gopinath, M. K. Md Arshad, L. B. Ying, F. K. Loong, U. Hashim, Y. Al-Douri: Synthesis of Silicon Carbide Nanowhiskers by Mi- crowave Heating: Effect of Heating Temperature	101	S. M. Kahar, V. C. Hong, L. C. Chuan, S. C B Gopinath, M. K. Md Arshad, L. B. Ying, F. K. Loong, U. Hashim, Y. Al-Douri: Sinteza nanodlačic iz silicijevega karbida z mikrov- alovnim segrevanjem: Vpliv temperature gretja
T. Saje, M. Vidmar: A Compact Radio Telescope for the 21 cm Neutral-Hydrogen Line	113	T. Saje, M. Vidmar: Radioteleskop za 21 cm vodikovo črto
M. Lešnik, D. Verhovšek, N. Veronovski, S. Gatarič, M. Drogenik, J. Kovač: Highly Efficient Photocatalytic Activity in the Visible Region in Hydrothermally Synthesized N-doped TiO <sub>2</sub>	129	M. Lešnik, D. Verhovšek, N. Veronovski, S. Gatarič, M. Drogenik, J. Kovač: Hidrotermalno sintentiziran TiO <sub>2</sub> dopiran z N z visoko fotokatalitsko aktivnostjo v vidnem delu svetlobnega spektra
Doctoral theses on Microelectronics, Electronic Components and Materials in Slovenia in 2016	139	Doktorske disertacije na področju mikroelektronike, elektronskih sestavnih delov in materialov v Sloveniji v letu 2016
Announcement and Call for Papers: 53 <sup>rd</sup> International Conference on Microelectronics, Devices and Materials With the Workshop on Materials for Energy Conversion and Their Applications	143	Napoved in vabilo k udeležbi: 53. Mednarodna konferenca o mikroelektroniki, napravah in materialih z delavnico o materialih za pretvorbo energije in njihovih aplikacijah
Front page: Local piezoelectric response of the 0.65Pb(Mg <sub>1/3</sub> Nb <sub>2/3</sub> )O <sub>3</sub> -0.35PbTiO <sub>3</sub> thick film determined by piezo-response force microscope (H. Uršič et al.)		Naslovnica: Lokalni piezoelektrični odziv debele plasti 0.65Pb(Mg <sub>1/3</sub> Nb <sub>2/3</sub> )O <sub>3</sub> -0.35PbTiO <sub>3</sub> določen z mikroskopom na atomsko silo s piezoelektričnim modulom (H. Uršič et al.)





# Design and Characterization of a 130 nm CMOS Ultra-Wideband Low-Noise Amplifier

Aleksandar Pajkanović<sup>1,2</sup>, Mirjana Videnović-Misić<sup>2</sup>, Goran M. Stojanović<sup>2</sup>

<sup>1</sup>Faculty of Electrical Engineering, University of Banja Luka, Bosnia and Herzegovina

<sup>2</sup>Faculty of Technical Sciences, University of Novi Sad, Serbia

**Abstract:** The design of an ultra-wideband low noise amplifier is presented in this paper. Schematic level design is described, as well as integrated circuit layout techniques applied and post-layout simulation results. After fabrication using the standard 130 nm CMOS process node, on-chip characterization has been performed. The simulation and characterization results are presented analyzed and discussed in detail.

**Keywords:** CMOS integrated circuits (IC); analog/radio-frequency (RF); ultra-wideband (UWB); low-noise amplifier (LNA); on-chip characterization

## Načrtovanje in karakterizacija 130 nm CMOS širokopasovnega ojačevalnika z nizkim šumom

**Izvleček:** Članek obravnava ultra širokopasoven ojačevalnik z nizkim šumom. Predstavljena je shema, uporabljene tehnike integracijskega vezja in rezultati simulacij. Po izdelavi v standardni 130 nm CMOS tehnologiji je bila opravljena karakterizacija na nivoju čipa. Predstavljeni so simulacijski in karakterizacijski rezultati.

**Ključne besede:** CMOS integrirana vezja; analogna radio frekvenca (RF); ultra široki pas (UWB); ojačevalnik z nizkim šumom (LNA); karakterizacija na čipu

\*Corresponding Author's e-mail: [aleksandar.pajkanovic@etf.unibl.org](mailto:aleksandar.pajkanovic@etf.unibl.org)

### 1 Introduction

Different applications employing ultra-wideband (UWB) systems are under investigation in the lower frequency range of radio-frequencies (RF), which is around 1-10 GHz [1]. Such applications of interest include high resolution radars [2], medical imaging [3], communication systems [4] and many more. Physical layer in common for all these implementations employs UWB signals which are characterized with high relative bandwidths, wider than in any other standard commercialized until now [5]. This possesses plenty of new challenges for the RF integrated circuit (IC) designers in an already complex engineering environment [6, 7].

UWB signal is defined in [1] as either a signal of absolute bandwidth ( $B$ ) larger than 500 MHz, or a signal of relative bandwidth larger than 20 %, where relative bandwidth ( $B_r$ ) is calculated as follows:

$$B_r = \frac{f_u - f_d}{f_c} \quad (1)$$

where  $f_u$ ,  $f_d$  and  $f_c$  represent upper and lower band limit, and a central frequency, respectively. Documents defining frequency ranges, emissions and other UWB regulations were released in the United States first in 2002 [8] and in EU, Japan, Korea, Singapore and China since. UWB technology may, thus, utilize a frequency range of up to of 3.1-10.6 GHz. The whole range of 7.5 GHz is used only in the USA. In EU, the UWB band is divided in two sub-bands: lower (3.168-4.752 GHz) and higher (6.336-8.976 GHz). In Japan the sub-bands are given as: lower (3.696-4.752 GHz) and higher (7.392-10.032 GHz), while Korea and China have their own specifications. Other important UWB technology regulations

include its applications' definitions, such as indoor, outdoor, portable, fixed installed; data speeds of up to 480 Mb/s; and maximum emission levels, i.e. power spectral density (PSD) measured in terms of equivalent isotropically radiated power (EIRP). Moreover, in some of the mentioned sub-bands, e.g. lower EU sub-band, interference mitigation techniques are obligatory. As a consequence of such stringent regulations, total emitted power allowed is very low, and equal to  $-41.3$  dBm/MHz. In the case of the full allowed specter (3.1-10.6 GHz), this means that the total transmitted power may not be greater than 0.56 mW. Therefore, commercial UWB transmission is limited to short range applications [1, 5].

To exploit these frequency ranges, there are two approaches to the design of UWB communication systems: impulse radio (IR), which is shown in Figure 1a, and orthogonal frequency division multiplexing (OFDM), which is shown in Figure 1b. In the former case, the transmission is based on ultra-short pulses, thus covering the whole available band or sub-band. In the latter case, the available UWB bandwidth is divided into a set of wideband OFDM channels [1]. IR-UWB technique is more appropriate for applications where simple modulation schemes, such as on-off keying, provide enough signal integrity and offer higher energy efficiency and lower cost [9].

Regardless of the system architecture, the front-end wideband low noise amplifier (LNA) is obligatory as the first stage of the receiver [5], Figure 1. Such amplifier must meet several stringent requirements, e.g. broadband input matching, sufficient gain with wide bandwidth, low noise figure, etc. [5, 10]. For the past decade CMOS represents standard technology in the RF IC domain [11, 12, 13].

For the design presented in this paper, a standard eight-metal layer, 130 nm CMOS technology node was chosen. A variety of MOS devices are available, including low- and high-threshold versions, devices operating at higher supply voltages (3.3 V) and devices intended for RF application. For circuit implementation presented within this paper RF MOS transistors are chosen, their nominal supply voltage (VDD) and transition frequency ( $f_t$ ) being 1.2 V and 105 GHz, respectively. In general, the transistors are capable for appropriate performance at frequencies up to 10 % of  $f_t$  [14]. This means that UWB applications are feasible utilizing the MOS devices available within the selected process node. Additional advantage of this particular process node, in the context of RF IC design, is the availability of standard inductors. These are implemented in metal layer 8 and are all of spiral topology, either circular or rectangular, their inductance ranging from 100 pH up to 10 nH.

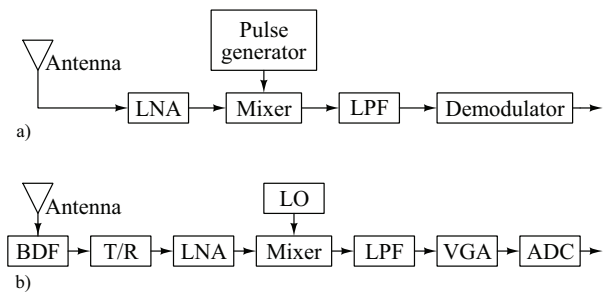


**Figure 1:** Two UWB communication system architectures [5]: a) IR and b) OFDM

In section 2 we provide a short introduction on figures of merit utilized within this paper for the LNA performance characterization. Then, in section 3 a brief overview of the related work is given. In the sections that follow, we present an LNA designed to operate in the EU UWB upper sub-band (69 GHz). The schematic level design procedure is described in section 4. The characterization procedure and the results obtained are presented in section 5. In section 6 the results characterized and simulated are analyzed and discussed, whereas in section 7 a conclusion follows.

## 2 Figures of Merit

In order to specify design requirements of an UWB amplifier, one is to use similar notions to those used when specifying a narrowband amplifier [14], such as gain, noise figure and input matching. However, the main difference is that these features must be achieved over a bandwidth of up to 10 GHz [1]. For example, according to Bode-Fano criterion [15], it is not possible to achieve arbitrary low reflection coefficient  $\Gamma(\omega)$  in the arbitrary wide bandwidth, if there is a reactive component in the load. That is the reason why wideband amplifiers must show higher reflection coefficient than their narrowband counterparts with the same transistor dimensions. This means that the information on any of those specifications in the context of RF IC is complete only if given over a range of frequencies. Furthermore, since these frequencies in the case of UWB applications extend well into microwave spectrum, we employ some figures of merit used in microwave engineering [11, 16] to precisely specify and, later on, characterize the LNA performance. Of course, different parameter values represent a standard in UWB case [17].

### 2.1 Scattering parameters

For a high frequency and broad bandwidth characterization of a two port network a two-by-two scattering (S) parameters matrix is used [11, 16]:

$$S = \begin{bmatrix} S_{11} & S_{12} \\ S_{21} & S_{22} \end{bmatrix}. \quad (2)$$

Each of the matrix members in equation (2) has physical meaning:

$S_{11}$  – input reflection coefficient,

$S_{12}$  – reverse transmission,

$S_{21}$  – a sort of gain [16], as it relates output wave to input wave,

$S_{22}$  – output reflection coefficient.

Normally, in the case of a LNA, the reflection coefficients and the reverse transmission coefficient should be as low as possible, whereas the gain should be as high as possible.

### 2.2 Noise factor

Three main sources of electrical devices noise are thermal, Schottky and flicker noise [16]. As opposed to the well known signal-to-noise ratio,  $S/N$  in the domain of RF IC design a parameter mostly used to present the information on internal noise are the noise factor,  $F$ , and the noise figure,  $NF$ . Noise factor represents the ratio of signal-to-noise ratio at the input and signal-to-noise ratio at the output:

$$F = \frac{(S/N)_{input}}{(S/N)_{output}}. \quad (3)$$

Noise figure is a dB representation of noise factor, obtained as follows:

$$NF = 10 \log F. \quad (4)$$

### 2.3 Linearity

Two parameters are used to characterize an amplifier in the aspect of linearity: 1-dB compression point,  $P_{1dB}$  and input-referred third-order intermodulation (IM) intercept point,  $IIP3$ . The former represents the upper limit of the input signal power for which the LNA provides the expected output. This limit is defined as the input signal power which causes the real output to be less than expected output by exactly 1 dB [11, 16].

The latter figure of merit,  $IIP3$ , is required to take into account the influence of IM products; namely, the existence of two signals of frequencies close to each other at the input, gives rise to IM products. Second-order IM products can be easily filtered out, but third-order products can rise at frequencies within the information signal bandwidth and, thus, cause linearity issues [11].

The number associated with  $IIP3$  is obtained by bringing two signals of close frequencies and of equal amplitudes to the circuit input. Then, both output signal power and output third-order IM product power are plotted versus input power signal. Extrapolation of those two curves yields an intercept point. The  $P_m$  at which the extrapolated intercept point appears is actually the  $IIP3$ .

These two figures of merit are related as follows [11]:

$$IIP3 - P_{1dB} = 9.6 \text{ dB}, \quad (5)$$

under the condition that all nonlinearities of the order higher than 3 can be neglected.

### 2.4 Stability

Another working mode which amplification circuit may not enter during normal operation is oscillation. A figure of merit that needs attention in this context is circuit stability. It is possible to maintain the circuit stability at arbitrary input signal magnitudes (unconditional stability). There are multiple parameters defined as stability factors, but those used within this paper are the  $\mu$  and  $\mu'$  factor. The former represents the distance from the Smith chart center point to the area where instability occurs caused by the load. It is calculated as follows [15]:

$$\mu = \frac{1 - |S_{11}|^2}{|S_{22} - \Delta S_{11}^*| + |S_{12} S_{21}|}, \quad (6)$$

where:

$$\Delta = S_{11} S_{22} - S_{12} S_{21}. \quad (7)$$

The latter is the distance from the center point to the area where instability occurs caused by the source. It is obtained in similar fashion:

$$\mu' = \frac{1 - |S_{22}|^2}{|S_{11} - \Delta S_{22}^*| + |S_{12} S_{21}|}. \quad (8)$$

A two-port network is unconditionally stable if  $\mu > 1$  and  $\mu' > 1$ .

## 3 Related Work

Achieving broadband gain is a fundamental requirement in an UWB receiver, which means that this is also necessary for any LNA – as it is the first stage of a receiver.

er in any of the cases mentioned in section 1. Depending on the system architecture, the approximate band covered by the LNA in most cases is either of the three frequency ranges: (i) from 3.1 to 5 GHz (low band), (ii) 6 to 10.6 GHz (high band) or (iii) 3.1 to 10.6 GHz (full band).

LNAs present in literature can also be classified according to the circuit topology applied to meet the requirements for each of the figures presented in section 2. Those can be broadly categorized into four types, as follows [18]:

- distributed amplifier,
- input reactive networks,
- resistive-feedback, and
- common-gate circuits.

These possible implementations are shown in Figure 2 at the highest level of abstraction.

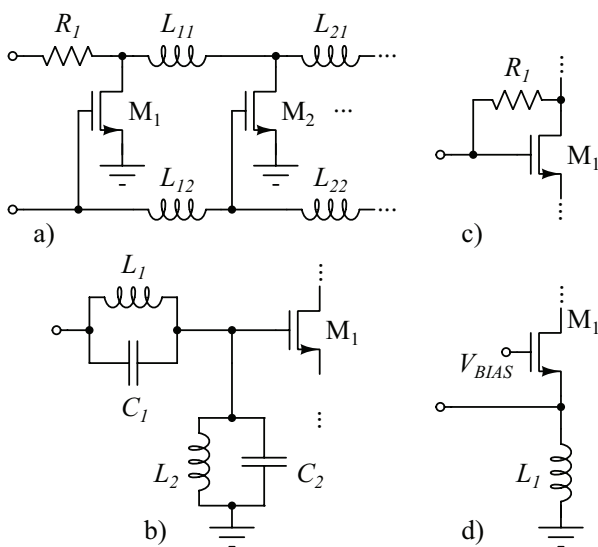


**Figure 2:** The standard wide bandwidth input matching techniques: a) distributed amplifiers, b) input reactive network, c) resistive-feedback and d) common-gate circuit

Distributed amplifiers, 0a, provide wide bandwidth characteristics, but tend to consume large DC currents due to the distribution of multiple amplifying stages which makes them unsuitable for low-power applications. Besides, such implementations contain a number of on-chip inductivities, so the whole circuit demands a larger area. In 0b, a topology which adopts a bandpass LC filter at the input of the LNA for wideband input matching is shown. The bandpass-filter-based topology incorporates the input impedance of the amplifier as a part of the filter, and shows good performances while dissipating small amounts of DC power. However, the inclusion of LC filter at the input demands a number of reactive elements, which introduce additional noise

and increase the chip area needed. In 0c and 0d, resistive-feedback and common-gate topologies principles are shown, respectively. The resistive feedback based amplifiers provide good wideband matching and flat gain, but the noise figure deteriorates due to additional resistive element and power dissipation increases. The common-gate input characteristic depends on the transistors geometry and the inductance in the source circuit. These parameters can be set in such a way that the circuit provides wideband input matching [18].

In [18] an LNA is designed applying the RC feedback topology, employing a gain enhancement technique and containing only one inductor. A frequency selective broadband LNA is presented in [19], where a topology of either a global or local feedback or the combination of both is investigated. In [20] a two-stage common-source (CS) LNA that utilizes forward-body-bias (FBB) technique in n-type MOS devices is presented. The authors in [21] also employed the FBB technique along with the current-reuse scheme and active shunt-feedback towards their goal of ultra-low power consumption. In [22] an UWB LNA with operating frequency range from 50 MHz to 10 GHz with resistive feedback and  $\pi$ -matching network is presented.

From the papers mentioned in the previous paragraph and keeping in mind the dates of those publications (2014-2017), we can conclude that UWB is an active research area interesting from the design of RF IC point of view. Designers [18-22] are utilizing different technologies, topologies, techniques and approaches while trying to optimize performance over a large number of, often opposing each other, requirements. Those requirements differ from case to case, thus no general way of comparing LNA performance is possible. Therefore, no figure of merit can be used on its own, rather the whole design must be considered within the context of specific application.

## 4 Low Noise Amplifier Design

In the following subsections, we present a UWB LNA, designed using the Cadence Design Systems® tool-chain and fabricated using the standard 130 nm CMOS process. First the topology choice is presented, where each stage is thoroughly discussed. Then physical design details are presented, describing the circuit layout. Finally, simulation results after parasitic extraction (postlayout simulation) are presented.

### 4.1 Topology Considerations

UWB circuits and systems must deal with numerous trade-offs [11]. For example, to design a highly linear

amplifier, large values of transistor overdrive voltages ( $V_{OD}=V_{GS}V_p$ ) are required; which causes the increase in drain currents and, consequently, in power consumption. This means that high linearity and low power consumption are opposed design goals. Analogous to this conclusion, when other LNA design goals mentioned in sections 1 and 2 are considered, similar facts can be derived; i.e. it is a matter of trade-off between figures of merit how well the circuit will perform overall.

In that context, the most interesting topologies out of those discussed in section 3 are resistive-feedback (Figure 2c) and common-gate (Figure 2d). Both of them satisfy input matching across a wide frequency range, and offer a compromise between the numerous demands. For high gain conditions, the noise and gain performance of a resistive-feedback and of a common-gate is virtually the same. A key difference arises at high frequencies, where the load capacitance  $C_L$  has a very significant impact on the input impedance in the case of the resistive-feedback amplifier, while this is not so in the common-gate case [5]. Derivations thoroughly presented and discussed in literature [17], show that the source impedance of a common-source topology yielding minimum noise factor must be inductive in nature. As the input impedance of a MOSFET in such configuration is capacitive, providing a good match to a 50  $\Omega$  source is a difficult task. Nevertheless, for an LNA, presenting a resistive impedance of this value to the external circuits and sub-circuits is a critical requirement – therefore, the LNA topology and the elements it comprises of, must be selected accordingly. The simplest approach would be to connect a 50  $\Omega$  resistor between the gate and source terminals of a common-source connected MOSFET. However, the resistor adds thermal noise of its own and, as it creates a voltage divider, it attenuates the signal by a factor of two. It turns out, as it is further explained in subsection 4.2, that a common-gate topology realizes resistive input impedance, as shown in equation (9).

However, common-gate amplifier topology cannot typically be used directly in UWB front-ends, as a consequence of its inadequate noise performance over the frequency range of interest, as well as potential failure to meet gain-bandwidth product requirement. This single-transistor topology thus needs to be enhanced to achieve the desired noise, gain and bandwidth specifications [5]. For this reason, the second stage consisting of a common-source amplifier employing the shunt-peaking technique [16] is cascaded to the first stage.

The proposed solution schematic is shown in Figure 3. This LNA circuit can be divided in three sub-circuits: common-gate (first stage), bandpass filter and com-

mon-source (second stage). All transistors operate in the strong inversion region.

Two circuit nodes directly controlling transistor biasing are accessible from outside through the pads, thus making the LNA operating region adaptable even after fabrication. These connections are omitted from Figure 3 for simplicity, but allow fine tuning of  $M_1$  and  $M_2$  operating points through  $V_{B1}$  and  $V_{B2}$  values setup. This is done with the idea to enable compensation of the potential process variations.

Finally, substrate of each transistor is grounded with a high resistivity resistor (body floating). In this way substrate current noise referred to drain node is reduced, resulting in overall NF reduction of about 0.5 dB [17].

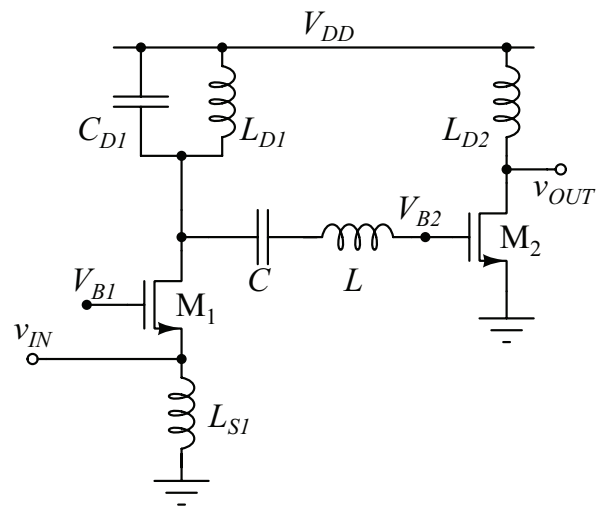


**Figure 3:** Proposed circuit (biasing, substrate contacts, pads and body floating resistors omitted)

#### 4.2 Common-gate Stage

The first stage consists of a transistor  $M_1$  in a common-gate configuration with a coil  $L_{s1}$  in the source and an RLC resonant circuit in the drain. In its first approximation, its input impedance is:

$$Z_{in} \approx \frac{1}{g_m}, \tag{9}$$

where  $g_m$  is transistor's transconductance. This relation is quite straightforward and, thus,  $M_1$ , along with inductor  $L_{s1}$ , is used to set input impedance towards the goal of 50  $\Omega$ , i.e. input return loss ( $S_{11}$ ) below -10 dB. The source input matching is needed in order to avoid signal reflections at the input of the LNA or the alterations of the characteristics of the RF filter preceding the LNA, such as pass-band ripple and stop-band attenuation [7].



Voltage gain of the common-gate stage is given as [1]:

$$\frac{V_{out}}{V_{in}} = \frac{g_m r_{out} + 1}{2 \left( 1 + \frac{r_{out}}{R_{D1}} \right)}, \quad (10)$$

where  $r_{out}$  represents the  $M_1$  output resistance and  $R_{D1}$  is the resistance in the drain of  $M_1$ . The resistor  $R_{D1}$  is not shown in Figure 3, as it is actually composed of resistive parasitics contained in  $L_{D1}$ ,  $C_{D1}$  and interconnects.

This common-gate configuration also acts as a tuned amplifier; namely, the resonant circuit consisting of  $L_{D1}$ ,  $C_{D1}$  and  $R_{D1}$  enables this subcircuit to amplify the signal within the band around the resonant frequency. The resonant circuit is not decoupled from the rest of the amplifier, so in all considerations other elements also must be included. Concretely, it is influenced by the  $M_1$  parasitic output impedance and the bandpass filter input impedance. Including the additional parasitics, the resonant circuit is tuned to 5.8 GHz.

For a MOSFET transistor operating in saturation, the most dominant noise source is channel thermal noise. Power spectral density of a saturated MOSFET is calculated in the following way [16]:

$$\overline{i_{nd}^2} = 4 \cdot kT \cdot \gamma \cdot g_{d0} \cdot \Delta f \quad (11)$$

is assumed the dominant source of noise, where  $g_{d0}$  is the drain-source conductance at zero  $V_{DS}$  and  $\gamma$  is the correction factor named excess-noise factor. For a sub-micron MOSFET, we assume:  $g_{d0}/g_m > 1$  and  $\gamma = 2/3$  for a long-channel saturated transistor in strong inversion. Value of  $\gamma$  can be larger,  $\gamma > 1$ , in the case of a short-channel transistor, as it strongly depends on the channel length modulation effect [16]. The noise factor of a common-gate device at low frequencies, when the input impedance is matched to the source, is given by:

$$F = 1 + \gamma + 4 \frac{R_S}{R_L}. \quad (12)$$

which, indirectly, yields  $NF$ , also. Thus, as the gain is increased by increasing the value of  $R_L$ , the noise factor similarly asymptotically assumes a value of  $1 + \gamma$ . This result also assumes that the common-gate amplifier uses an RF choke, which in this case is  $L_{S1}$ . The inductor is necessary, as the usage of a resistor or a current source instead would increase the noise factor [15, 16]. Therefore, the main purpose of  $L_{S1}$  is the reduction of noise factor. To achieve this, its value must be carefully selected. This is done first by preliminary calculations, based on the fact that this inductor, to enable noise figure

reduction, must resonate with the total capacitance in its proximity, which includes: capacitance of the input signal pad ( $C_{pad}$ ), the parasitic of the transistor  $M_1$  ( $C_{SB1}$  and  $C_{GS1}$ ) and its own parasitic capacitance ( $C_{LS1}$ ). A first order approximation yields:

$$L_{S1} = \frac{2 \cdot \pi \cdot f_{res}}{C_{pad} + C_{SB1} + C_{GS1} + C_{LS1}} \quad (13)$$

where  $f_{res}$  is the frequency at which the resonance occurs, in this case being equal to the frequency the  $RLC$  circuit in the drain of  $M_1$  is tuned to (5.8 GHz). As these capacitive parasitics cannot be known a priori, the calculation according to equation (13) is only the first step; namely, the final value of  $L_{S1}$  is yielded through simulations in several iterations.

#### 4.3 Common-source Stage

The cascaded second stage is a common-source circuit consisting of the transistor  $M_2$  loaded by the coil  $L_{D2}$ . Just as in the previous stage, a resonant circuit was used to set the working frequency range, in this stage it is done by a single coil in the drain circuit. This approach is known as shunt-peaking technique [16]. At higher frequencies, as the impedance of the inductance increases, that of the load capacitance decreases. By properly controlling the relative value of the load inductance in relation to the parasitic capacitance, a flat gain can be achieved over a wider bandwidth. In fact, a bandwidth extension of as much as 70% can be achieved by use of a single inductor, in comparison to a simple shunt RC load. In the case of wideband amplifiers, the inductor does not require a high-quality factor, since the bandwidth is supposed to be the widest possible.

Besides its influence on the gain characteristic,  $L_{D2}$  directly determines the output return loss,  $S_{22}$ .

#### 4.4 Bandpass filter

Impedance matching between the amplifying stages is achieved employing the bandpass filter composed of an inductor  $L$  and a capacitor  $C$ . The capacitance  $C$  is also used to decouple the first and the second stage, thus enabling the  $M_2$  transistor biasing. Keeping in mind this other purpose of the capacitive element and including the influence of the rest of the circuit, the bandpass filter is tuned to 9.5 GHz.

#### 4.5 Layout

In Figure 4 circuit's floorplan is presented. Elements occupying the largest area are four inductors, twelve

pads and a large decoupling capacitor formed as a vertically interdigitated structure encircling the LNA core, formed in metal layers 1 and 8.

During schematic level design, pad influence on LNA performance (especially on  $\Gamma(\omega)$ ) was taken into account (even though omitted from Figure 3). Groups of three pads on the left and right represent input and output ports in the constellation ground-signal-ground (GSG), where the middle pad is input and output, respectively. Top and bottom pad groups are in power-ground-logic form, where “logic” contacts are used as the inputs for transistor biasing control. Both power supply and ground connections are present on two sides (top and bottom) of the design in order to secure equal voltage levels of  $V_{DD}$  over the whole die.

The transistors  $M_1$  and  $M_2$  are each implemented as multiple transistors in parallel. Thus, more fingers are available to reduce effective gate resistance [17, 23].

Contrary to analog circuits where components and interconnects can be placed in the vicinity of each other, in the case of RF circuits that is not always possible. To ensure inductor operation without crosstalk, they must be safely distanced from other circuit components. The same consideration is applied to interconnects, as their behavior significantly changes at high frequencies (HF). For this reason plenty of empty space can be seen in Figure 4. However, that may not be fabricated as such, because metal density limitations are present in every CMOS technology node [24]. Therefore, these areas are filled with metal islands in order to satisfy the demand for metal density while degrading circuit performance as minimum as possible.

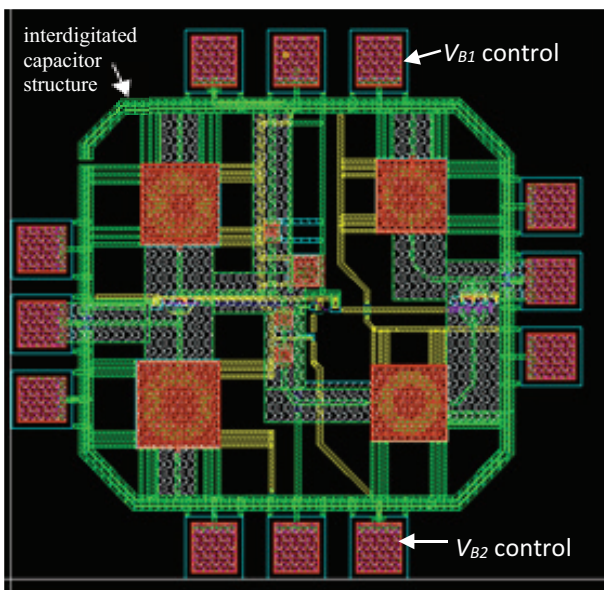


Figure 4: LNA layout screenshot as designed

The circuit occupies silicon area of 0.89 mm<sup>2</sup>, whereas the LNA core (LNA design without the pads and the interdigitated capacitor) occupies the area of 0.66 mm<sup>2</sup>.

#### 4.6 Post-layout Simulation Results

After the parasitic extraction and prior to fabrication, final scattering parameters and noise figure results are shown in Figure 5. For this nominal case,  $M_1$  biasing is set at  $V_{B1}=570$  mV and  $M_2$  biasing is done through a current mirror – the reference branch of which is biased at  $V_{B2}=1.2$  V. The maximum gain,  $S_{21}$ , is 15.48 dB, whereas the 3 dB frequencies are at 6.31 and 9.07 GHz. Input matching, measured by  $S_{11}$ , is better than -10 dB over the whole range. Output reflection coefficient is somewhat higher than -10 dB. However, such values for  $S_{22}$  are acceptable [17].

Minimum value of  $NF$  within the frequency range of interest is 3.8 dB at 7.10 GHz.

Power consumption is 18.41 mW from the supply voltage of 1.2 V.

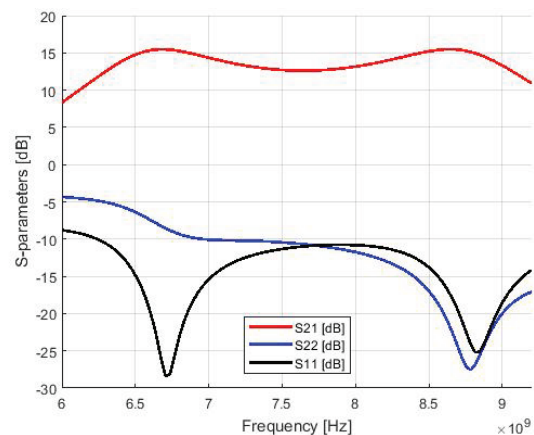


Figure 5: Post-layout scattering parameter simulation results

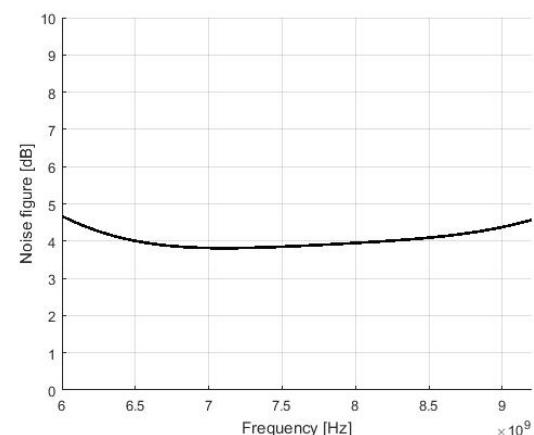


Figure 6: Post-layout noise figure simulation results

Linearity figures of merit of the designed LNA are summarized in 0, as defined in section 0.  $IIP3$  is simulated in two cases, hence the designations @ 50 MHz and @ 200 MHz. In the former case, the second signal is a 50 MHz offset relative to the main signal, whereas in the latter case the second signal is a 200 MHz offset relative to the main signal.

**Table 1:** Linearity figures of merit simulation results

f [GHz]	6.4	7	7.6	8.2	8.8
$IIP3$ @ 50 MHz [dBm]	0.38	1.33	3.18	2.38	0.95
$IIP3$ @ 200 MHz [dBm]	0.92	1.27	3.25	2.59	1.00
P1dB [dBm]	-8.68	-8.33	-6.35	-7.01	-8.60

### 5 Characterization

The on-chip characterization set-up is shown in Figure 7, consisting of VNA (N5240A from Keysight Technologies®), RF probe station, RF cables, two GSG probes and two DC PGL probes (all from Cascade Microtech®). First the influence of the equipment is canceled through VNA calibration process – short, open, load and thru (SOLT) procedure in this case – and then the characterization is performed.

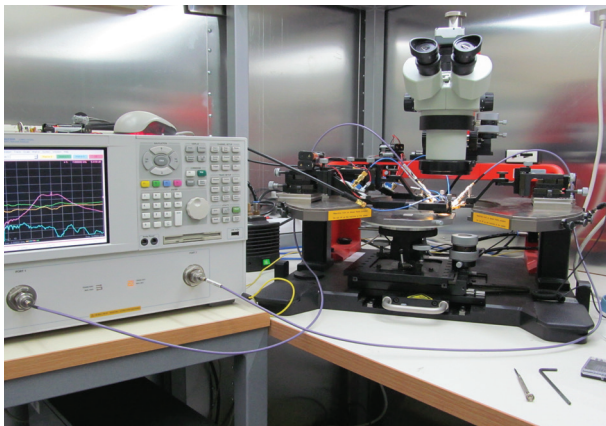


**Figure 7:** Measurement set-up

In Figure 8 fabricated circuit microphotograph is shown, while probe contact with pads is secured. Contrary to Figure 4, in this image metal filings are obvious.

In Figure 9-11 characterization results are shown at nominal biasing as given in subsection 4.6, witnessing scattering parameters behavior close to simulated values. A frequency shift of less than 10 % is present in all characteristics. Maximum gain is 12.33 dB, whereas the 3 dB band ranges from 5.74 GHz to 8.14 GHz, as shown in Figure 9. Input matching raises above -10 dB at mid-

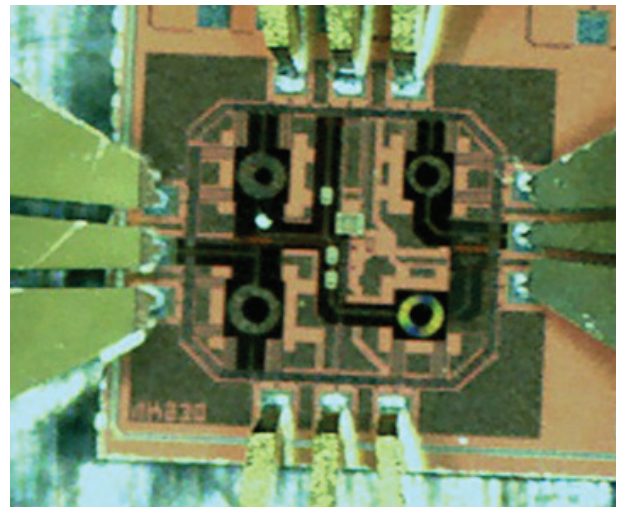


**Figure 8:** Die microphotograph

dle frequencies (around 7.54 GHz) but remains below for the rest of the 3 dB range, which is shown in Figure 10. Output reflection coefficient also deteriorates compared to post-layout simulation results shown in Figure 5, but within acceptable limits, as it is shown in Figure 11.

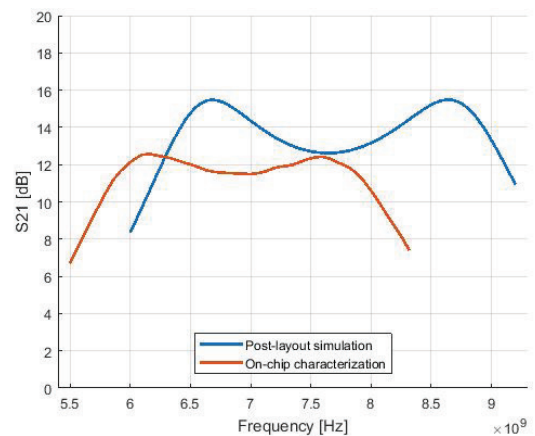


**Figure 9:**  $S_{21}$  characterization results (red) compared against the post-layout simulation results (blue)

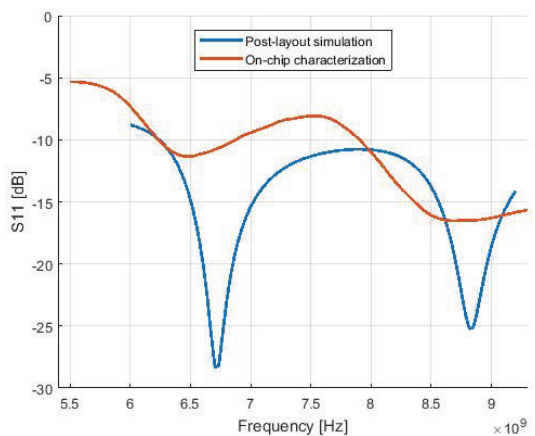


**Figure 10:**  $S_{11}$  characterization results (red) compared against the post-layout simulation results (blue)



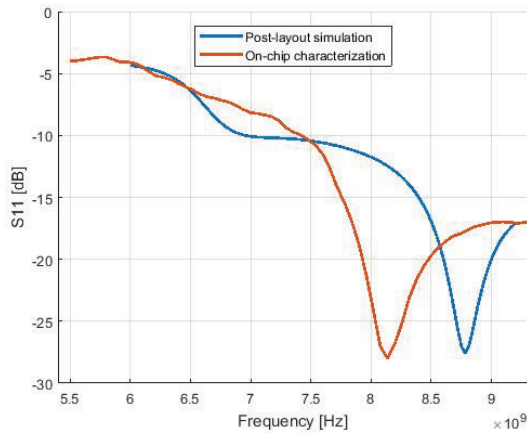


**Figure 11:**  $S_{22}$  characterization results (red) compared against the post-layout simulation results (blue)

In Figure 12 linearity characterization results are presented, showing a  $P_{1dB}$  point at -4.5 dBm of input power.

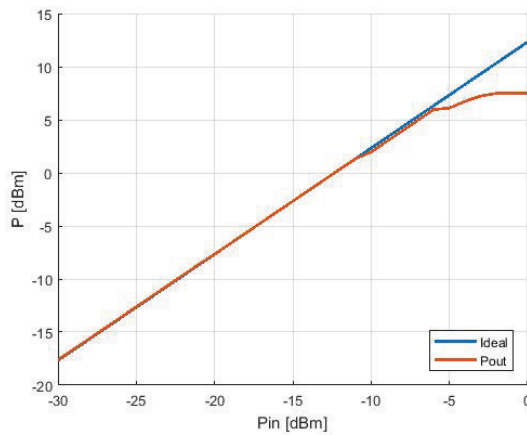


**Figure 12:** 1-dB compression point ( $P_{1dB}$ ) characterization results

## 6 Discussion

Characterization results deviate from the postlayout simulation as the frequency shift of 10 % is noticed in Figure 9 when compared to Figure 5. Therefore, 3 dB bandwidth of this circuit is from 5.74 to 8.14 GHz. Furthermore, LNA gain is deteriorated by 3 dB, as the maximum in postlayout is 15.48 dB, whereas the characterization yielded a maximum value of  $S_{21}$  as 12.33 dB. This is the reason why  $P_{1dB}$  is somewhat improved (-4.5 dBm) compared to expected results (Table 1); namely, since the gain is smaller, the amplifier will operate in the linear region at higher input signal power. Measured  $S_{11}$  is above -10 dB for a segment of the 3 dB bandwidth, in the vicinity of 7.54 GHz. Finally,  $S_{22}$  also departs from the predicted curve, but it does remain less than -5 dB over the frequency range of interest.

Frequency shift to lower frequencies and decrease in  $S_{21}$  are both signs of increased resistive parasitic components within the circuit interconnects [24]. Current density within a conductor of a circular cross-section is given as [25]:

$$J(u) = J(0) \left\{ \text{Re}(J_0(u)) + j\text{Im}(J_0(u)) \right\}, \quad (14)$$

Where  $u = \sqrt{-j} s$ ,  $s = k'r$ ,  $k' = \sqrt{\omega\mu\sigma}$ ,  $r$  distance to the conductor axis,  $J(0)$  current density along the conductor axis and  $J_0$  Bessel's function of order zero. At high frequencies, equation (14) can be approximated as follows:

$$J(x) = J_s e^{-\frac{x}{\delta}} \quad (15)$$

where  $J_s$  is current surface density,  $x$  distance to the conductor surface and  $\delta$  penetration depth, given by:

$$\delta = \frac{1}{\sqrt{\pi\mu\sigma f}}, \quad (16)$$

where  $\mu$  and  $\sigma$  represent permeability and conductivity, respectively.

Equation (14) is valid only for conductor of circular cross-section, whereas approximation (15) is also valid for conductors of rectangular cross-section. This effect is known as skin effect and it actually means that at low frequencies current flows through the whole cross-section uniformly; while, as the operating frequency rises, current flow is retreating towards the conductor surface. If the skin effect is dominant, current flows almost completely on the surface of the conductor. This further means that the cross-section of the part of the conductor used for current flow reduces as the frequency rises. Reduction of cross-section increases conductor surface resistance, which is directly proportional to  $\sqrt{f}$  [25], which theoretically justifies the decrease in gain magnitude and its shift to the lower frequencies, visible in Figures 9-11.

In Figure 13 and Figure 14 the influence of transistor  $M_1$  biasing to circuit operation is shown –  $S_{11}$  and  $S_{21}$ , respectively.

Two resonant pairs of frequencies can be seen in Figure 13. At values of 476, 526 and 576 mV for  $V_{B1}$ , one pair of resonant frequencies and at values of 810 mV, 1 and 1.2 V, another pair of resonant frequencies is noticed for  $S_{11}$ . The reason for such fundamental change in behavior is a consequence of different modes of operation of transistor  $M_1$ . For values of 476, 526 and

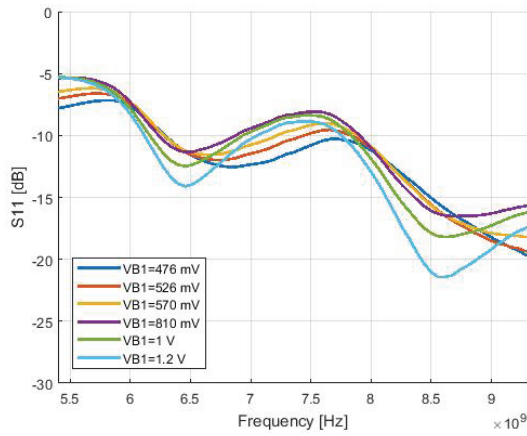


**Figure 13:** Transistor  $M_1$  biasing influence to  $S_{11}$

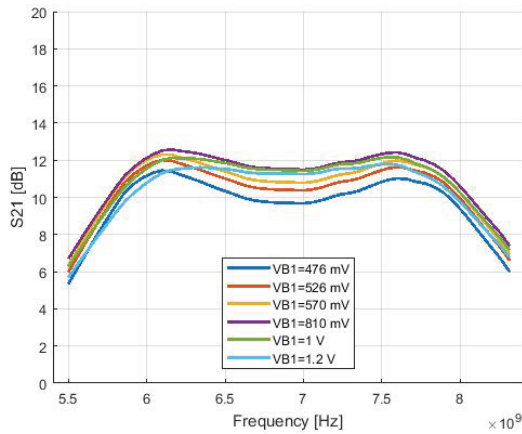


**Figure 14:** Transistor  $M_1$  biasing influence to  $S_{21}$

576 mV it operates in the weak inversion operation region and for values of 810 mV, 1 and 1.2 V it operates in the strong inversion. All parasitic capacitances (except for gate-substrate capacitance, denoted as  $C_{gb}$ ) are zero, whereas they (gate-source and substrate source, for example, denoted as  $C_{gs}$  and  $C_{bs}$ ) rise to significant values in the strong inversion saturation [26]. Thus, as gate-source voltage,  $V_{B1}$ , of  $M_1$  raises and it passes into strong inversion, the resonant frequencies shift to left. Even though  $S_{11}$  deteriorates above -10 dB at nominal value of  $V_{B1}$  (Figure 9), in Figure 13 it can be seen that  $V_{B1}$  may be used to eliminate this variation, e.g. by setting  $V_{B1}=476$  mV. In Figure 14 it is seen that variation of  $S_{21}$  may not be remedied as easily, but characteristics that are easily influenced to the extent are 3 dB range and  $S_{21}$  variation over that range. During characterization,  $V_{B2}$  was also varied. However, its influence to  $S_{22}$  was negligible, as that parameter is primarily determined by  $L_{D2}$ .

In Table 2, a summary of the circuit performance presented in this paper is given, along with several other

works cited. The purpose of this table in no way is a claim which of the circuits performance is better, since each of them was designed to optimize a different figure of merit; for example, in [21] the main goal was low power consumption, whereas in [22] the authors achieved very high linearity. Therefore, Table 2 is given here in order to point out that the characterization results obtained within this paper are of the same order like the results found in relevant and up-to-date literature.

**Table 2:** This work result summary and comparison to related work

	This work	[2]	[3]	[4]	[5]
technology [nm]	130	180	90	130	130
$S_{21MAX}$ [dB]	12.33	10.15	15	14	13.28
3 dB range [GHz]	5.74-8.14	1.1-5	3.5-9.25	0.6-4.2	0.05-10
$S_{11}$ [dB]	< -10	< -10	< -10	< -10	< -10
$S_{22}$ [dB]	< -5	< -10	< -10	< -10	< -10
$NF_{min}$ [dB]	3.8*	4.05*	2.4	4	3.29
$P_{1dB}$ [dBm]	-4.5	-9.5	-17.25	-19.6**	3.6**
$V_{DD}$ [V]	1.2	1.8	0.8	0.5	1.2
$P_{DD}$ [mW]	18.41*	28.54	9.6	0.25	31.2
area [mm <sup>2</sup> ]	0.66	0.35	0.56	0.39	0.77

\* simulated

\*\* estimated according to equation (5)

This work represents the continuation of research presented in [27]. In the next iteration of circuit redesign, electromagnetic (EM) properties [12, 24], such as skin effect, and PVT compensation techniques [28, 29] will be included.

## 7 Conclusion

Successful characterization of a fabricated UWB LNA using a standard 130 nm CMOS technology node is presented in this paper. The characterization results show that the techniques applied during the design phase of the circuit successfully fulfill its task: amplification over a wide frequency range with low noise factor. To prove this, a comparison with several state-of-the-art LNA designs found in literature is given in Table 2. The designed LNA provides 12.33 dB gain within the upper EU UWB band, its input reflection coefficient being less than -10 dB over the whole range. Minimum noise figure is shown to be 3.8 dB, while the circuit consumes 18.41 mW of power from a 1.2 V supply voltage. The amplifier remains linear for the input power levels up to -4.5 dBm and its area on chip is 0.66 mm<sup>2</sup>.



The in-depth discussions of the design procedure, the figures of merit and, especially, characterization approach provide detailed insight in the steps performed to achieve the obtained results. The characterization results do deviate less than 10 % of the post-layout simulation results, as a consequence of the skin effect; namely, due to the fact that the current is flowing on the surface of the conductor, resistance of the signal line increases proportionally to the square root of the operating frequency. However, techniques to tackle these effects are recognized and will be implemented in future work.

## 8 Acknowledgement

This research is done within the project: SENSEIVER-ITN – Low-cost and energy-efficient LTCC sensor/IR-UWB transceiver solutions for sustainable healthy environment, 2012-2015 a part of the FP7 Marie Curie Initial Training Network funded by the European Commission, contract number 289481 and partly within the project TR32016.

## 9 References

1. B. Razavi, RF Microelectronics, Prentice Hall, 2011.
2. A. Djugova, J. Radic, M. Videnovic-Misic, B. Goll and H. Zimmermann, "A Compact 3.1-5 GHz RC Feedback Low-Noise Amplifier Employing a Gain Enhancement Technique," *Informacije MIDEM, Journal of Microelectronics, Electronic Components and Materials*, vol. 44, no. 3, pp. 201-211, 2014.
3. S. Bagga, A. L. Mansano, W. A. Serdijn, J. R. Long, K. Van Hartingsveldt and K. Philips, "A Frequency-Selective Broadband Low-noise Amplifier with Double-Loop Transformer Feedback," *IEEE Transactions on Circuits and Systems I: Regular Papers*, vol. 61, no. 6, pp. 1883-1891, June 2014.
4. M. Parvizi, K. Allidina and M. N. El-Gamal, "Short Channel Output Conductance Enhancement Through Forward Body Biasing to Realize a 0.5 V 250  $\mu$ W 0.6–4.2 GHz Current-Reuse CMOS LNA," *IEEE Journal of Solid-State Circuits*, vol. 51, no. 3, pp. 574-586, 2016.
5. Y.-Y. Tey, H. Ramiah, N. M. Noh and U. R. Jagedheswaran, "A 50 MHz-10 GHz, 3.3 dB NF, +6 dBm IIP3 Resistive Feedback Common Source Amplifier for Cognitive Radio Application," *Microelectronics Journal*, vol. 61, no. 3, pp. 89-94, March 2017.
6. A. Pajkanovic and M. Videnovic-Misic, "An Ultra Wideband, 6-9 GHz, 130 nm CMOS Low Noise Amplifier," in *21st Telecommunications forum TELFOR 2013*, Belgrade, 2013.
7. B. Milinkovic, M. Milicevic, D. Simic, G. Stojanovic and R. Djuric, "Low-pass Filter for UWB System with the Circuit for Compensation of Process Induced On-chip Capacitor Variation," *Informacije MIDEM, Journal of Microelectronics, Electronic Components and Materials*, vol. 45, no. 4, pp. 266-276, 2015.
8. M. Milicevic, B. Milicevic, D. Simic, D. Grujic and L. Saranovac, "Temperature and Process Compensated RF Power Detector," *Informacije MIDEM, Journal of Microelectronics, Electronic Components and Materials*, vol. 46, no. 1, pp. 24-28, 2016.
9. J. Radic, A. Djugova, L. Nagy and M. Videnovic-Misic, "A Low-Complexity and Energy-Efficient IR-UWB Pulse Generator in 0.18  $\mu$ m Technology," *Informacije MIDEM, Journal of Microelectronics, Electronic Components and Materials*, vol. 43, no. 3, pp. 179-184, 2013.
10. B. Razavi, Design of Analog CMOS Integrated Circuits, McGrawHill Education, 2016.
11. P. Allen and D. Holberg, CMOS Analog Circuit Design, Oxford University Press, 2011.
12. Niknejad and Ali, Electromagnetics for High-Speed Analog and Digital Communication Circuits, Cambridge, 2007.
13. R. Gharpurey and P. Kinget, "Ultra Wideband: Circuits, Tranceivers and Systems," in *Ultra Wideband: Circuits, Tranceivers and Systems*, Springer, 2008, pp. 1-23.
14. A. Hastings, Art of Analog Layout, 2005.
15. T. Zwick, W. Wiesbeck, J. Timmermann and G. Adamiuk, Ultra-wideband RF System Engineering, Cambridge: Cambridge University Press, 2013.
16. O. Taheri, A. Maunder and P. Mousavi, "Correlation-Based UWB Radar for Thin Layer Resolution," *IEEE Antennas and Wireless Propagation Letters*, vol. 15, pp. 901-904, 2016.
17. A. T. Mobashsher and A. Abbosh, "Performance of Directional and Omnidirectional Antennas in Wideband Head Imaging," *IEEE Antennas and Wireless Propagation Letters*, vol. 15, pp. 1618-1621, 2016.
18. H. Bahrami, S. A. Mirbozorgi, A. T. Nguyen, B. Gosselin and L. A. Rusch, "System-Level Design of a Full-Duplex Wireless Transceiver for Brain-Machine Interfaces," *IEEE Transactions on Microwave Theory and Techniques*, vol. 64, no. 10, pp. 3332-3341, Oct 2016.
19. S. Voinigescu, High-Frequency Integrated Circuits, Cambridge University Press, 2013.
20. C. F. Liu and L. S. I., "A Broadband Noise-Canceling CMOS LNA for 3.1-10.6 GHz UWB Receivers," *IEEE Journal of Solid-State Circuits*, vol. 42, no. 2, pp. 1-16, 2007.
21. T. Lee, The RF CMOS Integrated Circuit Design, Prentice Hall, 1998.

22. D. M. Pozar, *Microwave Engineering*, 2nd Ed., John Wiley & Sons Ltd., 1998.
23. J. Li, S. Song, X. Chen, H. Nian and W. Shi, "Design and Implementation of a Novel Directional Coupler for UHF RFID Reader," *Electronics Journal*, vol. 20, no. 1, pp. 22-26, June 2016.
24. S. Pandey and J. Singh, "A 0.6 V, Low-power and High-gain Ultra-wideband Low-noise Amplifier with Forward-body-bias Technique for Low-voltage Operations," *IET Microwaves, Antennas and Propagation*, vol. 9, no. 8, pp. 728-734, 2015.
25. Y. T. Lo and J. F. Kiang, "Design of Wideband LNAs using parallel-to-series resonant matching network between common-gate and common-source stages," *IEEE Transactions on Microwave Theory and Techniques*, vol. 59, no. 9, pp. 2285-2294, 2011.
26. D. Grujic, "Design of Monolithic Microwave Integrated Circuits for 60 GHz Band - PhD thesis, in serbian," University of Belgrade, School of Electrical Engineering, Belgrade, 2013.
27. FCC, "First report and order: revision of part 15 of the Commission's rules regarding ultra-wideband transmission systems," *Et Docket*, 98-153, 2002.
28. B. Popovic, *Elektromagnetika*, Belgrade: Gradjevinska knjiga, in Serbian, 1985.
29. Y. Tsvividis, *Operation and Modeling of the MOS Transistor*, New York, Oxford: Oxford University Press, 2011.
30. M. C. Schneider and Galup-Montoro, *CMOS Analog Design using All-Region MOSFET Modeling*, Cambridge: Cambridge University Press, 2010.

Arrived: 14. 03. 2017

Accepted: 16. 06. 2017

# *Pb(Mg,Nb)O<sub>3</sub>-PbTiO<sub>3</sub> thick films on metalized low-temperature co-fired ceramic substrates*

H. Uršič<sup>1</sup>, A. Benčan<sup>1,2</sup>, E. Khomyakova<sup>1</sup>, S. Drnovšek<sup>1</sup>, I. F. Mercioniu<sup>3</sup>, K. Makarovič<sup>1,2,4</sup>, D. Belavič<sup>5</sup>, C. Schreiner<sup>6</sup>, R. Ciobanu<sup>6</sup>, P. Fanjul Bolado<sup>7</sup>, B. Malič<sup>1</sup>

<sup>1</sup>Jožef Stefan Institute, Ljubljana, Slovenia

<sup>2</sup>Centre of Excellence NAMASTE, Ljubljana, Slovenia

<sup>3</sup>Institutul National Cercetare-Dezvoltare pentru Fizica Materialelor, Bucharest, Romania

<sup>4</sup>Keko Equipment Ltd., Žužemberk, Slovenia

<sup>5</sup>HIPOT-RR d.o.o., Otočec, Slovenia

<sup>6</sup>Technical University of Iasi, Iasi, Romania

<sup>7</sup>DROPSSENS, Parque Tecnológico de Asturias - Llanera, Spain

**Abstract:** Compatibility of screen-printed piezoelectric 0.65Pb(Mg<sub>1/3</sub>Nb<sub>2/3</sub>)O<sub>3</sub>-0.35PbTiO<sub>3</sub> thick films with metalized low-temperature co-fired (LTCC) ceramic substrates is examined. Such substrates are interesting for micro-electro mechanical systems, for example for piezoelectric sensors and actuators, where functional layers are usually Pb-based piezoelectrics. In this study the special attention is given to the influence of the Au, Ag and Ag/Pd electrode materials coated over the LTCC on the functional properties of the films. The best phase purity, dielectric and piezoelectric properties were obtained in the films on gilded substrates. No secondary phases were observed at the film/Au interface by scanning electron microscope. The piezoelectric coefficient d<sub>33</sub> of the films on gilded substrates is equal to 120 pC/N.

**Keywords:** PMN-PT; piezoelectric; thick film; domain structure; low-temperature co-fired ceramic; LTCC

## *Debele plasti Pb(Mg,Nb)O<sub>3</sub>-PbTiO<sub>3</sub> na podlagah iz keramike z nizko temperature žganja*

**Izveček:** V članku poročamo o pripravi piezoelektričnih 0,65Pb(Mg<sub>1/3</sub>Nb<sub>2/3</sub>)O<sub>3</sub>-0,35PbTiO<sub>3</sub> debelih plasti na podlagah iz keramike z nizko temperature žganja. Omenjene podlage so uporabne v mikro elektro mehanskih sistemih, kot so piezoelektrični senzori in aktuatorji, zato je njihova kompatibilnost s funkcijskimi plastmi velikega pomena. Preučevali smo vpliv spodnje elektrode na lastnosti funkcijskih plasti. Pripravili smo vzorce s tremi različnimi elektrodami, z Ag, Ag/Pd in Au. Ugotovili smo, da plasti na različnih elektrodah izkazujejo različno fazno sestavo, dielektrične in piezoelektrične lastnosti. Plasti na Au elektrodah izkazujejo veliko boljše dielektrične in piezoelektrične lastnosti ter vsebujejo manj sekundarnih faz kot plasti na Ag in Ag/Pd elektrodah. Piezoelektrični koeficient d<sub>33</sub> plasti na podlagah iz keramike z nizko temperaturo žganja z zlatimi elektrodami je 120 pC/N.

**Ključne besede:** PMN-PT; piezoelektrik; debela plast; domenska struktura; keramika z nizko temperaturo žganja, LTCC

\*Corresponding Author's e-mail: hana.ursic@ijs.si

### *1 Introduction*

The thick-film technology is attractive for the production of simple functional structures and also quite complex systems. Screen-printing is one of the most widely used thick-film deposition techniques for producing up to a hundred micrometres thick piezoelectric films.

Commercially available piezoelectric thick films are mostly based on Pb(Zr,Ti)O<sub>3</sub> solid solution [1]. The most commonly used substrate materials for piezoelectric ceramic thick films are silicon and alumina. However, low-temperature co-fired ceramics (LTCC) are promising for the fabrication of three-dimensional ceramic

structures or ceramic micro-electro-mechanical systems (c-MEMS) and for this reason considered as desirable substrates for functional layers. The LTCC are based on glass-ceramic composites or crystallizing glass and densify at relatively low temperature (around 850 °C), which enables the use of low cost conductive materials and fast firing profiles [2, 3]. Therefore the LTCC and thick-film technologies enable fast and easy fabrication of electronic devices and systems, which could reduce the cost of devices and shorten the time of fabrication [2, 4]. The LTCC materials are especially interesting for actuator and sensor applications due to lower Young's modulus (90–110 GPa) than alumina (210–410 GPa), which enables high actuation sensitivity [1].

An alternative to  $\text{Pb}(\text{Zr,Ti})\text{O}_3$ -based piezoelectric material is  $(1-x)\text{Pb}(\text{Mg}_{1/3}\text{Nb}_{2/3})\text{O}_3-x\text{PbTiO}_3$  (PMN–100xPT) solid solution with the morphotropic phase boundary at  $x = 0.35$  [5, 6]. The PMN–35PT thick films prepared on silicon and alumina substrates possesses high dielectric permittivity (more than 3000 at 1 kHz and room temperature [7-9]) and high piezoelectric coefficients ( $d_{33}$  of 150 to 200 pC/N [9, 10]), and are therefore promising for sensor and actuator applications [11].

The aim of this work was to examine the compatibility of PMN–35PT piezoelectric thick films with metalized LTCC substrates. Until recently, only the  $\text{Pb}(\text{Zr,Ti})\text{O}_3$ -based piezoelectric thick films were processed on LTCC substrates [12-15]. But, the glass phase from LTCC may interact with  $\text{PbZr}_{0.53}\text{Ti}_{0.47}\text{O}_3$  (PZT) thick film and PbO from the thick film may diffuse into the LTCC during annealing [12, 13], which leads to changes in the thick film's phase composition and consequently functional properties. Hence the processing of piezoceramic films on LTCC materials is still challenging. In order to prevent the film-substrate interactions different solutions were reported, such as interposing of the barrier layer [12] or use of a very dense Au bottom electrode [15]. In this work the PMN–35PT thick films were prepared on metalized LTCC substrates with the interposed 15  $\mu\text{m}$  thick PZT barrier layer to minimize the film-substrate interactions.

## 2 Experimental methods

For the synthesis of the PMN–35PT powder, PbO (99.9 %, Aldrich), MgO (98 %, Aldrich),  $\text{TiO}_2$  (99.8 %, Alfa Aesar) and  $\text{Nb}_2\text{O}_5$  (99.9 %, Aldrich) were used. A mixture of these oxides in the molar ratio corresponding to the PMN–35PT stoichiometry with an excess of 2 mol% PbO was high-energy milled for 72 h at 300 rpm in a Retsch Model PM 400 planetary mill, and additionally in an attritor mill for 4 h at 800 rpm in isopropanol. The

powder was then heated at 700 °C for 1 h. The size of the particles after heating was determined by a light-scattering technique using a Microtrac S3500 Series Particle Size Analyzer instrument. The results were derived from the area particle size distribution. The most common parameter used is the median particle size  $d_{50}$ , where the area of all particles smaller than  $d_{50}$  accounts for 50 % of the area of all the particles. The powder morphology was analysed using the field-emission scanning electron microscopy (FE-SEM) JSM 7600F (Jeol, Tokyo, Japan). The powders were dispersed in acetone under ultrasound, and a few drops were spread on highly oriented pyrolytic graphite substrates. The PMN–35PT thick-film paste was prepared from a mixture of the PMN–35PT powder and an organic vehicle consisting of alpha-terpineol, [2-(2-butoxy-ethoxy)-ethyl]-acetate and ethyl cellulose in the ratio 60/25/15. For more details on PMN–35PT powder and thick-film paste processing and characterization see [7, 16].

The LTCC substrates were prepared by laminating three layers of the LTCC tape (DuPont 951) at 50 °C and 20 MPa. The laminated tapes were then heated at 450 °C for 1 h to burn-out the organic binder and densified at 875 °C for 15 min. In order to minimize the chemical interactions between the PMN–35PT thick film and the LTCC substrate, a PZT barrier layer was interposed between substrate and bottom electrode as suggested in [7, 17]. The PZT thick-film paste was printed on substrate and sintered 870 °C for 1 h. For more details regarding PZT powder and thick-film paste processing see [7]. The PZT/LTCC structure is further-on referred as the substrate. Thick-film silver (Ag ESL 9912MM), silver/palladium (80Ag/20Pd FERRO EL44-001) and gold (Au ESL 8884G) conductors were printed on the barrier layer/substrate structures and fired at 850 °C for 1 h. The thicknesses of the sintered electrodes were 50, 25 and 25  $\mu\text{m}$ , respectively.

The PMN–35PT paste was printed five times on the electrode substrate with intermediate drying at 150 °C after each printing step. The samples were pressed at 50 MPa, heated at 500 °C for 1 h to decompose the organic vehicle [16], sintered at 850 °C for 2 h in covered alumina crucibles in the presence of  $\text{PbZrO}_3$  packing powder with an excess of 2 mol% PbO and then cooled to room temperature with a rate of 2 °C/min.

The X-ray diffraction (XRD) patterns of the films were recorded using a PANalytical X'Pert PRO MPD (X'Pert PRO MPD, PANalytical, Almeo, The Netherlands) diffractometer with Cu–K $\alpha$ 1 radiation. The XRD patterns were recorded in the 2 $\theta$  region from 10° to 70° using a detector with a capture angle of 2.122°. The exposure time for each step was 100 s and the interval between the obtained data points was 0.034°.



For microstructural analysis the samples were mounted in epoxy, ground and polished using standard metallographic techniques. The microstructures of the samples were investigated with a FE-SEM JSM 7600F (Jeol, Tokyo, Japan) equipped with an Inca Energy Detector. The energy-dispersive X-ray spectroscopy (EDXS) analyses were performed at 15 keV. The average grain size (GS) was estimated from the SEM images obtained by backscattered electrons (BE) of the film's surface. For the stereological analysis more than 400 grains per sample were measured with the Image Tool Software. The GS is expressed as the Feret's diameter.

The topography and piezoresponse images were recorded with an atomic force microscope (AFM; Asylum Research, Molecular Force Probe 3D, Santa Barbara, CA, USA) equipped with a piezoresponse force mode (PFM). A tetrahedral Si tip coated with Ti/Ir (Asytec-01, Atomic-Force F&E GmbH, Mannheim, Germany) with the curvature diameter of  $30 \text{ nm} \pm 10 \text{ nm}$  was applied for scanning the sample surface. The out-of-plane amplitude PFM images were measured in the Single mode at ac amplitude signal of 20 V and frequency of  $\sim 300 \text{ kHz}$ . The local amplitude and phase hysteresis responses were measured in the Dual AC Resonance Tracking Switching Spectroscopy (DART-SS) mode with the waveform parameters: increasing step signal with maximum amplitude of 60 V and frequency 0.1 Hz; overlapping sinusoidal signal of amplitude 5 V and frequency 20 Hz, off-loop mode.

For dielectric and piezoelectric measurements, Cr/Au electrodes with a 1.5-mm diameter were deposited on the top surface of the films using RF-magnetron sputtering (5 Pascal). The dielectric permittivity ( $\epsilon'$ ) and dielectric losses ( $\tan \delta$ ) versus temperature were measured with a HP 4284 A Precision LCR Meter by ac amplitude of 1 V and frequencies of 1, 10, and 100 kHz during cooling from  $300 \text{ }^\circ\text{C}$  to  $25 \text{ }^\circ\text{C}$ . The films were poled at  $160 \text{ }^\circ\text{C}$  with a dc electric field from 2.5 to 7.5 kV/mm for 5 min and field-cooled to  $25 \text{ }^\circ\text{C}$ . After poling the samples were aged for 24 h. The piezoelectric constants  $d_{33}$  were measured by Berlincourt piezometer (Take Control PM10, Birmingham, UK) at alternating stress frequency of 100 Hz.

### 3 Results and discussion

#### 3.1 Characterisation of PMN-35PT powder

The particle size distribution of the PMN-35PT powder used for preparation of the thick-film paste is shown in Figure 1(a). The  $d_{50}$  was  $0.32 \text{ } \mu\text{m}$ . Around 10 % of the particles are larger than  $1 \text{ } \mu\text{m}$ , while the majority of them has a sub-micrometre size. Such distribution was confirmed by the FE-SEM analysis, where both fine sub-

micrometre and coarse particles were observed (Figure 1(b)). The XRD pattern of PMN-35PT mechanochemically synthesized powder after calcination at  $700 \text{ }^\circ\text{C}$  is shown in Figure 1(c). All reflections correspond to the perovskite phase.

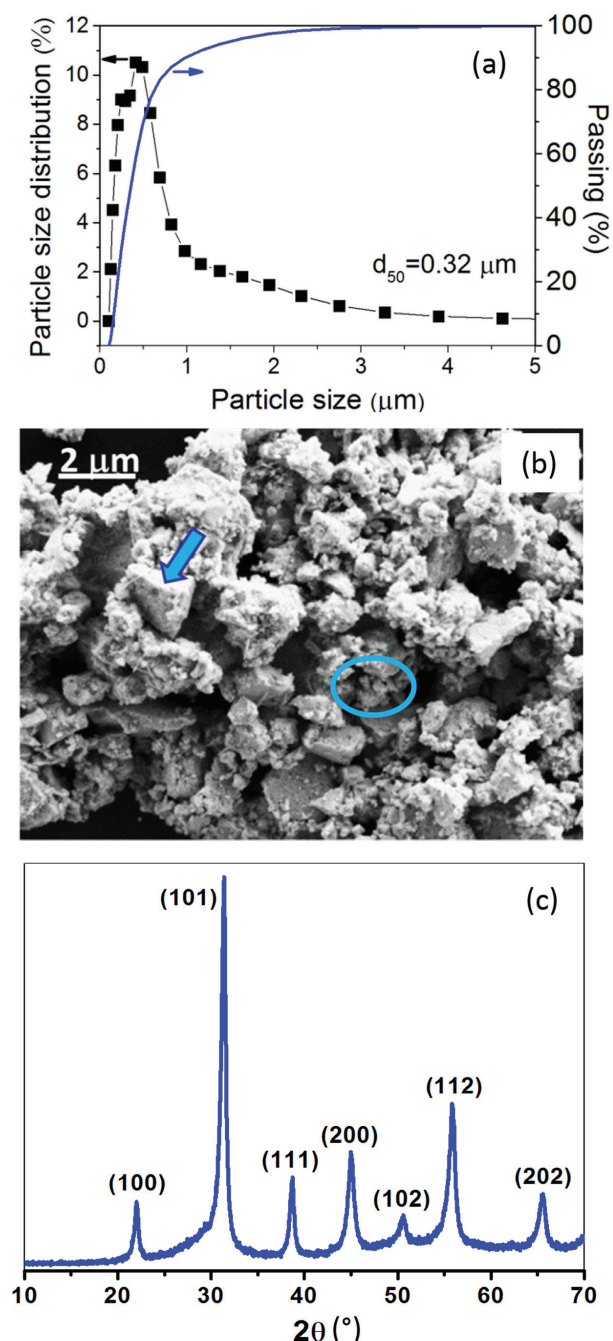


**Figure 1:** (a) The area particle size distribution, (b) FE-SEM micrograph and (c) XRD pattern of the PMN-35PT powder after heating at  $700 \text{ }^\circ\text{C}$  for 1 h. A coarse particle and smaller, submicron sized particles are marked by an arrow and a circle in panel (b), respectively. The indexed peaks of the pseudo-cubic perovskite phase (JCPDS 81-0861) are shown in brackets in panel (c).



### 3.2 The influence of the bottom electrode material on the phase composition and functional properties of PMN-35PT films

In order to study the influence of the bottom electrode layer on the properties of functional thick-film structures three different electrode materials were used; Ag, Ag/Pd and Au. Corresponding XRD patterns of ~60 μm thick PMN-35PT films on the metalized substrates are shown in Figure 2.

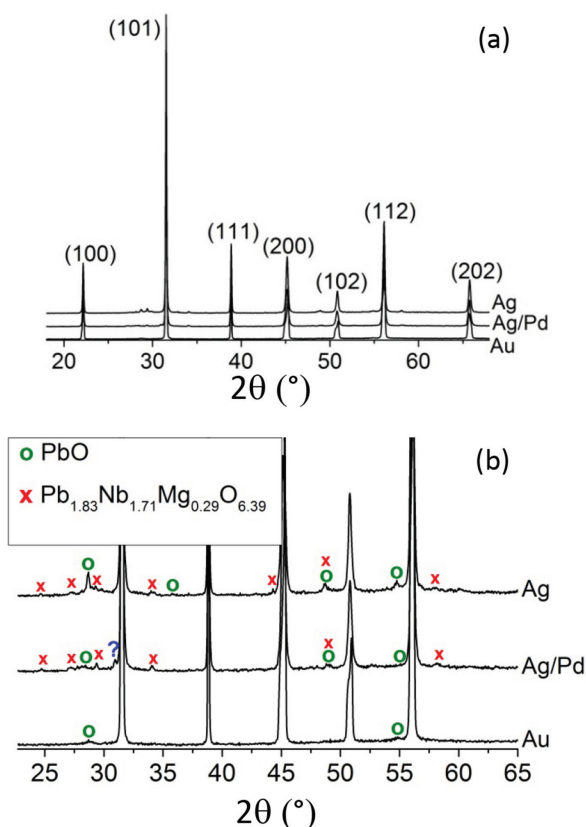


**Figure 2:** (a) XRD patterns of PMN-35PT thick films on Ag-, Ag/Pd- and Au-metalized substrates. The indexed peaks of the pseudo-cubic perovskite phase are shown in brackets (JCPDS 81-0861). (b) An enlarged  $2\theta$ -region from 23 to 65°. The peaks corresponding to PbO (JCPDS 78-1664) and pyrochlore  $\text{Pb}_{1.83}\text{Nb}_{1.71}\text{Mg}_{0.29}\text{O}_{6.39}$  (JCPDS 33-0769) are marked by  $\circ$  and  $\times$ , respectively. The reflection, which cannot be clearly identified by crystallographic cards, is marked by a question mark in Fig. (b).

In addition to the perovskite reflections, also low-intensity PbO and pyrochlore reflections are observed in XRD patterns of the films on Ag- and Ag/Pd-metalized substrates. In the latter, also one reflection exists, which cannot be clearly identified by crystallographic cards in JCPDS base (marked by a question mark in Figure 2(b)). Note that the penetration depth of X-rays in PMN-35PT thick films is around 10 μm [10] and there-

fore the results show only the composition of the upper part of the thick films. On the other hand in the XRD pattern of PMN-35PT thick film on Au-metalized substrate the perovskite reflections and only a trace of two reflections corresponding to PbO phase can be observed. These low-intensity diffraction peaks are most probably related to the initial excess of PbO in the starting powder mixture (see Experimental methods). The secondary phases determined from the XRD patterns together with the dielectric properties of PMN-35PT thick films on metalized substrates are collected in Table 1.

**Table 1:** The secondary phases (SP) determined from the XRD patterns, the room-temperature dielectric and piezoelectric properties of PMN-35PT thick films on metalized substrates.

electrode	SP	$\epsilon'$ at 10 kHz	$\tan \delta$ at 10 kHz	$d_{33}$ at 5.5 kV/mm
Ag	PbO, Py	250	/*	/
Ag/Pd	PbO, Py, UP	300	0.04	/
Au	traces of PbO	1050	0.04	120

/not possible to pole

/\*not possible to measure at 10 kHz,  $\tan \delta$  is 0.06 at 100 kHz

UP-unidentified phase, Py-pyrochlore

The dielectric permittivity of the films on Au-metalized substrates is 1050 at 10 kHz, which is more than three times higher than in the films on Ag- and Ag/Pd-metalized substrates. The  $\tan \delta$  of films on Au- and Ag/Pd-metalized substrates are in the same range. For films on Ag-metalized substrates the  $\tan \delta$  at 10 kHz was not possible to measure. Low values of  $\epsilon'$  (i.e. 235) were previously reported also for PZT films on Ag/Pd-metalized LTCC (with no barrier layer between the LTCC and the electrode layer), which was attributed to intense interactions between the functional film and the substrate [14]. Furthermore, we were able to pole only the films on Au-metalized substrates (Table 1). The measured  $d_{33}$  coefficient of such films is 120 pC/N. Due to the superior phase purity, dielectric properties and ability of poling, we further analysed only the PMN-35PT films on Au-metalized (gilded) substrate. The microstructural, dielectric properties as a function of temperature and piezoelectric properties of these films are further discussed below.

### 3.3 The PMN-35PT thick films on gilded substrates

The photo of a PMN-35PT thick film on the gilded substrate is shown in Figure 3(a). The thick film surface is crack-free on cm scale. The BE-SEM images of the surface and polished cross-section of the film are shown

in Figure 3(b) and (c), respectively. Fig. 3(b) reveals a porous, but uniform microstructure. The estimated average grain size is  $\sim 0.8 \mu\text{m}$ . Some PbO, seen as a white inclusion in Figure 3(b), is also present in the film. The

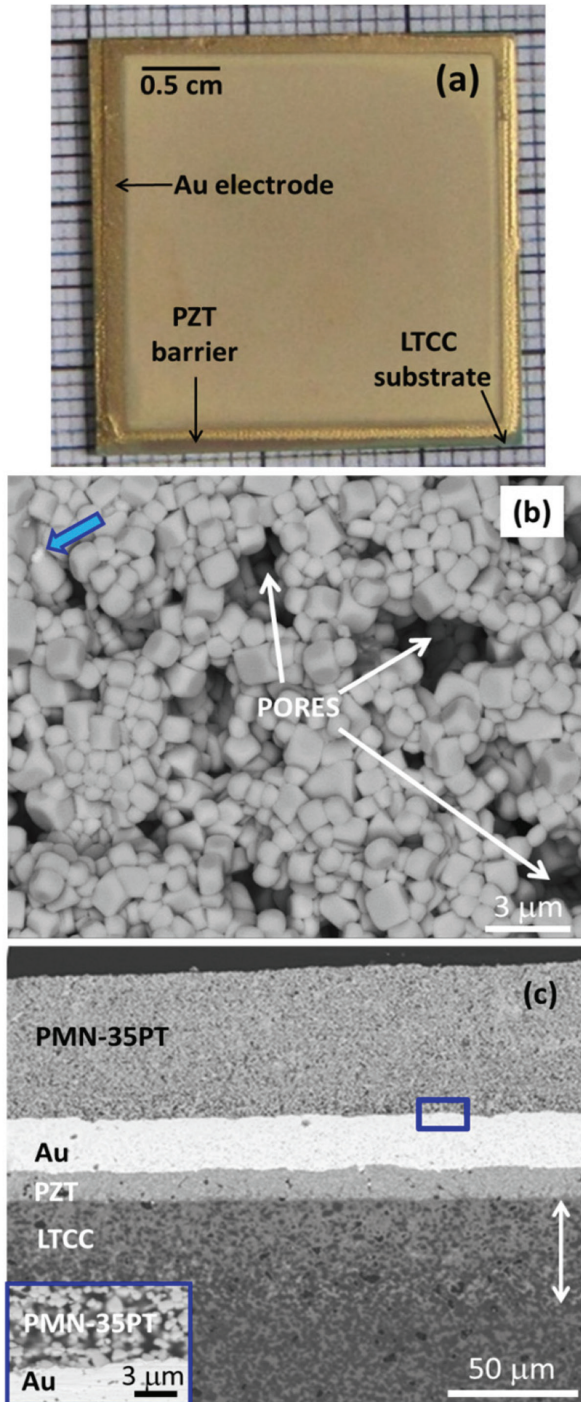


**Figure 3:** (a) The photo and BE-SEM images of (b) thick film surface and (c) polished cross-section of PMN-35PT thick film on gilded substrate. The thick arrow in panel (b) marks the PbO phase. In panel (c) the extension of a Pb rich layer in the LTCC is marked by an arrow and the inset shows an enlarged view of the PMN-35PT/Au interface.

results are in accordance with the XRD analysis, where in addition to the perovskite phase, a trace amount of PbO phase was also detected (see Fig. 2(b)). As seen in Figure 3(c) the thicknesses of the PZT barrier layer, Au and PMN-35PT film are  $\sim 15$ ,  $\sim 25$  and  $\sim 60 \mu\text{m}$ , respectively. The thickness of the PMN-35PT film is quite homogeneous across the substrate. No secondary phases are observed at the PMN-35PT/Au interface (inset in Figure 3(c)). Below the PZT layer into the LTCC substrate, a  $\sim 50 \mu\text{m}$  thick, brighter layer is formed (marked with an arrow). According to the EDXS analysis, this layer is PbO-rich and can be attributed to diffusion of PbO from PZT into the LTCC. Such layer was previously reported also in PZT/Au/LTCC structures, where the PbO diffused from the PZT functional layer into the substrate [13].

In Figure 4 the  $\epsilon'$  and  $\tan \delta$  as a function of temperature are shown for the PMN-35PT thick film on gilded substrate. At  $30^\circ\text{C}$  and 1 kHz the  $\epsilon'$  and  $\tan \delta$  are 1150 and 0.06, respectively. The temperature of  $\epsilon'_{\text{max}}$  ( $\sim 4800$ ) at 1 kHz is  $166^\circ\text{C} \pm 1^\circ\text{C}$ , which is in agreement with the previously published temperature for PMN-35PT bulk ceramics [18, 19]. The  $\epsilon'$  at room temperature is approximately three times lower than the one of the films on platinized alumina [7, 8] and approximately four times lower than PMN-35PT bulk ceramics [20], which could be attributed to the higher porosity and smaller average grain size of studied films on gilded LTCC substrates. On the other hand, the prepared films exhibit at least two times higher  $\epsilon'$  at room temperature than previously published PZT films on LTCC substrates [12-14].

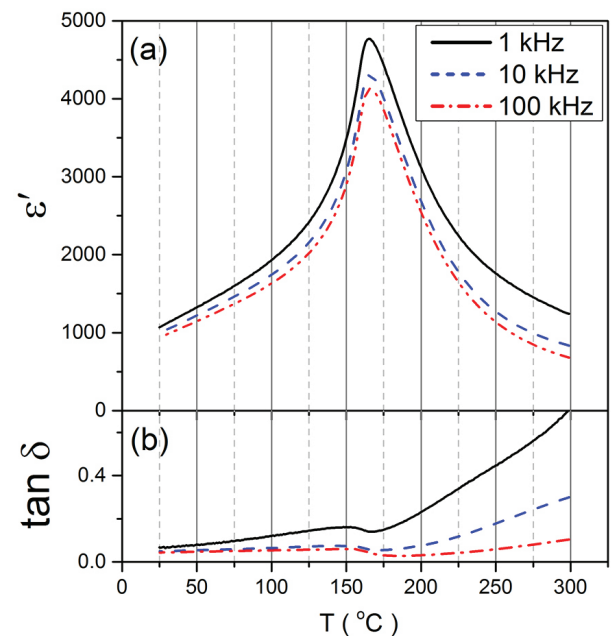


**Figure 4:** (a)  $\epsilon'$  and (b)  $\tan \delta$  of the PMN-35PT film on gilded substrate as a function of temperature at 1, 10 and 100 kHz.



Further the local piezoelectric response and ferroelectric domain configuration were investigated. The topography and out-of-plane PFM amplitude images

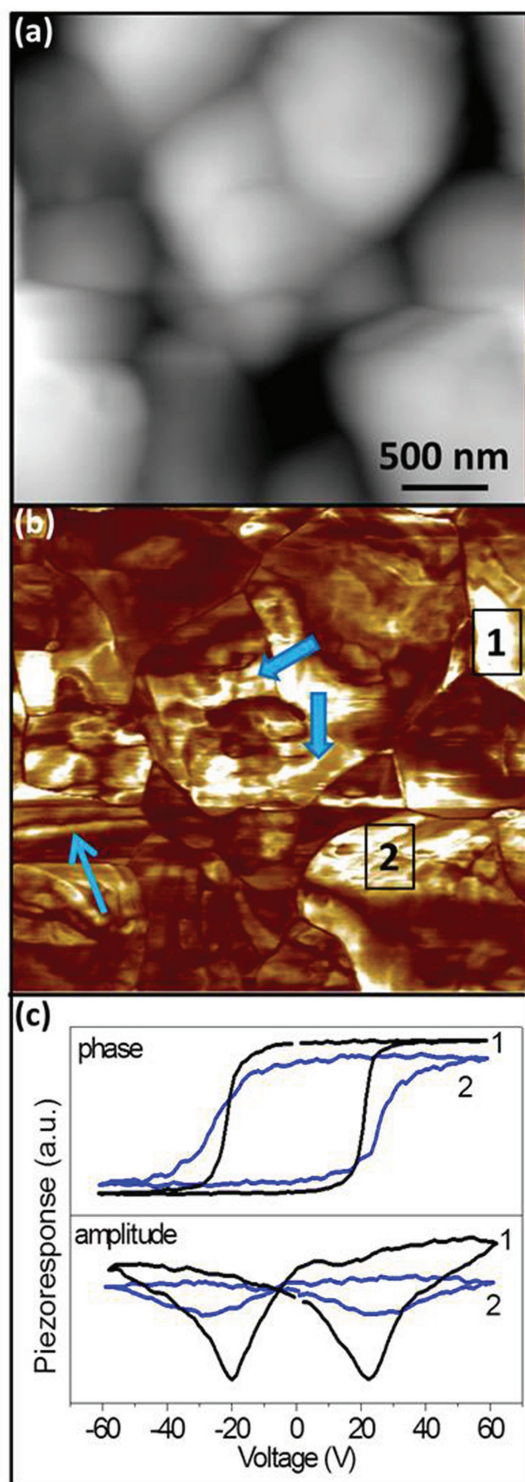


**Figure 5:** (a) Topography and (b) out-of-plane PFM amplitude image of the PMN–35PT thick film on gilded substrate. (c) PFM amplitude and phase hysteresis loops obtained from the areas marked by no. 1, 2 in the panel (b).

are shown in Figure 5 (a) and (b), respectively. In the topographical image, the grain boundaries can be clearly identified, while in the amplitude image the grain boundaries are visible as dark non-active boundaries. The enhanced local piezoelectric activity is evident as brighter areas within the grains. An example of such region is marked by no. 1 in Figure 5 (b). The most frequently observed domains in the film are irregularly shaped domains found also in  $\text{Pb}(\text{Sc}_{0.5}\text{Nb}_{0.5})\text{O}_3$  [21]. The size of the domains varies from a few hundred nanometres to a micrometre. Examples of such irregularly shaped domains are marked by thick arrows in Figure 5 (b). In addition rear lamellar-like domains can be found (marked by a thin arrow). Irregularly shaped and lamellar domains were previously observed also in PMN–35PT films on alumina substrates [22]. The local PFM amplitude and phase hysteresis loops are shown in Figure 5 (c) confirming a typical hysteretic response of the ferroelectric material and indicating the local domain switching.

The PMN–35PT thick films were poled with a dc electric field of 2.5–7.5 kV/mm as described in Experimental section. The  $d_{33}$  values are collected in Table 2. For the films poled at 2.5 kV/mm, the  $d_{33}$  was 65 pC/N, but it increased with the increasing poling field until 5.5 kV/mm. The highest  $d_{33}$  of 120 pC/N was measured for the samples poled at electric field amplitudes between 5.5 and 7.5 kV/mm. The  $d_{33}$  coefficient is only 20 % lower than the one reported for PMN–35PT films on platinized alumina, i.e., ~150 pC/N for similar film thickness [10]. We note that the reduction of  $d_{33}$  in PZT thick films deposited on LTCC or on alumina was much more pronounced than in our PMN–PT films; i.e., 75 pC/N versus 125 pC/N, which is about 40 %. Such strong deterioration of the piezoelectric response was attributed to the interaction between the PZT film and the LTCC substrate [13]. It is also important to mention that the piezoelectric coefficient of PMN–35PT bulk ceramics prepared from the mechanochemically synthesized powder, but sintered at 1200 °C is ~640 pC/N (at similar poling conditions; electric field of 4.5 kV/mm) [20].

**Table 2:** The piezoelectric coefficient  $d_{33}$  measured for the PMN–35PT films poled at different electric field amplitudes.

Epoling (kV/mm)	$d_{33}$ (pC/N)
2.5	65
3.5	85
4.5	100
5.5	120
6.5	120
7.5	120

The degradation of dielectric and piezoelectric properties of the PMN–35PT films on metalized LTCC substrates in comparison to the properties of the films on metalized alumina substrates could be related to the higher porosity of the films deposited on the former substrates. Further work is thus needed to improve the densification of the films on LTCC substrates.

#### 4 Summary and conclusions

The compatibility of piezoelectric PMN–35PT thick-films with metalized LTCC substrates (DuPont 951) was studied. Three different bottom electrodes were used; Ag, Ag/Pd and Au. The XRD analysis revealed the presence of a large amount of secondary phases in the films prepared on Ag- and Ag/Pd-metalized substrates, while in the film deposited on the Au-metalized substrate only a trace of PbO phase was detected. Furthermore, about three times higher room temperature dielectric permittivity (1050 at 10 kHz) was measured in the films on Au in comparison to the ones on Ag- and Ag/Pd-metalized substrates. The films on Ag- and Ag/Pd-metalized substrates could not be poled, but the ones on gilded substrates exhibit the piezoelectric coefficient  $d_{33}$  as high as 120 pC/N. Irregularly-shaped and lamellar-like domains with the size from a few hundred nanometres to micrometres were observed and the domain switching was confirmed by piezo-response force microscopy.

In conclusion, we succeeded to prepare ~60  $\mu\text{m}$  thick PMN–35PT films on gilded substrates, where no film-substrate interactions were observed by SEM. The films exhibit high piezoelectric properties, much higher than the ones previously published for lead-based thick films on LTCCs. However, further work is needed to improve the densification of these films aiming to further enhance their functional properties.

#### 5 Acknowledgements

This work was funded by M-ERA.NET project "Integrated sensors with microfluidic features using LTCC Technology" INT CERSEN (PR-06211) and the Slovenian Research Agency (research core funding No. P2-0105). Technical support by Mitja Jerlah, Jena Cilenšek, Brigita Kmet, Aneja Tuljak and Mateo Markov (Erasmus+ program) is gratefully acknowledged.

#### 6 References

- Zarnik M S, Ursic H, Kosec M. Recent progress in thick-film piezoelectric actuators prepared by screen-printing, in: Piezoelectric Actuators (*open access*), J. E. Segel, Ed., Nova Science Publishers Inc., 2011. [https://www.novapublishers.com/catalog/product\\_info.php?products\\_id=30015](https://www.novapublishers.com/catalog/product_info.php?products_id=30015)
- Imanaka Y. Multilayered low temperature co-fired ceramics (LTCC) technology. New York, USA, Springer, 2005. <http://link.springer.com/book/10.1007%2Fb101196>
- Makarovic K, Meden A, Hrovat M, Holc J, Bencan A, Dakskobler A, Kosec M. The effect of processing conditions on the properties of LTCC material, *J. Am. Ceram. Soc.*, 2012; 95: 760–767. <http://onlinelibrary.wiley.com/doi/10.1111/j.1551-2916.2011.05027.x/abstract>
- Belavic D, Hrovat M, Zarnik MS, Holc J, Kosec M. An investigation of thick PZT films for sensor applications: A case study with different electrode materials, *J. Electroceram.*, 2009; 23: 1–5. <http://link.springer.com/article/10.1007/s10832-008-9495-1>
- Singh A K, Pandey D. Evidence for MB and MC phases in the morphotropic phase boundary region of  $(1-x)[\text{Pb}(\text{Mg}_{1/3}\text{Nb}_{2/3})\text{O}_3]_x\text{PbTiO}_3$ : A rietveld study, *Phys. Rev. B*, 2003; 67, 064102 1–12. <https://journals.aps.org/prb/pdf/10.1103/PhysRevB.67.064102>
- Handbook of Advanced Dielectric, Piezoelectric and Ferroelectric Materials, Z.-G. Ye, Ed. Cambridge, England, Woodhead Publishing Ltd, 1<sup>st</sup> ed., 2008. <http://www.sciencedirect.com/science/book/9781845691868>
- Ursic H, Hrovat M, Holc J, Tellier J, Drnovsek S, Guiblin N, Dkhil B, Kosec M. Influence of the substrate on the phase composition and electrical properties of 0.65PMN–0.35PT thick films, *J. Eur. Ceram. Soc.*, 2010; 30: 2081–2092. <http://www.sciencedirect.com/science/article/pii/S0955221910001615>
- Gentil S, Damjanovic D, Setter N. Development of relaxor ferroelectric materials for screen-printing on alumina and silicon substrates. *J. Eur. Ceram. Soc.*, 2005; 25: 2125–2128. <http://www.sciencedirect.com/science/article/pii/S095522190500169X>
- Gentil S, Damjanovic D, Setter N.  $\text{Pb}(\text{Mg}_{1/3}\text{Nb}_{2/3})\text{O}_3$  and  $(1-x)\text{Pb}(\text{Mg}_{1/3}\text{Nb}_{2/3})\text{O}_3-x\text{PbTiO}_3$  relaxor ferroelectric thick films: processing and electrical characterization. *J. Electroceram.*, 2004; 12: 151–161. <http://link.springer.com/article/10.1023/B:JECR.0000037720.39443.e3>
- Ursic H, Zarnik MS, Tellier J, Hrovat M, Holc J, Kosec M. The influence of thermal stresses on the phase composition of  $0.65\text{Pb}(\text{Mg}_{1/3}\text{Nb}_{2/3})\text{O}_3-0.35\text{PbTiO}_3$  thick films, *J. Appl. Phys.*, 2011; 109: 014101 1–5. <http://aip.scitation.org/doi/full/10.1063/1.3526971>
- Ursic H, Zarnik MS, Kosec M.  $\text{Pb}(\text{Mg}_{1/3}\text{Nb}_{2/3})\text{O}_3-\text{PbTiO}_3$  (PMN–PT) material for actuator applications, *Smart Materials Research (open access)*,

- 2011; 2011: 452901 1–6. <https://www.hindawi.com/journals/smr/2011/452901/>
12. Hrovat M, Holc J, Drnovsek S, Belavic D, Cilensek J, Kosec M. PZT thick films on LTCC substrates with an interposed alumina barrier layer, *J. Eur. Ceram. Soc.*, 2006; 26: 897–900. <http://www.sciencedirect.com/science/article/pii/S0955221905000634>
  13. Ursic H, Hrovat M, Belavic D, Cilensek J, Drnovsek S, Holc J, Zarnik MS, Kosec M. Microstructural and electrical characterisation of PZT thick films on LTCC substrates, *J. Eur. Ceram. Soc.*, 2008; 28: 1839–1844. <http://www.sciencedirect.com/science/article/pii/S0955221908000253>
  14. Golonka L J, Buczek M, Hrovat M, Belavic D, Dziedzic A, Roguszczak H, Zawada T, Properties of PZT thick films made on LTCC, *Microelectronics Int.*, 2005; 22: 13–16. <http://www.emeraldinsight.com/doi/abs/10.1108/13565360510592171>
  15. Gebhardt S, Seffner L, Schlenkrich F, Schonecker A. PZT thick films for sensor and actuator applications, *J. Eur. Ceram. Soc.*, 2007; 27: 4177–4180. <http://www.sciencedirect.com/science/article/pii/S095522190700163X>
  16. Ursic H, Tchernychova E, Bencan A, Jouin J, Holc J, Drnovsek S, Hrovat M, Malic B. The influence of the platinum substrate roughness on the ferroelectric properties of  $0.65\text{Pb}(\text{Mg}_{1/3}\text{Nb}_{2/3})\text{O}_3-0.35\text{PbTiO}_3$  thick films, *Informacije MIDEM, Journal of Microelectronics, Electronic Components and Materials (open access)*, 2014; 44: 12–18, [http://www.midem-drustvo.si/Journal%20papers/MIDEM\\_44\(2014\)1p12.pdf](http://www.midem-drustvo.si/Journal%20papers/MIDEM_44(2014)1p12.pdf)
  17. Holc J, Hrovat M, Kosec M. Interactions between alumina and PLZT thick films. *Mater. Res. Bull.*, 1999; 34: 2271–8. <http://www.sciencedirect.com/science/article/pii/S0025540899002275>
  18. Alguero M, Ricote J, Jimenez R., Ramos P, Carreaud J, Dkhil B, Kiat J M, Holc J, Kosec M. Size effect in morphotropic phase boundary  $\text{Pb}(\text{Mg}_{1/3}\text{Nb}_{2/3})\text{O}_3-\text{PbTiO}_3$ , *Appl. Phys. Lett.*, 2007; 91: 112905 1–3. <http://aip.scitation.org/doi/abs/10.1063/1.2778471>
  19. Leite E R, Scotch A M, Khan A, Li T, Chan H M, Harmer M P, Liu S F and Park S E. Chemical heterogeneity in PMN–35PT ceramics and effects on dielectric and piezoelectric properties, *J. Am. Ceram. Soc.*, 2002; 85: 3018–3024. <http://onlinelibrary.wiley.com/doi/10.1111/j.1151-2916.2002.tb00572.x/abstract>
  20. Ursic H, Tellier J, Hrovat M, Holc J, Drnovsek S, Bobnar V, Alguero M, Kosec M. The Effect of Poling on the Properties of  $0.65\text{Pb}(\text{Mg}_{1/3}\text{Nb}_{2/3})\text{O}_3-0.35\text{PbTiO}_3$  Ceramics, *Jpn. J. Appl. Phys.*, 2011; 50: 035801-6.
  21. Ursic H, Drnovsek S, Malic B. Complex domain structure in polycrystalline  $\text{Pb}(\text{Sc}_{0.5}\text{Nb}_{0.5})\text{O}_3$ , *J. Phys. D: Appl. Phys.*, 2016; 49: 115304 1–4. <http://iopscience.iop.org/article/10.1088/0022-3727/49/11/115304>
  22. Ursic H, Ricote J, Amarin H, Holc J, Alguero M. Ferroelectric domain configurations in  $0.65\text{Pb}(\text{Mg}_{1/3}\text{Nb}_{2/3})\text{O}_3-0.35\text{PbTiO}_3$  thick films determined by piezoresponse force microscopy, *J. Phys. D: Appl. Phys.*, 2012; 45: 265402 1–11. <http://iopscience.iop.org/article/10.1088/0022-3727/45/26/265402>

Arrived: 17. 04. 2017

Accepted: 13. 07. 2017



# Considerations about the use of the Moon in X-band antenna G/T measurements

Darko Šekuljica<sup>1</sup>, Stefano Badessi<sup>1</sup>, Massimiliano Ferrante<sup>2</sup>, Matjaž Vidmar<sup>3</sup>

<sup>1</sup>European Space Agency

<sup>2</sup>Vitrociset S.p.A.

<sup>3</sup>University of Ljubljana, Faculty of Electrical Engineering, Ljubljana, Slovenia

**Abstract:** The most common G/T quality factor measurement methods applicable for operational X-band (8 GHz - 12 GHz) parabolic antennas with a reflector aperture diameter between 7 and 13m are reviewed. Analyses have shown that the most adequate astronomical source for the G/T measurement of the antennas with the size of interest is the Moon.

Since the Moon's angular diameter is wider than the antenna's Half Power Beam Width (HPBW), a thorough analysis of the extended source size correction factor is performed. As a result, an efficient correction factor approximation method which is more accurate in case of efficiency losses is identified, and a best-fit estimation method for the HPBW verification is introduced.

The proposed G/T quality factor measurement procedure is verified on an operational X-band 11 meter Cassegrain antenna, used for Low Earth Orbit (LEO) satellite data acquisition. The results obtained with the proposed method, have provided accurate G/T factor estimations that are consistent and in line with the expectations. As further confirmation, the validity of the measurement method results is also verified against a G/T measurement done with the Cassiopeia A radio star as an RF source.

**Keywords:** X-band, G/T measurements, Moon, Satellite communications, Extended source size correction factor

## Ugotovitve o uporabi Lune pri G/T meritvah antenskih sistemov frekvenčnega pasu X.

**Izveček:** Najbolj pogoste metode za merjenje kakovostnega faktorja G/T pri operativnih paraboličnih antenah frekvenčnega pasu X (8 GHz – 12 GHz) s premerom zaslone zrcala med 7 in 13 metrov so bile pregledane v tej študiji. Analiza je pokazala, da je Luna najbolj ustrezen astronomski vir za G/T meritve omenjenih anten.

Ker je Lunin zorni kot širši od -3dB širine snopa antene (HPBW), je narejena celovita analiza korekcijskega faktorja za uporabo porazdeljenega vira. Na podlagi tega je identificirana najbolj učinkovita metoda približka korekcijskega faktorja za omenjene antene. Uvedena je tudi najbolj prilegajoča metoda ocene HPBW z ciljem preverjanja izmerjenih vrednosti.

Predlagani postopek merjenja G/T kakovostnega faktorja je bil preverjen na operativni 11 metrski Cassegrain anteni v frekvenčnem pasu X, ki se uporablja za pridobivanje podatkov s satelitov LEO (nizka Zemljina orbita). Rezultati dobljeni z uporabo omenjene predlagane metode so dali konsistentne in točne ocene G/T faktorja v skladu s pričakovanji. Dodatna potrditev veljavnosti postopka je dana s primerjanjem dobljenih rezultatov in izmerjenega G/T faktorja z uporabo radio zvezde Cassiopeia A kot RF izvora.

**Ključne besede:** G/T, frekvenčni pas X, Luna, satelitske komunikacije, korekcijski faktor razširjene velikosti vira

\*Corresponding Author's e-mail: darko.sekuljica@gmail.com

### 1 Introduction

The antenna power Gain over system noise Temperature ratio (G/T), sometimes also labelled as "figure of

merit", can be regarded as a quality factor used to indicate the ground station capability to discriminate between signal and noise in a radio communication sys-

tem [1]. The higher the ratio, more efficient the ground station is in receiving a weak signal.

At the European Space Agency, as a part of the standard requirements for Earth Observation Satellites acquisition service contracts, a minimum G/T ratio is always specified to ensure the service is capable of properly acquiring uncorrupted data. Periodic measurements of the G/T are therefore required to ensure that the antennas selected to deliver the service maintain the required performance.

Typical antennas, for the purposes of Earth Observation (EO) satellite data acquisition, are receiving X-band with a main reflector aperture in the range of 7 to 13 meters. These ground station antennas perform routinely full elevation and azimuth rotations and accelerations which, beside the wind and gravity effects, add to the possibility of antenna distortions.

Because of their intense use, the antennas are constantly operational with small allotments of time available for performing the G/T measurements. Short pauses between satellite passes and frequent performance verifications require an accurate, efficient and time saving G/T measurement method.

Considering the antenna size range of interest, and the corresponding far field region distance, the optimal RF source has to be found in the skies. Direct G/T measurement using the Moon as an RF source, for the antenna size range of interest, has been selected and elaborated in this paper, providing a simple, fast and highly accurate G/T quality factor estimation method.

This paper is organized as follows. In Section II, the analysis of the available celestial sources has been described. Direct G/T calculation procedure, correction factor analysis and concerns from practical point of view are given in Section III. Section IV presents detailed G/T measurement procedure and the quality factor measurement results obtained with an operational 11 meter X-band antenna located at the e-GEOS station in Southern Italy. Finally, Section V draws some conclusions.

## 2 Analysis of the adequate available sources

For the antenna size range of interest in the X-band, the far-field region determined by the Fraunhofer's distance, results always more than 2.5km from the antenna location. In that case, terrestrial measurements with a distant antenna set as a source are highly im-

practical due to the terrain variety, high multi-path and various man-made or natural sources. Therefore, celestial sources were considered. As the measurement procedure must be valid and applicable for any antenna location, the selected source has to be well-defined and frequently visible.

The most obvious celestial sources are geostationary satellites, and natural sources like Sun, Moon and radio stars. Unfortunately, commercial geostationary satellites operating in the X-band, with well-known characteristics are uncommon. Hence, geostationary satellites could not have been taken as a suitable RF source. The strongest celestial natural source observed from Earth is the Sun. However, the Sun is subject of a possible and unpredictable variations with time due to Sun storms and Sun bursts [2, 3]. These variations, along with the extended source size of the Sun in respect to the antenna's HPBW, can introduce a significant uncertainty in the final quality factor estimation.

Radio star flux densities have been well-defined in [4, 5, 6]. For the antenna size range of interest, 7-13 meters, a radio star can be considered a point-like source. The latter means that using a radio star as an RF source in G/T measurement minimizes the error introduced by using G/T correction factors. However, the brightness of radio stars is much lower than those of the Sun or the Moon. For X-band antennas with reflector diameter smaller than 18m [7], using a direct G/T measurement method with radio stars may introduce significant uncertainties. These uncertainties, and consequently the errors in G/T estimation, are caused by the very small Y-factor, i.e. the ratio between the received noise power while pointing at the radio star, and the received noise power while pointing at the cold sky.

The Moon's radiation can be modelled with the black-body radiation that changes with the lunar phases and the Earth-Moon geometry. Y-factor readings using the Moon as a source are well above 1dB for the antennas of interest. Considered as a black-body, the Moon's radiation can be efficiently approximated as the radiation from a uniform brightness disk, introducing minimal errors [8, 9] in G/T estimation. Uniform brightness disk flux density approximation depends on the Moon's solid angle that changes with Earth-Moon geometry, and on the average brightness temperature of the Moon. For the X-band, it can be approximated using the Rayleigh-Jeans law:

$$S_{Moon} = \frac{2f^2 k_B T_{Moon}}{c_0^2} \Omega_{Moon} \quad (1)$$

where  $S_{Moon}$  is black-body flux density given in  $[W m^{-2} Hz^{-1}]$ ,  $f$  is the frequency in  $[Hz]$ ,  $k_B$  is Boltzmann constant

given with  $k_b \cong 1.38 \cdot 10^{-23}$  [m<sup>2</sup> kg s<sup>-2</sup> K<sup>-1</sup>],  $c_0$  [m s<sup>-1</sup>] is the speed of light, and  $\Omega_{Moon}$  is the Moon's solid angle in [sr].

The Moon average brightness temperature  $\overline{T_{Moon}}$  [K], is a function of the frequency, lunar phase and solar mean anomaly. In this paper, the yearly variation in the solar irradiation at the lunar surface due to the Earth's eccentric orbit has been neglected. Approximation of the Moon's average brightness temperature has been given by [8, 9]:

$$\overline{T_{Moon}} = \overline{T_0} \left[ 1 - \frac{\overline{T_1}}{\overline{T_0}} \cos(\phi - \psi) \right] \quad (2)$$

In the above equation,  $\overline{T_0}$  represents the constant brightness temperature term expressed in [K],  $\overline{T_1}$  is the first harmonic of the brightness temperature given in [K],  $\phi$  is the lunar phase angle in degrees and  $\psi$  is the phase lag in degrees [°]. In case that the lunar phase angle is in the decreasing cycle, a value of  $\phi' = 360 - \phi$  should be used in the Equation (2) calculation. According to [8] the error introduced using the approximation of the Moon's average brightness temperature given by the Equation (1) is less than 0.18%.

The values  $\overline{T_0}$  [K],  $\overline{T_1}$  [K],  $\psi$  [°] and the ratio  $\overline{T_1} / \overline{T_0}$ , were determined from accurate radio measurements at few selected frequencies and have been interpolated in between [8, 9]. Given parameters can be estimated using the following interpolation equations depending on the frequency of interest  $f_{GHz}$  given in [GHz]:

$$\begin{aligned} \overline{T_0} &= 207.7 + \frac{24.43}{f_{GHz}} \\ \frac{\overline{T_1}}{\overline{T_0}} &= 0.004212 \cdot f_{GHz}^{1.224} \\ \psi &= \frac{43.83}{1 + 0.0109 f_{GHz}} \end{aligned} \quad (3)$$

The Moon ephemeris, as are lunar angular diameter, lunar phase and other parameters depending on the observer location and on the current orbital positions of the Earth, Moon and Sun are provided by NASA web interface in [10].

The Moon's flux density dependence on the lunar angular diameter and on the lunar phase are shown on the Figure 1 and Figure 2. Both results were calculated for the frequency of interest  $f = 8.1775$  [GHz], and individually presented with the fixed lunar phase angle of  $\phi = 240^\circ$  and the fixed angular diameter of  $\theta_{Moon} = 0.5^\circ$  respectively.

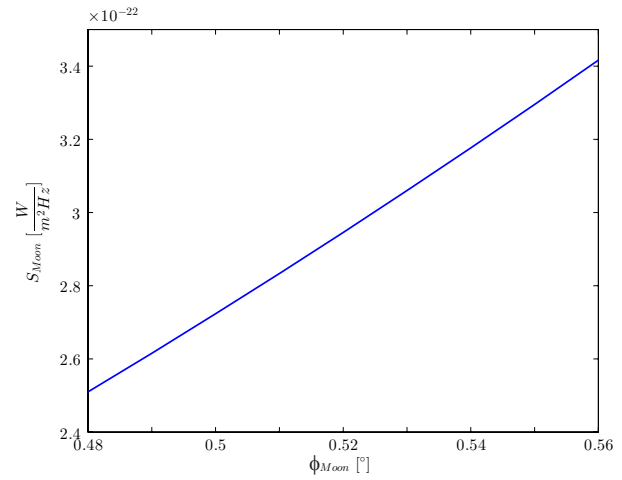


**Figure 1:** Lunar flux density change with angular diameter

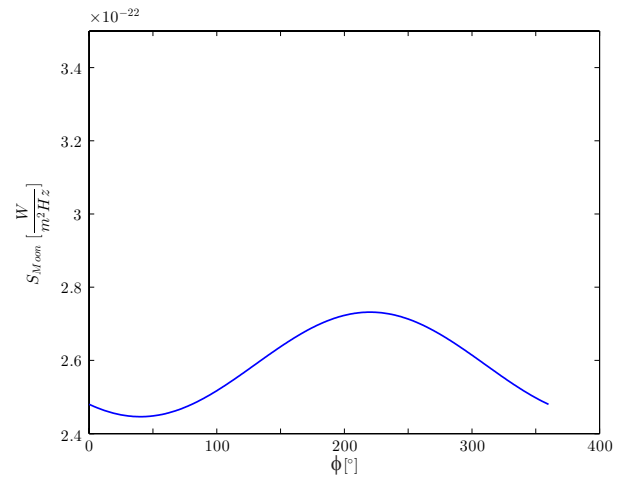


**Figure 2:** Lunar flux density change with phase angle

### 2.1 Uncertainties and proposed RF source

The overall G/T measurement uncertainty is given “in quadrature” and presented for the Moon, the Sun and the radio star Cassiopeia A [5, 7, 8, 11]:

**Table 1:** G/T measurement uncertainties

	Moon	Sun	Cassiopeia A
S	0.33 dB	0.3 dB *	0.1 dB
Y-factor	0.1 dB	0.1 dB *	1 dB
K <sub>1</sub>	0.05 dB	0.05 dB	0.05 dB
K <sub>2</sub>	0.2 dB	0.2 dB	0.01 dB
G/T	0.4 dB	0.38 dB *	1 dB

It must be noted that values in the Table 1 represent the G/T uncertainties due to the flux density  $S$ , the Y-factor and correction factors  $K_1$  and  $K_2$ , not their uncertainties themselves. Also, the (\*) sign marks that the possible

sunspot contribution is not considered because of its complicated computability.

Considering the Moon’s good stability, high flux density and low uncertainty, it has been selected as the most adequate source for an accurate G/T measurement, for parabolic antennas with reflector sizes in the range of 7-13 meters.

### 3 G/T direct measurement method

G/T direct calculation method requires a measurement of two well-defined signal sources [12]. Hence, the measurement is obtained by received noise power readings when the antenna is pointing at i) the Moon -  $P_{Moon}$  [W Hz<sup>-1</sup>], and ii) the cold sky -  $P_{sky}$  [W Hz<sup>-1</sup>]. Derivation of the G/T direct calculation method equation can be found in [13], while the final expression for the direct G/T quality factor calculation, expressed in [K<sup>-1</sup>], is given with the Equation (4):

$$\frac{G}{T}(\theta_i) = \frac{8\pi k_B (Y(\theta_i) - 1)}{\lambda^2 \cdot S_{Moon}} \cdot K_1 \cdot K_2 \quad (4)$$

where  $k_B$  [m<sup>2</sup> kg s<sup>-2</sup> K<sup>-1</sup>] is Boltzmann constant,  $S_{Moon}$  [W m<sup>-2</sup> Hz<sup>-1</sup>] is the Moon’s flux density,  $\lambda$  [m] is the wavelength of interest, and  $Y$  represents the well known Y-factor noise power ratio given in linear scale.  $K_1$  and  $K_2$  are correction factors due to atmospheric attenuation and extended source size respectively. Finally,  $\theta_i$  is the elevation angle at which the measurement was performed.

Atmospheric attenuation for the X-band is very low, and is mostly composed of the attenuations due to gases, water vapour and scintillation. Those attenuations can be efficiently estimated using advanced mathematical models given in [15, 16, 17, 18]. However, the estimation of attenuations caused by fog, rainy clouds, and precipitation is based on empirical and static models. Therefore, the measurements should be performed in clear sky conditions. The correction factor for the atmospheric attenuation is expressed in linear scale and given as a sum of the attenuation contributors. Impact of the atmospheric attenuation correction on the final G/T quality factor calculation can be within few tenths of decibel, whereas the impact of the extended source size correction can result in few-decibel change of the final G/T quality factor calculation. The extended source size correction factor  $K_2$  is therefore a factor of great importance when using the Moon as an RF source in G/T measurements, and will be further discussed in a separate subsection.

#### 3.1 Elevation angle adjustment

The measurement of G/T quality factor, using the Moon as an RF source, is performed at different elevation angles, depending on the Moon’s ephemeris. Therefore, it was important to establish a reference elevation angle, to which all measurement results will be adjusted. This was done in order to provide more realistic results and to allow mutual comparison of the results.

A reference value for the G/T measurement elevation angle adjustment was chosen to be the elevation of  $\theta_{REF} = 5^\circ$  measured from the local horizon [13]. This reference value adjusts a G/T quality factor for the worst case scenario, i.e. minimum elevation angle for satellite data acquisition, providing the most relevant G/T quality factor result. The antenna power gain  $G$  is a property of the antenna and is constant with elevation angle variation. Therefore, the G/T quality factor values can be adjusted by noting that the variation of G/T factor with elevation angle is equal to the variation of the cold sky noise power with elevation angle:

$$\frac{\frac{G}{T}(\theta_i)}{\frac{G}{T}(\theta_{REF})} = \frac{\frac{G}{T_{sys}(\theta_i)}}{\frac{G}{T_{sys}(\theta_{REF})}} = \frac{T_{sys}(\theta_{REF})}{T_{sys}(\theta_i)} = \frac{P_n(\theta_{REF})}{P_n(\theta_i)} \quad (5)$$

Where  $G/T(\theta_i)$  is the quality factor value obtained for the elevation angle at the moment of measurement, and  $G/T(\theta_{REF})$  is the quality factor value adjusted to the reference value  $T_{sys}$  and  $P_n$  are the system noise temperature and the received noise power respectively, given for both measurement and reference elevation angles. The ratio of  $P_n(\theta_i)$  and  $P_n(\theta_{REF})$  can be labelled as  $K_{EA}$  and can be expressed both in linear and logarithmic scale, yielding a shortened expression of the adjusted G/T quality factor:

$$K_{EA} = \frac{P_n(\theta_i)}{P_n(\theta_{REF})}$$

$$\frac{G}{T}(\theta_{REF}) = \frac{G}{T}(\theta_i) \cdot K_{EA} \quad (6)$$

$$\left[ \frac{G}{T}(\theta_{REF}) \right]_{dB} = \left[ \frac{G}{T}(\theta_i) \right]_{dB} + [K_{EA}]_{dB}$$

#### 3.2 Extended source size correction factor

The radio source whose angular diameter exceeds one fifth of the antenna’s half power beamwidth (HPBW) is considered an extended radio source. Each portion of

the RF source contributes to the received noise power according to the antenna radiation pattern. In the case of extended source, the peak of the antenna beam is assumed to be aligned with the center of the source, while the edges of the source are received by parts of the antenna beam with lower gain. This can result in the measured noise power smaller than what would be expected for the antenna's effective collecting area and the aperture illumination [19]. Therefore it is necessary to correct the measurement by the extended source size correction factor  $K_2$  given by [13]:

$$K_2 = \frac{\int_0^{2\pi} \int_0^{\frac{\theta_{Moon}}{2}} B(\theta, \phi) \sin(\theta) d\theta d\phi}{\int_0^{2\pi} \int_0^{\frac{\theta_{Moon}}{2}} B(\theta, \phi) g(\theta, \phi) \sin(\theta) d\theta d\phi} \quad (7)$$

Where  $\theta_{Moon}$  [°] is the Moon's angular diameter,  $B(\theta, \phi)$  [ $W m^{-2} sr^{-1} Hz^{-1}$ ] is the Moon's brightness distribution, and  $g(\theta, \phi)$  is the antenna radiation pattern normalized to the maximum directivity value, given in the linear scale.

Considering the Moon's radiation as that from a uniform brightness disk, the expression of the  $K_2$  correction factor can be simplified as:

$$K_2 = \frac{\int_0^{2\pi} \int_0^{\frac{\theta_{Moon}}{2}} \sin(\theta) d\theta d\phi}{\int_0^{2\pi} \int_0^{\frac{\theta_{Moon}}{2}} g(\theta, \phi) \sin(\theta) d\theta d\phi} \quad (8)$$

This approximation restricts measurement window to during the near full Moon phase. However, the integration over the antenna's radiation pattern is a rather complicated task and some alternative methods will be presented. Using the Moon as an RF source, the ratio of angular source size to the antenna's HPBW is less than 3, which makes it possible to obtain a good approximation of the normalized antenna radiation pattern using the normalized Gaussian far-field radiation pattern. The normalized Gaussian approximation of a radiation pattern, and the derivation of the  $K_2$  correction factor expression using the Gaussian pattern, are presented in [20, 13]:

$$K_2 = \frac{\ln(2) \left( \frac{\theta_{Moon}}{\theta_{HPBW}} \right)^2}{1 - e^{-\ln(2) \left( \frac{\theta_{Moon}}{\theta_{HPBW}} \right)^2}} \quad (9)$$

The approximated  $K_2$  correction factor depends on the Moon's angular diameter  $\theta_{Moon}$  [°] and the antenna's HPBW  $\theta_{HPBW}$  [°]. While the Moon's angular diameter can

be easily obtained on [10], the antenna's  $\theta_{HPBW}$  has to be properly measured.

For the purpose of the HPBW verification, the well known estimation expression was used [21]:

$$\theta_{HPBW} = k \cdot \frac{\lambda}{d} \quad (10)$$

where  $\lambda$  is wavelength in [m],  $d$  is the antenna reflector diameter in [m] and  $k$  is the antenna beamwidth factor. In the published literature, it is possible to find different definitions of the beamwidth factor, like  $k = 70$  in [22], and  $k = 65$  in [21]. However, the beamwidth factor is dependent on the feed's edge-tapering and cannot be approximated with a constant value. For that purpose, using the reflector antenna analysis software GRASP, numerous radiation patterns for the antenna range of interest were produced. Beside changing the antenna reflector size, the edge tapering was also varied. The feed used in the simulations was a Gaussian beam pattern feed. Results were then analysed and extrapolated in order to find a best fitting expression for bandwidth factor definition:

$$k = 58.96(1 + 0.0107 \cdot T_e) \quad (11)$$

Where  $T_e$  represents the absolute value of the edge taper given in the logarithmic scale [dB].

Usually, the extended source size correction factor estimation method is provided by the antenna vendor in polynomial expression form. It represents the best fit for the specific antenna reflector sizes, and is given with relation to the frequency,  $f_{GHz}$  [GHz], and the Moon's angular diameter,  $\theta_{Moon}$ . An example of the polynomial  $K_2$  expression and corresponding coefficients can be found in [13].

The comparison of the  $K_2$  polynomial expression, with  $K_2$  correction factor expression using the Gaussian pattern and HPBW estimation equation, is presented in Figure 3 - Figure 5. The  $K_2$  factor values were calculated for Cassegrain antennas designed with the reflector diameters of: 5.4, 7.3, 9.1, 10.26 and 11.28 meters, and have been interpolated in between using the polynomial interpolation and then adjusted to the uniform circular aperture illumination ( $k = 58.96$  [14]). For the reference value, simulated radiation patterns were used in the general expression for the  $K_2$  correction factor, given by Equation (8). The purpose of this comparison has been to analyse the  $K_2$  approximation method's fit to the reference values for different edge tapering and antenna reflector sizes. Results presented in Figure 3 - Figure 5 were calculated for the frequency



of  $f_{GHz} = 8.1775$  [GHz], including blockage effect, with edge tapering of both  $T_e = -10$  dB and  $T_e = -15$  dB. On the figures, red curve presents the  $K_2$  reference value, blue curve presents the polynomial  $K_2$  expression, magenta curve presents the  $K_2$  values obtained with the Equations (9, 10) considering the beamwidth factor  $k = 70$ . Finally, the black curve presents the  $K_2$  values obtained with the Equations (9, 10) considering the novel beamwidth factor given with Equation (11).

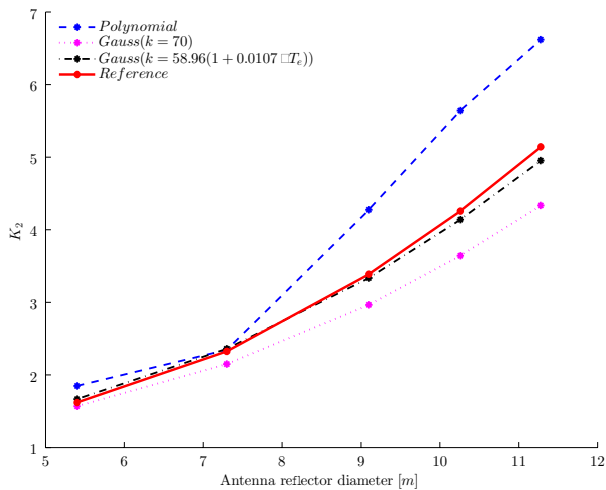


**Figure 3:** K2 approximation method comparison for Cassegrain antenna with  $T_e = -10$  dB and  $\theta_{Moon} = 0.56^\circ$ .

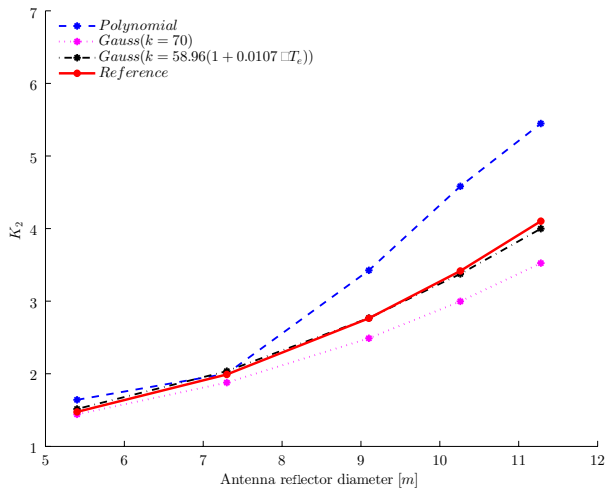


**Figure 4:** K2 approximation method comparison for Cassegrain antenna with  $T_e = -10$  dB and  $\theta_{Moon} = 0.5^\circ$

From the figures given above it can be observed that the polynomial approximation method diverges by the largest factor from the reference level. The divergence of the polynomial approximation is assumed to be due to possible double-shaping of the antenna reflectors. To estimate beamwidth factor in order to use Gaussian approximation for double-shaped antennas, the value

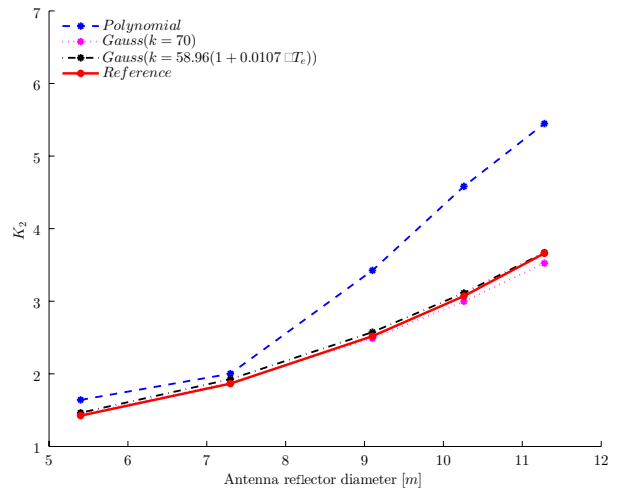


**Figure 5:** K2 approximation method comparison for Cassegrain antenna with  $T_e = -15$  dB and  $\theta_{Moon} = 0.5^\circ$

of uniform illuminated aperture  $k = 58.96$  can be taken for a rough estimation.

Also, it can be seen that the Gaussian approximation when beamwidth factor is given as  $k = 70$  yields significantly lower values than the reference. That beamwidth factor is probably suitable just for one specific edge tapering, usually used for the transceiver antennas.

It can be concluded that the Gaussian pattern approximation method for the  $K_2$  estimation is the best fitting  $K_2$  approximation method. Also, the HPBW approximation expression using the proposed bandwidth factor provides a good estimation, and therefore the verification value, for the antenna of interest HPBW. Finally, the polynomial approximation method values can be too optimistic resulting in significant error in G/T estimation.

Another important observation is that the polynomial approximation values, are constant for the antenna of interest, calculated for the optimal geometry antenna configuration. In case of antenna distortion the electrical properties of the antenna change. As a consequence, the extended source size factor value is reduced, and use of a constant  $K_2$  can introduce significant errors in the G/T quality factor estimation. Analysis of the possible discrepancies in G/T estimation using the constant  $K_2$  factor in case of antenna distortions has been made (Figure 6 - Figure 8).

For this purpose, every antenna was firstly designed and simulated for optimal performance. The  $K_2$  was in this case calculated with the numerical integration of the simulated antenna radiation pattern. This was done to neglect the uncertainties, as the scope of this test

is to provide an insight in problems occurring when using the constant correction factor values. Then, the radiation pattern simulation was performed for few axial displacements of the secondary reflector, in order to simulate antenna distortions. Therefore, the figures (Figure 6 - Figure 8) present the  $G/T$  quality factor results of: i) Optimal geometry antenna and optimal geometry antenna's  $K_2$  – green curve, ii) Distorted antenna keeping the optimal geometry antenna's  $K_2$  – red curve, and iii) Distorted antenna with  $K_2$  calculated for the distorted antenna – blue curve.

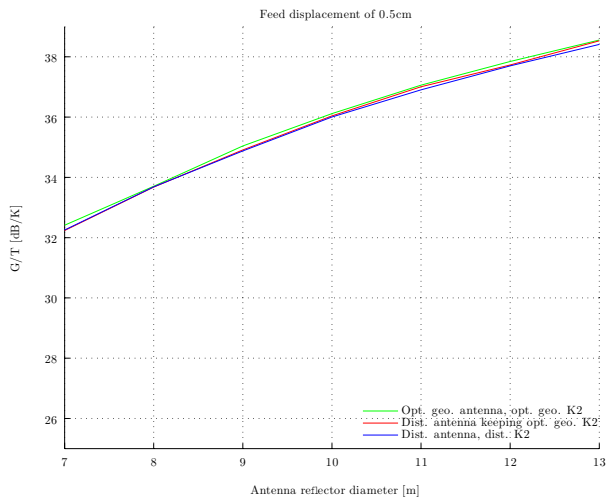


**Figure 6:** Secondary reflector displacement of 0.5 cm

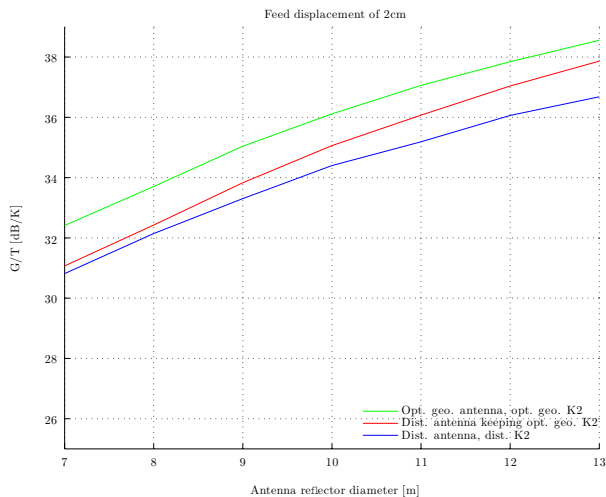


**Figure 7:** Secondary reflector displacement of 2 cm

It can be concluded that  $G/T$  estimation using the constant  $K_2$  factor value, for the antennas with efficiency degradation due to distortions, is too optimistic. Also, the real degradation of distorted antenna  $G/T$  quality factor, expressed in logarithmic scale, can be more than twice the  $G/T$  quality factor degradation using the constant  $K_2$  factor value.

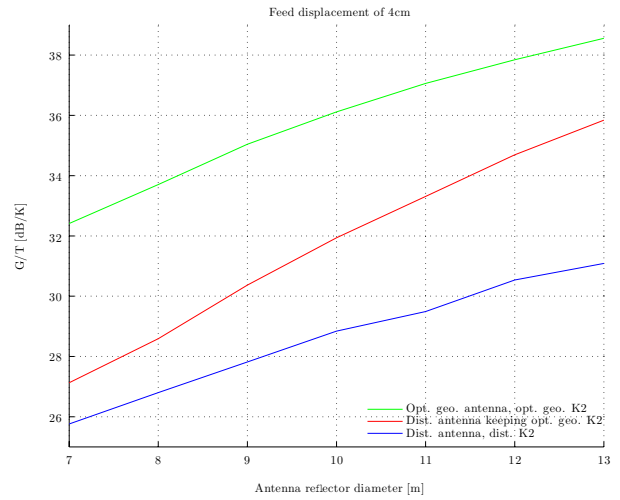


**Figure 8:** Secondary reflector displacement of 4 cm

## 4 Measurements

The measurement procedure is a result of detailed study and analysis, while the proposed settings for the spectrum analyser have been traded-off and selected in order to provide the best compromise between stability and measurement error. The measurements were performed on the operational 11m Cassegrain antenna, using the proposed procedure. Finally, obtained results were compared with well-defined  $G/T$  measurements using the radio star as a source.

### 4.1 Measurement procedure

To ensure the maximum possible Y-factor readings, it is advised performing the measurements in the days between waxing and waning Moon phase. The Moon's elevation should be higher than  $30^\circ$  to ensure that the sidelobes looking at the ground are 40 dB below the maximum directivity. Also, it should be verified that no other RF source is in the near vicinity of the Moon.

Before performing the set of measurements for  $G/T$  factor calculation, the antenna's horizontal and vertical radiation pattern cut should be measured. This is done to verify the antenna's HPBW, nulls and sidelobe behaviour. Measurement can be roughly performed letting the Moon pass over the antenna boresight. Then, the final check of the measured HPBW can be performed following the Equation (4).

Proposed spectrum analyser settings for the appropriate noise power readings are as follows:

**Table 2:** Proposed spectrum analyser settings

Center frequency	IF (typically 750 MHz)
Frequency span	0 Hz
dB/div	1
RBW	100 kHz
VBW	10 Hz
Marker	ON
Sweep time	100 ms
Average	10

Each measurement consists of three different values: i) On-source – received noise power when pointing the Moon, ii) Off-source – received noise power pointing the cold sky, at the same elevation and 5° tilt in azimuth, and iii) 5° elevation – received noise power pointing the cold sky at the elevation of 5°, and same azimuth as the Off-source measurement.

The measurements are repeated several times to minimize the Y-factor reading uncertainty. Correction factors and flux density are calculated using the methods described in this paper, and finally, the average values in linear scale of Y-factor and  $K_{EA}$  values are used to estimate the G/T quality factor of measured antenna.

4.2 Performed measurements - Moon

Measurements were performed following the proposed procedure, first using the Moon and then using the Cassiopeia A radio star as a source, with the purpose of proposed method validation. The antenna under measurement is shown in Figure 9, and its characteristics are given in Table 3.

**Table 3:** Antenna characteristics

Type	Cassegrain
Frequency	f = 8.1775 GHz
Reflector diameter	d = 11.28 m
Approx. gain	G ≈ 57.5 dBi

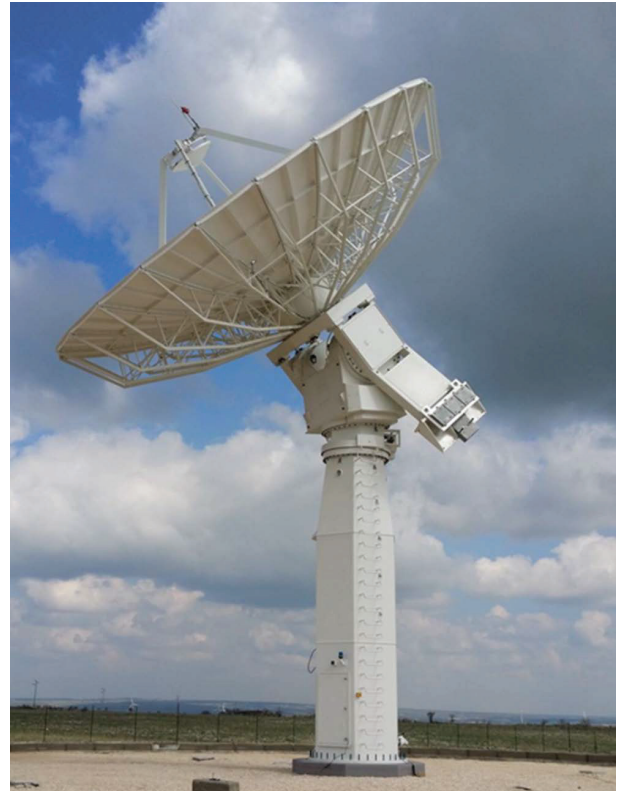


**Figure 9:** X-band ground station with d = 11.28 m

The Moon ephemeris were obtained from [10] in order to estimate its flux density, which is given in Table 4:

**Table 4:** Lunar ephemeris and flux density

Parameter	Value
$\overline{T_0}$	210.687 K
$\overline{T_1} / \overline{T_0}$	0.05515
$\overline{T_{Moon}}$	214.0622 K
$\Psi$ (lunar phase leg)	40.243 °
$\overline{\phi}$ (average lunar phase angle)	147.114 °
Lunar phase cycle	Increasing
$\overline{\theta_{Moon}}$ (lunar angular diameter)	0.549 °
$S_{Moon}$ (lunar flux density)	$3.1710^{-22} \text{ W m}^{-2} \text{ Hz}^{-1}$

**Table 6:** Measurement results with Moon as a source

	Time (UTC) [hh:mm]	Elevation [°]	On-source [dBm]	Off-source [dBm]	5° elevation [dBm]
Set 1	19:23	40.30	-79.26	-82.87	-81.48
Set 2	19:28	40.66	-79.38	-82.90	-81.50
Set 3	19:31	40.75	-79.28	-82.87	-81.48
Set 4	19:33	40.91	-79.38	-82.90	-81.50
Set 5	19:36	40.98	-79.34	-82.87	-81.59
Set 6	19:38	41.04	-79.30	-82.85	-81.60

The atmospheric attenuation correction factor was calculated using the local weather data at the time of the measurement, according to the latest ITU-R recommendation. Extended source size correction factor, however, is calculated using the measured antenna's HPBW, and the Gaussian pattern  $K_2$  approximation expression. Measured HPBW has been verified with the proposed beamwidth approximation equation. Both correction factors are given in Table 5.

**Table 5:** Local weather information and correction factors

Parameter	Value
Weather	Cloudy
Date	13.10.2016
Local Temperature	14.9 °C
Local Humidity	91 %
Local Pressure	960.9 hPa
$K_1$	1.033
$\theta_{HPBW}$	0.19 °
$K_2$	5.71

The next step was to perform the measurements of the Y-factor following the proposed procedure. Measurement was repeated six times and the results are given in Table 6.

Finally it was possible to estimate the G/T quality factor for the antenna under measurement.

**Table 7:** Quality factor estimation using the Moon as a source

Parameter	Value
Y-factor average	2.266
$K_{EA}$ average	0.733
G/T	4457 K <sup>-1</sup>
$[G/T]_{dB}$	36.5 dBK <sup>-1</sup>
G/T uncertainty	0.4 dB

Polynomial expression for  $K_2$  correction factor depending on frequency and Moon's angular diameter provided the

**Table 9:** Measurement results with Cassiopeia A as a source

	Time (UTC) [hh:mm]	Elevation [°]	On-source [dBm]	Off-source [dBm]	5°elevation [dBm]
Set 1	17 : 28	57.30	-83.25	-83.63	-82.75
Set 2	17 : 31	57.60	-83.32	-83.66	-82.76
Set 3	17 : 33	57.90	-83.29	-83.65	-82.74
Set 4	17 : 36	58.30	-83.28	-83.64	-82.71
Set 5	17 : 38	58.60	-83.26	-83.61	-82.69
Set 6	17 : 42	58.90	-83.28	-83.64	-82.71

result of  $K_2 = 6.35$ . Including the polynomial expression  $K_2$  value to the final G/T calculation using the Moon as a source yields the result  $[G/T]_{dB} = 37$  dBK<sup>-1</sup>. Using the polynomial expression, the  $K_2$  measurement uncertainty is not known.

#### 4.3 Performed measurements – Cassiopeia A

Measurements using Cassiopeia A as a source were performed following the same measurement procedure using the same spectrum analyser. Cassiopeia A has very-well defined flux density and decay factor described in [5, 23]. The weather information at the time of measurement, Cassiopeia A flux density, and corresponding correction factors are presented in Table 8.

**Table 8:** Local weather information and correction factors

Parameter	Value
Weather	Clear
Date	19.10.2016
Local Temperature	14 °C
Local Humidity	90 %
Local Pressure	960 hPa
$K_1$	1.012
$\theta_{Cas A}$	0.0767 °
$\theta_{HPBW}$	0.19 °
$K_2$	1.0565
$S_{Cassiopeia A}$	401.56·10 <sup>-26</sup> W m <sup>-2</sup> Hz <sup>-1</sup>

The measurements using the Cassiopeia A as a source are presented in Table 9, while the G/T quality factor estimation is presented in Table 10.

**Table 10:** Quality factor estimation using the Cassiopeia A as a source

Parameter	Value
Y-factor average	1.086
$K_{EA}$ average	0.811
G/T	4794 K <sup>-1</sup>
$[G/T]_{dB}$	36.8 dBK <sup>-1</sup>
G/T uncertainty	1 dB



From the presented results it can be observed that the estimation of  $G/T$  quality factor value using Cassiopeia A as a source, provides  $G/T$  value higher than when using the Moon as a source for 0.3 dB. However, also the uncertainty of  $G/T$  calculated value is much higher than when using the Moon as a source.

For the small angular diameters as is the case with the Cassiopeia A radio star, the polynomial expression is not valid.

## 5 Conclusions

In this paper, an accurate and time effective method for  $G/T$  quality factor measurement using the Moon as an RF source has been described. The Moon was selected as the most adequate RF source for the antennas of interest, because of its stable radiation flux density and low introduced uncertainty. The proposed method is considered valid for parabolic antennas with the reflector apertures ranging from 7 to 13 meters. In case of smaller size antennas, the  $Y$ -factor readings using the Moon fall under 1dB introducing larger uncertainties. For antennas of larger sizes, however, the  $K_2$  factor uncertainty becomes dominant resulting in significant possible  $G/T$  estimation error and in that case a star radio source becomes the preferred option.

As the Moon results to be an extended source for the antennas of interest, the important achievement was to propose an improved method to compute the extended source size correction factor. The improvement of a well-known  $K_2$  expression is given with polynomial expression for more accurate estimation of measured HPBW. This aspect turned out to be of key importance because a small error in the correction factor can result in an error of several tenths of a decibel in the final  $G/T$  value.

Results have shown that the best correction factor estimation can be obtained using a Gaussian pattern approximation. Also, it turned out that other estimation methods, such as the use of a fixed polynomial expansion, are often too optimistic.

Besides, by providing a constant correction factor value for the antenna of interest, these methods are hiding possible degradations of the  $G/T$  quality factor in case of antenna efficiency degradations. Results have shown that the real degradation of distorted antenna quality factor expressed in dB can be more than twice the degradation using a constant correction factor value. Proposed method uses the measured HPBW value confronted with the proposed polynomial expression,

both for verification and for precision value rounding to two digits.

The proposed direct measurement method is of great interest for the  $G/T$  measurements of typical X-band LEO satellite reception ground stations that have small pauses between satellite acquisitions.

Some measurements taken on an operational X-band Cassegrain antenna 11 m antenna have been presented to confirm the model. Measurements were performed on site on a tight schedule and following the procedure given in this paper. Measurement results are consistent and in line with expectations, and have shown a good agreement with measurements made on the ground station using the Cassiopeia A as an RF source.

Based on the obtained results, the European Space Agency (ESA/ESRIN) has updated the procedure used for periodic  $G/T$  measurement, using the method described in this paper.

## 6 Acknowledgments

The authors would like to express their gratitude to Paolo Rutigliano and Michele Paradiso of e-GEOS for the opportunity they provided to participate in their periodic  $G/T$  measurement campaign, and for the practical knowledge they shared during the process.

## 7 References

1. D. F. Wait, M. Kanda, W. Daywitt in C. Miller, "A study of the measurement of  $G/T$  using Cassiopeia A," tech. rep., DTIC Document, 1974.
2. W. C. Daywitt, "On 10-60 GHz  $G/T$  measurements using the Sun as a source: A preliminary study (Report, 1985-1986)." (1986).
3. D. A. Giudice, and J. P. Castelli, "The use of extraterrestrial radio sources in the measurement of antenna parameters." *IEEE Transactions on Aerospace and Electronic Systems* 2 (1971): 226-234.
4. M. Ott, et al. "An updated list of radio flux density calibrators." *Astronomy and Astrophysics* 284 (1994): 331-339.
5. J. W. M. Baars, et al. "The absolute spectrum of CAS A-an accurate flux density scale and a set of secondary calibrators." *Astronomy and Astrophysics* 61 (1977): 99-106.
6. E. Ekelman and C. Abler, "Antenna gain measurements using improved radio star flux density expressions," in *Antennas and Propagation Society International Symposium*, 1996. AP-S.

- Digest, volume=1, pages=172-175, year=1996, organization=IEEE.
7. D. F. Wait, M. Kanda, W. Daywitt and C. Miller, "A study of the measurement of G/T using Cassiopeia A," tech. rep., DTIC Document, 1974.
  8. W. C. Daywitt, "An error analysis for the use of presently available lunar radio flux data in broadbeam antenna-system measurements," *Error analysis for the use of presently available lunar radio flux data in broadbeam antenna-system measurements..* Report NBS-TN-1073, Natl. Bur. Stand., Washington, DC, USA, 30 pp., vol. 1, 1984.
  9. Z. Kopal, *Advances in astronomy and astrophysics*, vol. 3. Academic Press, 2013.
  10. JPL-NASA, "HORIZONS Web-Interface." Available at: <http://ssd.jpl.nasa.gov/horizons.cgi>. Accessed: 24. 10. 2016].
  11. W. C. Daywitt, "On 10-60 GHz G/T measurements using the Sun as a source: A preliminary study." *Report, 1985-1986 National Bureau of Standards, Boulder, CO. Electromagnetic Fields Div.* (1986).
  12. W. Welch and D. DeBoer, "Expected properties of the ATA antennas," *ATA Memo Series*, vol. 66, 2004.
  13. D. Šekuljica, "Using the Moon as a calibrated noise source to measure the G/T figure-of-merit of an X-band satellite receiving station with a large antenna 200...400 wavelengths in diameter" : *master's thesis*. Ljubljana: [D. Šekuljica], 2017. XVI, 116 str., ilustr. <https://repozitorij.uni-lj.si/lzpisGradiva.php?id=88902>. [COBISS.SI-ID 11686996].
  14. T. A. Milligan, *Modern antenna design*. John Wiley & Sons, 2005.
  15. ITU-R recommendation, "Attenuation by atmospheric gases," *ITU-R P. 676*.
  16. ITU-R recommendation, "Reference Standard Atmospheres," *ITU-R P. 835*.
  17. ITU-R recommendation, "Propagation data and prediction methods required for the design of Earth-space telecommunication systems," *ITU-R P. 618*.
  18. ITU-R recommendation, "Attenuation due to clouds and fog," *ITU-R P. 840*.
  19. A. Solovey in R. Mittra, "Extended source size correction factor in antenna gain measurements," in *Microwave Conference, 2008. EuMC 2008. 38th European*, pages=983-986, year=2008, organization=IEEE.
  20. H. Ko, "On the determination of the disk temperature and the flux density of a radio source using high-gain antennas," *IRE Transactions on Antennas and Propagation*, vol. 9, no. 5, str. 500-501, 1961.
  21. ITU, *Handbook on Satellite Communications (FSS)*. International telecommunication union, 2002.
  22. R. A. Nelson, "Antennas: the interface with space," *Via Satellite, Sep*, 1999.
  23. J. Baars, P. Mezger in H. Wendker, "The Spectra of the Strongest Non-Thermal Radio Sources in the Centimeter Wavelength Range.," *The Astrophysical Journal*, vol. 142, str. 122, 1965.

Arrived: 06. 04. 2017

Accepted: 26. 06. 2017



# *Reversible Data Hiding Based on Radon and Integer Lifting Wavelet Transform*

*A.Amsaveni<sup>1</sup>, P.T Vanathi<sup>2</sup>*

*<sup>1</sup>Kumaraguru College of Technology, Department of Electronics and Communication Engineering, Coimbatore, India*

*<sup>2</sup>PSG College of Technology, Department of Electronics and Communication Engineering, Coimbatore, India*

**Abstract:** This paper presents a reversible data hiding technique based on radon and integer lifting wavelet transform to secure the data transmitted over communication network. The technique focuses on three optimality criteria, namely imperceptibility, robustness, and reversibility. The frequency domain strategy is applied due to its superior performance over the spatial domain techniques in certain important aspects like robustness and reversibility towards signal processing and image processing operations. The cover image is first transformed from spatial domain to radon domain and then, this radon image is applied with integer lifting wavelet transform. As the Radon transform performs rotation, scaling and translation operations on the cover image, it changes the locations of the secret bits. Hence, it is very difficult to detect the embedded data without taking the inverse Radon transform and subsequently, it increases the security of the embedded payload. The integer lifting wavelet transform guarantees complete reversibility as they produce integer wavelet coefficients. Then, the middle bit planes of high frequency lifting coefficients are compressed using arithmetic coding to provide space for embedding secret payload. As the proposed framework embeds data in red, green, and blue channels, it can work well for a variety of images with different distribution of colors.

**Keywords:** reversible data hiding; radon transform; integer lifting transform; bit plane coding; arithmetic coding

## *Reverzibilno skrivanje podatkov na osnovi Radonove in diskretne valčne transformacije*

**Izveček:** Članek opisuje tehnike reverznega skrivanja podatkov na osnovi Radonove in diskretne valčne transformacije za varovanje podatkov preko omrežja. Tehnika sloni na trhe kriterijih: neopaznost, robustnost in reverzibilnost. Uporabljena je strategija na osnovi frekvence saj prednjači pred prostorsko tehniko v ključnih točkah robustnosti in reverzibilnosti obdelave signalov in slik. Slika je najprej pretvorjena v radon proctor in nato še z diskretno valčno transformacijo. Radonova transformacija opravi rotacijo, skaliranje in translacijo in spremeni lokacijo skrivnih bitov. Brez inverzne transformacije je skoraj nemogoče odkriti skrite podatke. Valčna transformacija zagotavlja popolno reverzibilnost in določi valčne koeficiente, ki so stisnjeni z aritmetičnim kodiranjem. Predlagan postopek vsebije morer, zelen in rdeč kanal, tako da je uporaben za številne slike.

**Ključne besede:** reverzibilno skrivanje podatkov; radonova transformacija; diskretna valčna transformacija; kodiranje bitne ravnine; aritmetično kodiranje

\* Corresponding Author's e-mail: [amsaveni.a.ece@kct.ac.in](mailto:amsaveni.a.ece@kct.ac.in)

### *1 Introduction*

Securing data transmitted over the internet has become a challenging issue caused by the advancement in data digitization and communication networking over the past decade. Therefore, it is necessary to devise strategies to secure information during the process of information exchange. Reversible data hiding

has emerged as a major research area due to the phenomenal growth in internet and multimedia technologies. It involves concealing confidential data within another seemingly innocuous cover media such as text, video, audio, images, and compression coding [1].



Basic terminologies used in data hiding are as follows: *Secret Payload* – Message to be embedded in the cover image; *Cover image* – Image that carries the secret message; *Stego image / Embedded image* – Cover image after embedding the secret payload (Cover image + Secret data); *Imperceptibility* – Measure of distortion which is caused by embedding the secret message in the original cover image. It is the inability of the human eye to differentiate between the cover image and the embedded image. Generally, embedded images with higher imperceptibility are preferred in data hiding; *Robustness* – Robustness is the ability of the secret payload to withstand various intentional attacks such as image processing operations and unintentional attacks such as addition of noise; *Embedding Capacity* – Data embedding rate or number of bits embedded per pixel, measured in terms of bits per pixel; *Security / Undetectability* – Any data hiding system may be considered as secure if the possibility of knowing the presence of a secret message in any cover medium is very difficult; *Attacks* – Process of revealing the hidden data from the embedded image by attacking with various signal processing and image processing techniques.

While embedding secret information in a cover image, the emphasis is on two key problems. The first one is to produce an embedded image with a tolerable level of quality so that the distortion produced due to data embedding is imperceptible. The second is to produce the embedded image that is distortion tolerant (robust), i.e., even if the embedded image is attacked during communication, the hidden data can be recoverable. Robustness of data hiding techniques can be enhanced if the properties of the cover image could be properly utilized. By considering these aspects, embedding data in frequency domain becomes more popular compared to spatial domain techniques [2]. The frequency domain techniques modify the frequency coefficients of the cover image by applying a specific transformation function on the cover image. They are designed to be imperceptible and robust against various geometrical transformations and external attacks.

Frequency domain schemes use transformation methods, such as integer cosine transform [3] or integer wavelet transform [4] to compute the transform coefficients of the cover image. Then, these coefficient values are modified to embed the secret data. In reversible data hiding technique based on DCT, one secret bit was embedded into two neighboring DCT coefficients in an image block [5]. The secret payload is embedded in the high frequency coefficients of discrete wavelet transform (DWT) by exploiting the statistical properties of the cover image [6]. The DWT works well against various image processing attacks. As it produces floating coefficients, embedded data is potentially lost while re-

constructing the cover image by inverse wavelet transform. This drawback is overcome by integer wavelet transform (IWT). The secret data is embedded into the middle frequency of the integer lifting wavelet domain by modifying the histogram of the cover image [7].

Data embedding is also performed in radon domain, which shows a considerable improvement in bit error rate. A radon-based approach was introduced to incorporate translation invariance properties to the payload [8]. RST invariant watermarking technique has been proposed by utilizing the Fourier transform and transforming them to log polar coordinates, which are quite flexible towards rotation, scaling and translation attacks [9].

Hybrid transform has been proposed based on the unique features of the transforms in the hybrid combination, so that it is able to address the robustness and reversibility criteria. Accordingly, the rotation, scaling and translation properties of the Radon transform and reversibility property of integer lifting transform have been joined together in a hybrid formation. The paper investigates a combinatorial data hiding approach using radon transform and integer lifting wavelet transform (ILWT). Radon transform ensures robustness and ILWT makes the algorithm reversible by using the lifting scheme on orthogonal and bi-orthogonal wavelets. The superiority of this combination is also tested and compared with the other existing works in literature. The proposed method improves the quality of embedded image as well as the robustness of embedded payload against various attacks compared to the existing methods.

This paper is organized as follows. Section 2 describes the Radon transform. Section 3 explains Integer Lifting Transform. Section 4 discusses the proposed algorithm. Section 5 presents the experimental results and, Section 6 concludes the paper.

## 2 Radon transform

Radon transform is a linear transform which is an effective method to analyze signal between the spatial domain and its projection space. It represents the image as a collection of projections along various directions [10]. It computes the projection of the image intensity along a radial line oriented at a specific angle. For each angle  $\theta$  and at each distance  $\rho$ , the intensity of a ray perpendicular to the  $\rho$  axis is summed up at  $R(\rho, \theta)$ . Radon transform converts rectangular coordinates  $(x, y)$  into polar coordinates  $(\rho, \theta)$ . The simplest form of discrete Radon transform is to select finite number of the

angular variable of projection, then to take the summation on the discrete image along the projection line.

As shown in Fig.1, the radon transform of a two dimensional function  $f(x, y)$  is the integral of function  $f$  along a straight line parallel to the  $y$ -axis, which is given by,

$$R_{\theta}(x') = \int f(x' \cos\theta - y' \sin\theta, x' \sin\theta + y' \cos\theta) dy' \quad (1)$$

Where 
$$\begin{bmatrix} x' \\ y' \end{bmatrix} = \begin{bmatrix} \cos\theta & \sin\theta \\ -\sin\theta & \cos\theta \end{bmatrix} \begin{bmatrix} x \\ y \end{bmatrix} \quad (2)$$

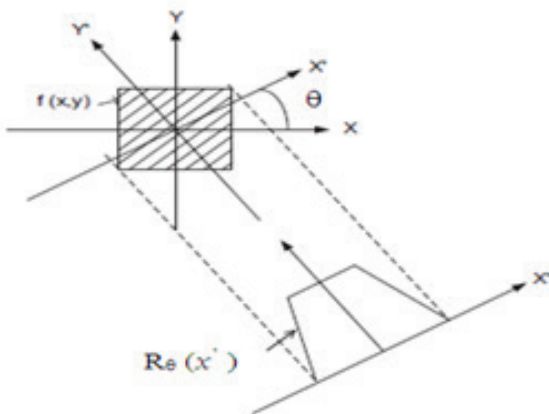


**Figure 1:** Geometry of the Radon transform

An efficient reversible data hiding method must be robust against a wide range of image processing operations such as image enhancement, cropping, rotation, scaling, compression, and signal processing operation such as addition of noise. However, conventional data hiding algorithms are more sensitive to geometric distortions. Hence, radon transform is introduced to perform rotation, scaling, and translation operations on the cover image. These operations change the positioning of the secret bits. Without taking inverse Radon Transform, it is very difficult to detect the embedded data and subsequently, this increases the security of embedded payload.

### 3 Integer lifting wavelet transform

There are many researches that have been explored using wavelets in the field of image processing and image steganography. The main advantage of wavelet is that they offer multi-resolution capability, which is similar to the operation of the human visual system. Wavelets provide an optimal representation of signals. Normally, wavelet-based data hiding gives better performance compared to other methods. As the conventional

wavelet transform performs a convolution of the input image and the wavelet basis, it requires large memory space for the computation process. The time taken and the large memory required for the conventional wavelet transform is reduced in the lifting method. Lifting transform is a technique used in constructing second generation wavelets entirely in the frequency domain. It is fast compared to the first generation wavelets, as it requires only addition and subtraction.

Conventional wavelet transform is not suitable for reversible data hiding scheme as reversibility property is not guaranteed. Wavelet transform operates on a floating-point arithmetic basis. An image that has integer intensity values in the spatial domain is converted into decimal wavelet coefficients. The wavelet coefficients are modified appropriately during data hiding operation and inverse wavelet transform is carried out to reconstruct the image in the spatial domain. A serious note here is that practically wavelet coefficients are truncated or rounded as it is not viable to represent the coefficients to its full accuracy. Information is potentially lost while reconstructing the image by inverse wavelet transform. But reversible data hiding schemes have to recover the host image without distortion along with the secret payload. Eventually, this makes the discrete wavelet transform a poor choice for reversible data hiding [11]. To address this specific issue, an invertible integer lifting wavelet transform is used in the proposed scheme. The system operates on integer arithmetic and alleviates the loss of any information via forward and inverse transforms [12].

The lifting wavelet transform decomposes the image into frequency subbands, which contain approximation and detail coefficients. The system reserves the detail coefficients, which have texture, edges, and region boundary for data hiding. It is an insensible region for human visual system. An advantage of the Lifting Scheme is that it can be converted easily into a transform that maps integers to integers while retaining the perfect reconstruction property. Thus, embedding data in integer lifting wavelet domain satisfies the properties like security, imperceptibility, and robustness of the proposed technique.

### 4 Bit plane embedding using binary arithmetic coding

The Binary Arithmetic Coding can be exploited for compressing the bit planes of grayscale/colour images. As arithmetic coding is a lossless compression method, it guarantees the recovery of original payload. In bit plane embedding, the most significant bits for each

CLH Header (16 bits)	CHL Header (16 bits)	CHH Header (16 bits)	CLH Length (16bits)	CHL Length (16bits)	CHH Length (16 bits)	Length of embed- ding data (32 bits)	Secret Payload
-------------------------	-------------------------	-------------------------	------------------------	------------------------	-------------------------	---	-------------------

**Figure 2:** Structure of the embedded bit plane

pixel are grouped into one bit plane, the next most significant bits into another bit plane and so on till the least significant bit plane. Mostly, the five highest order planes contain visually significant data. The other lower bit planes contain fine details in the image. Lesser the bit plane number, lesser is its contribution to the final stage.

Statistically, there is an equal distribution of zeroes and ones in the lower planes of the image than in the higher planes. This leads to lower compression ratio and lower embedding capacity in the lower bit planes than in the higher planes. This is because binary sequences of length L having higher probability may be encoded more compactly than another one of the same length with a lower probability. But the signal to noise ratio falls down as higher bit planes are altered for embedding [13].

The most significant bit plane contains the most critical approximation values of the image. Hence, modifications made in higher bit-plane may degrade the quality of the cover image. In order to have the embedded image visually as same as the cover image, data is hidden in one or more middle bit planes.

The bits in one or more bit-planes can be compressed to provide space to hide data like text or image due to the existence of redundant information. The ap-

proximate coefficients in the LL sub-band contribute to visual perception. Hence, the secret bits are embedded in LH, HL or HH subbands (Detail Coefficients). The original bits in the selected bit plane of LH, HL or HH subbands are compressed using arithmetic coding to provide space for embedding the payload bits.

The structure of the embedded bit plane is shown in Fig.2. CHH, CHL, and CLH headers represent the header information of the compressed HH, HL, and LH sub bands. They describe the bit distribution required for arithmetic encoder and decoder. CHH, CHL, and CLH lengths denote the length of the compressed bit stream in the chosen bit plane of the LH, HL, and HH subbands.

### 5 Proposed methodology

Majority of the methods discussed in the literature addressed only a few of the desired characteristics, namely lossless/reversible, imperceptible, high payload capacity and robustness, and not all. The proposed method of reversible data hiding is based on bit plane embedding in radon and integer lifting wavelet domain. It aims to meet all the desired characteristics to an optimal level. The block diagram of the proposed data embedding algorithm is shown in Fig.3.

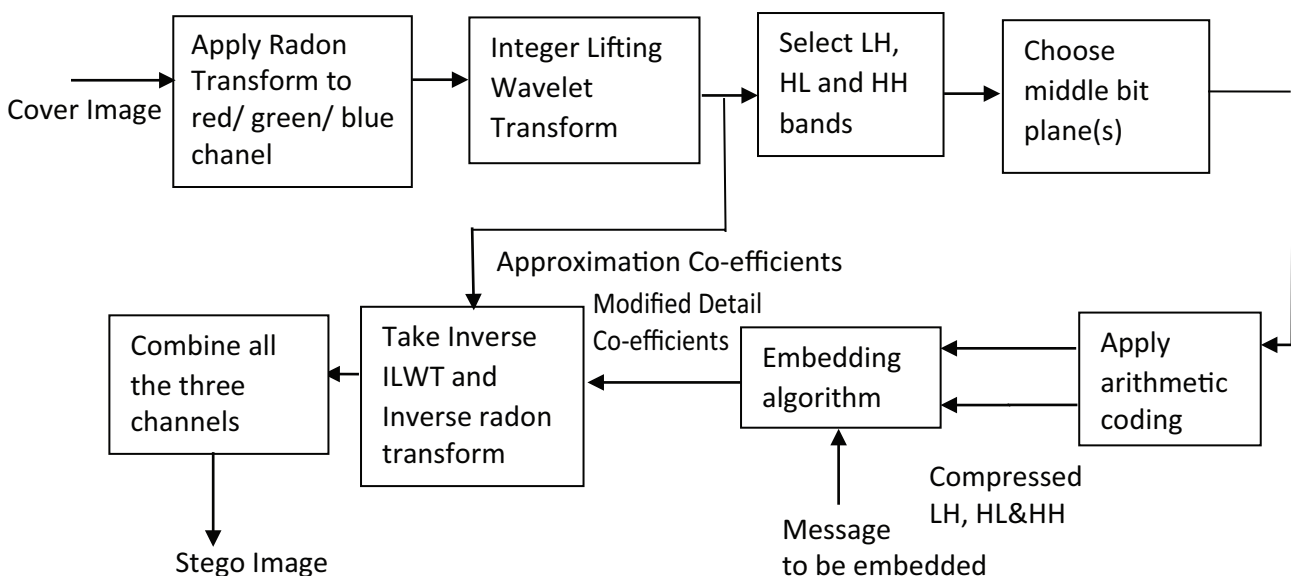


**Figure 3:** Block diagram of embedding process

### 5.1 Data Embedding Algorithm

**Input:** Cover image with M-rows and N-columns, Secret payload bits.

**Output:** Stego Image

Step 1: Read the cover image of size M x N.

Step 2: Separate color channels (Red, Green, and Blue) of the cover image.

Step 3: Apply radon transform on any one of the channels.

Step 4: Notice that Radon image undergoes a single level integer lifting wavelet transform which results in 4 subbands (LL, LH, HL, HH) of size M/2 x N/2, each.

Step 5: Construct binary images from the chosen bit planes of LH, HL, and HH bands.

Step 6: Compress the original bits in the chosen bit plane of these bands using arithmetic coding and obtain the header information required for the arithmetic encoder and decoder.

Step 7: Read the secret payload and convert it into a bit string.

Step 8: Concatenate the header length, header information, and compressed bit streams of CLH, CHL, and CHH and the secret payload to get a single bit stream.

Step 9: Embed bit stream into chosen bit plane of LH band. If not enough, embed in HL band and then in HH band and observe that it results in embedded LH, HL, and HH components.

Step 10: Apply inverse integer lifting transform on LL coefficients and the modified LH, HL, and HH coefficients.

Step 11: Compute inverse radon transform of the image obtained from Step 10.

Step 12: Combine all the three color channels to get stego image.

### 5.2 Data Extraction Algorithm

Step 1: Read the stego image of size M x N.

Step 2: Separate color channels (Red, Green, and Blue) of stego image.

Step 3: Apply radon transform to the channel in which the data is embedded.

Step 4: Notice that Radon image undergoes single level integer lifting wavelet transform which results in 4 subbands (LL, LH, HL, HH) of size M/2 x N/2, each.

Step 5: Construct binary images from chosen bit planes of LH, HL, and HH bands.

Step 6: Derive the header information and header length needed for arithmetic decoding.

Step 7: Extract the compressed bits from the chosen bit plane of these bands using arithmetic decoder and decompress the subbands to get the reconstructed subbands.

Step 8: Apply inverse integer lifting transform on the reconstructed subbands LH, HL, and HH along with LL subband.

Step 9: Compute inverse radon transform of the image obtained from Step 8.

Step 10: Combine all the three channels to get the original cover image.

## 6 Experimental results

In order to investigate the performance of the proposed data hiding algorithm, several experiments are carried out in a computer system equipped with Intel core 2 duo processor with 2 GB memory and a clock speed of 2 GHz. Matlab 8 (R2013a) platform is used for the digital simulation of the algorithm. Five standard 512 x 512 color images such as (a) *Airplane*, (b) *Baboon*, (c) *Boat*, (e) *Lena* and (e) *Pepper*, obtained from USC-SIPI (Image database), have been used as cover images. The performance of the algorithm is investigated in terms of imperceptibility, robustness, and reversibility.

### 6.1 Imperceptibility

The metrics used to test the imperceptibility property of the proposed algorithm are PSNR (Peak Signal to Noise Ratio) and SSIM (Structural Similarity Index Measure).

The PSNR for an image of size M x N is calculated by,

$$PSNR = 10 \log_{10} (255^2 / MSE) \text{ dB} \quad (3)$$

where,

$$MSE = \sum_{x=1}^M \sum_{y=1}^N (p(x, y) - p'(x, y))^2 \quad (4)$$

where  $p(x, y)$  stands for the pixel value in the cover image and  $p'(x, y)$  is the pixel value at position  $(x, y)$  in the stego image after embedding the secret message. M and N denote the number of rows and columns of the image and  $(x, y)$  denotes the pixel coordinates.

The quality of the stego image is also calculated using SSIM as follows:

$$SSIM = \frac{(2\mu_x\mu_y + c1)(2\sigma_{xy} + c2)}{(\mu^2_x + \mu^2_y + c1)(\sigma^2_x + \sigma^2_y + c2)} \quad (5)$$

where  $x$  and  $y$  are same size windows of the cover and stego images and  $\mu_x$  and  $\mu_y$  are corresponding  $x$  and  $y$  averages.  $\sigma^2_x$  and  $\sigma^2_y$  are the variances of  $x$  and  $y$  and



$\sigma_{xy}$  is the covariance of x and y. The positive constants  $c_1$  and  $c_2$  are included to avoid a null denominator. Typically  $c_1 = (k_1L)^2$ ;  $c_2 = (k_2L)^2$ ;  $L = (2^{\text{no.of bits/pixel}} - 1)$ ;  $[k_1, k_2] = [0.01, 0.03]$  by default.

Table 1 shows the PSNR and SSIM of cover images after embedding a payload of 10,000 bits using the wavelet *cdf2.4* (Cohen-Daubechies-Feauveau 2.4) in the fourth bit plane of Red, Green and Blue channels. As the PSNR obtained from the stego images is greater than 42 dB, the embedded payload is highly imperceptible to the human eye, i.e., the perceptual quality of the resultant stego images is good. The red channel offers better PSNR and SSIM compared to green and blue channels. The red channel gives an improvement in PSNR of about 2.0 to 7.0 dB over green and blue channels. Among all cover images, the *Airplane* image yields better PSNR for the same payload.

**Table 1:** Quality metrics

Cover image	PSNR (dB) and SSIM					
	Red Channel		Green Channel		Blue Channel	
	PSNR	SSIM	PSNR	SSIM	PSNR	SSIM
Airplane	47.70	0.9771	47.65	0.9867	46.70	0.9519
Baboon	43.29	0.9900	42.91	0.9704	42.49	0.9894
Boats	46.96	0.9921	43.23	0.9740	43.69	0.9693
Lena	45.87	0.9820	42.46	0.9780	43.46	0.9409
Pepper	46.86	0.9784	44.34	0.9840	42.39	0.9656

The Fig.4. shows the embedded images of size 512 x 512, after embedding a payload of 10,000 bits using *cdf2.4* in the fourth bitplane of red channel of standard images.

Table 2 summarizes the quality of the Lena image under varying payload, after embedding in the bit plane 4, 5, and 6 of red channel using wavelet *cdf2.4*.

**Table 2:** Embedding capacity Vs. PSNR (dB)

Secret payload (bits)	Embedding Rate (bpp)	PSNR (dB)		
		Bit Plane 4	Bit Plane 5	Bit Plane 6
1000	0.004	45.27	43.08	41.42
3000	0.011	45.26	43.07	41.40
6000	0.023	45.14	43.04	41.20
10,000	0.038	45.10	43.02	41.06
20,000	0.076	44.68	42.54	40.83
40,000	0.153	42.21	40.41	38.33
50,000	0.191	42.20	39.80	38.33
70,000	0.267	41.49	39.52	37.44
80,000	0.305	41.28	38.79	37.17

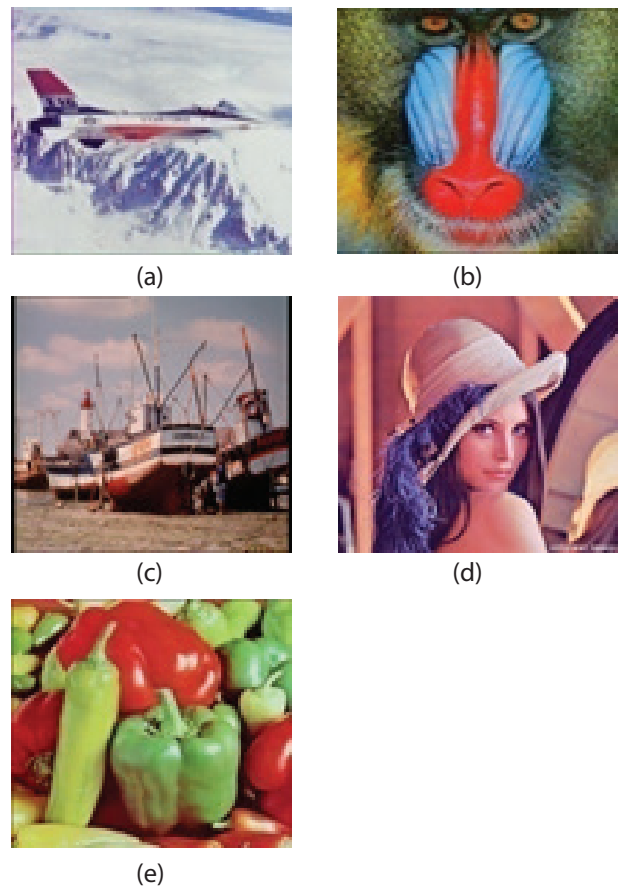


**Figure 4:** Standard color images of size 512 x 512 after embedding a payload of 10,000 bits (a) Airplane; (b) Baboon; (c) Boat; (d) Lena; (e)Pepper

86,000	0.328	41.16	38.72	37.13
90,000	0.343	Insufficient	38.64	37.11
95,000	0.362	Insufficient	Insufficient	37.04
96,000	0.366	Insufficient	Insufficient	Insufficient

The perceptual quality of cover image will get reduced if the data is embedded in higher bit planes and also PSNR drops down as more number of bits embedded in that plane. The bit plane 4 can accommodate only 90,000 bits as the bit plane 4 provides less space for data embedding compared to other bit planes. The maximum embedding capacity of bit planes 5 and 6 is 95,000 bits and 96,000 bits respectively. Beyond 95,000 bits, there is no space to accommodate the secret payload in both the bit planes. The embedding capacity completely depends upon cover image and is also based on the bit distribution of the chosen bit plane. The PSNR varies from 41.12 dB at the embedding rate of 0.004 bits per pixel to 37.04 dB at 0.362 bits per pixel for bit plane 6.

The experimental results of the proposed scheme are compared with the various schemes discussed in Tsai &

Sun [14], Fu & Shen [15], and Niu et al [16] and summarized in Table 3. The PSNR of the cover images is measured after embedding a payload of 10,000 bits in Red channel using the wavelet *cdf2.4*. The PSNR offered by the proposed scheme is about 15% greater than Niu et al scheme. The proposed scheme gives better PSNR for *Lena* image compared to *Baboon* and *Boat* images.

**Table 3:** Comparison of the proposed scheme with the schemes in the literature

Host image	PSNR (dB)			
	Tsai and Sun Scheme	Fu and Shen Scheme	Niu et al Scheme	Proposed Scheme
Lena	39.43	38.10	40.57	45.87
Baboon	41.76	38.90	41.67	43.29
Boat	42.49	39.72	40.71	44.03

### 6.2 Robustness

Robustness is measured using Bit Error Rate (BER) and is defined as:

$$BER = \sum_{k=0}^n b_k \oplus b'_k / N \tag{6}$$

where  $b$  and  $b'$  are embedded and extracted bits respectively,  $N$  is the total number of secret bits embedded and represents  $\oplus$  the XOR operation. The value of BER ranges between 0 and 1. If BER is closer to 1 then, it means that the error value of extracted data is higher. The value of BER is calculated after retrieving the secret data from the embedded block. Lower the BER%, higher is the accuracy of the extracted secret data.

**Table 4:** Effect of various attacks on BER

Attacks	Bit Error Rate				
	Airplane	Baboon	Boats	Lena	Pepper
Gaussian Noise ( $\sigma^2=0.2$ )	0.0032	0.0034	0.0035	0.0032	0.0034
Gaussian Noise ( $\sigma^2=0.4$ )	0.0036	0.0036	0.0037	0.0037	0.0038
Poisson Noise	0.0028	0.0030	0.0029	0.0030	0.0031
Impulse Noise ( $\sigma^2=0.05$ )	0.0017	0.0020	0.0021	0.0018	0.0022
Impulse Noise ( $\sigma^2=0.10$ )	0.0019	0.0022	0.0024	0.0020	0.0024
Speckle Noise ( $\sigma^2=0.05$ )	0.0018	0.0021	0.0025	0.0026	0.0024
Speckle Noise ( $\sigma^2=0.10$ )	0.0019	0.0024	0.0027	0.0027	0.0026
Rotation (5°)	0.0018	0.0021	0.0020	0.0022	0.0024
Rotation (10°)	0.0020	0.0023	0.0023	0.0024	0.0026
Scaling (200%)	0.0016	0.0017	0.0018	0.0019	0.0022
Scaling (400%)	0.0018	0.0019	0.0020	0.0020	0.0024
Blurring (5)	0.0024	0.0023	0.0020	0.0019	0.0023
Blurring (10)	0.0027	0.0026	0.0022	0.0021	0.0025
Cropping (10%)	0.0026	0.0028	0.0030	0.0029	0.0031
Cropping (25%)	0.0031	0.0034	0.0033	0.0031	0.0033

The stego images are added with Gaussian noise with a variance of 0.2 and 0.4, Poisson Noise, Impulse Noise with a variance of 0.05 and 0.1 and Speckle Noise with a variance of 0.05 and 0.1. Generally, addition of noise is responsible for the degradation of the image. The image processing operations such as Rotation (5 and 10 degrees), Scaling (200% and 400%), Blurring and Cropping (10% and 25%) are performed on embedded images.

After subjecting to the attacks, the original cover image is extracted and the bit error rate of extracted payload over secret payload is measured. Table 4 summarizes the experimental results for the proposed data hiding scheme against various attacks. As the BER is about 0.15 to 0.35 % of embedded payload, the algorithm is robust against various intentional and unintentional attacks.

### 6.3 Reversibility

In order to ensure the reversibility, the extracted cover image and the original cover image must be similar. The metric used to measure the similarity between the two images is Normalized Correlation Coefficient (NCC). The value of 0 represents no correlation. NCC will approach to one if the extracted cover image resembles the original cover image. The Normalized Correlation Coefficient between cover image and extracted cover image is defined as,

$$NCC = \frac{\sum_{x,y} (f(x,y) - f_{mean})(g(x,y) - g_{mean})}{\sqrt{\sum_{x,y} (f(x,y) - f_{mean})^2 \sum_{x,y} (g(x,y) - g_{mean})^2}} \tag{7}$$

where  $f(x, y)$  is the original cover image,  $g(x, y)$  is the extracted cover image.

Table 5 summarizes the experimental results for the proposed data hiding scheme against various attacks. As the NCC values are greater than 0.98, it is concluded that the algorithm restores the original cover image exactly at the destination.

### 7 Conclusion

In this paper, a reversible data hiding technique based on radon and integer lifting wavelet transform is presented. Hybrid transform has been proposed based on the unique features of the transforms, so that it is able to address the robustness and reversibility criteria. As the Radon transform performs rotation, scaling and translation operations on the cover image, it changes the positioning of the secret bits. The integer lifting wavelet transform guarantees complete reversibility. The original bits in the selected bit planes of LH, HL or HH subbands are compressed using arithmetic coding to provide space for embedding the payload bits. Generally, middle bit planes are used for embedding as they provide a balanced trade-off between embedding capacity and visual quality of that stego image. Data is embedded in red, green, and blue channels of the color image independently. As the PSNR obtained for the stego images is greater than 42 dB, the embedded payload is imperceptible to the human eye. The results have been compared with the existing works in the literature and the proposed method gives 10 to 15%

improvement in PSNR. As the BER is about 0.15 – 0.35 % of embedded payload, the algorithm is robust to attacks. From the simulation results, it is inferred that the proposed algorithm exhibits reversibility due to high NCC values.

### 8 References

1. Amsaveni, A. and Vanathi, P.T. (2015) 'A comprehensive study on image steganography and steganalysis techniques', *Int. J. Information and Communication Technology*, Vol. 7, Nos. 4/5, pp.406–424.
2. Amsaveni, A. and Vanathi, P.T. (2015) 'An efficient reversible data hiding approach for colour images based on Gaussian weighted prediction error expansion and genetic algorithm', *Int. J. Advanced Intelligence Paradigms*, Vol. 7, No. 2, pp.156–171.
3. Yang, B., Schmucker, M., Funk, W., Busch, C & Sun, S (2004), 'Integer DCT-based reversible watermarking for images using companding technique', *Proceedings of Electronic Imaging, Science and Technology*, vol. 5306, pp. 405-415.
4. Xuan, G., Zhu, J., Chen, J., Shi, Y.Q., Ni, Z., & Su, W (2002), 'Distortion less data hiding based on integer wavelet transform', *IEEE Electronics Letters*, vol. 38, no. 25, pp. 1646-1648.
5. Lin, S.D., Shie, S.C., & Guo, J.Y., (2010), 'Improving the robustness of DCT based image watermarking against JPEG compression', *International Journal of Computer Standards and Interfaces*, vol. 32, no. 1, pp. 54-60.

**Table 5:** Effect of various attacks on NCC

Attacks	Normalized Correlation Co-efficient				
	Airplane	Baboon	Boats	Lena	Pepper
Gaussian Noise ( $\sigma^2=0.2$ )	0.9817	0.9843	0.9825	0.9819	0.9824
Gaussian Noise ( $\sigma^2=0.4$ )	0.9850	0.9842	0.9860	0.9805	0.9814
Poisson Noise	0.9829	0.9844	0.9832	0.9822	0.9814
Impulse Noise ( $\sigma^2=0.05$ )	0.9839	0.9843	0.9816	0.9811	0.9813
Impulse Noise ( $\sigma^2=0.10$ )	0.9810	0.9816	0.9804	0.9802	0.9807
Speckle Noise ( $\sigma^2=0.05$ )	0.9833	0.9822	0.9871	0.9864	0.9846
Speckle Noise ( $\sigma^2=0.10$ )	0.9811	0.9804	0.9810	0.9820	0.9825
Rotation (5°)	0.9880	0.9806	0.9802	0.9824	0.9816
Rotation (10°)	0.9863	0.9794	0.9788	0.9804	0.9810
Scaling (200%)	0.9835	0.9820	0.9869	0.9846	0.9863
Scaling (400%)	0.9825	0.9806	0.9832	0.9828	0.9822
Blurring (5)	0.9854	0.9810	0.9809	0.9817	0.9826
Blurring (10)	0.9825	0.9806	0.9789	0.9738	0.9805
Cropping (10%)	0.9732	0.9726	0.9727	0.9728	0.9716
Cropping (25%)	0.9702	0.9706	0.9701	0.9706	0.9678

6. Xiang, S., Kim, H.J., & Huang, J (2008), 'Invariant Image watermarking based on statistical features in the low frequency domain', IEEE Transactions on Image Processing, vol. 14, no. 12, pp. 2140-2150.
7. Xuan, G., Zhu, J., Chen, J., Shi, Y.Q., Ni, Z., & Su, W., (2002), 'Distortion less data hiding based on integer wavelet transform', IEEE Electronics Letters., vol. 38, no. 25, pp. 1646-1648.
8. Stankovic, S, Djurovic, I & Pitas, I 2001, 'Watermarking In The Space/Spatial-Frequency Domain Using Two-Dimensional Radon-Wigner Distribution', IEEE Transactions on Image Processing, vol. 10, no. 4, pp. 650-658.
9. Lin, C, Wu, M, Bloom, J, Cox, I, Miller, M & Lui, Y 2001, 'Rotation, scale, and translation resilient watermarking for images', IEEE Transactions on Image Processing, vol. 10, no. 5, pp. 767-782.
10. Kim, H, Baek, Y, Lee, H & Suh, Y 2003, 'Robust image watermark using Radon transform and bispectrum invariants', Lecture Notes in Computer Science, pp. 145-159.
11. Lee, S, Yoo, CD & Kalker, T 2007, 'Reversible image watermarking based on integer-to-integer wavelet transform', IEEE Transactions on Information Forensics and Security, vol. 2, no. 3, pp. 321-330.
12. Calderbank, AR, Daubechies, I, Sweldens, W & Yeo, B 1998, 'Wavelet transforms that map integers to integers', Applied and Computational Harmonic Analysis, vol. 5, no. 3, pp. 332-369.
13. Xuan, G, Zhu, J, Chen, J, Shi, YQ, Ni, Z & Su, W 2002, 'Distortion less data hiding based on integer wavelet transform', IEEE Electronics Letters., vol. 38, no. 25, pp. 1646-1648.
14. Tsai, HH & Sun, DW 2007, 'Color image watermark extraction based on support vector machines' Journal of Information Sciences, vol. 177, no. 2, pp. 550-569.
15. Fu, YG & Shen, RM 2008, 'Color image watermarking scheme based on linear discriminant analysis. Computer Standard & Interfaces', vol. 30, no. 3, pp. 115-120.
16. Niu, PP, Wang, XY, Yang, YP & Ming, Y 2011, 'A novel color image watermarking scheme in non-sampled contourlet-domain', Journal of Expert Systems with Applications, vol. 38, no. 3, pp. 2081-2098 .

Arrived: 31. 03. 2017

Accepted: 12. 06. 2017





# Synthesis of Silicon Carbide Nanowhiskers by Microwave Heating: Effect of Heating Temperature

Suhaimi Mat Kahar<sup>1</sup>, Voon Chun Hong<sup>1</sup>, Lee Chang Chuan<sup>2</sup>, Subash C B Gopinath<sup>1,3</sup>, Mohd Khairuddin Md Arshad<sup>1</sup>, Lim Bee Ying<sup>4</sup>, Foo Kai Loong<sup>1</sup>, Uda Hashim<sup>1</sup>, Yarub Al-Douri<sup>5</sup>

<sup>1</sup>Institute of Nanoelectronic Engineering, Universiti Malaysia Perlis, Perlis, Malaysia

<sup>2</sup>School of Manufacturing Engineering, Universiti Malaysia Perlis, Perlis, Malaysia

<sup>3</sup>School of Bioprocess Engineering, Universiti Malaysia Perlis, Perlis, Malaysia

<sup>4</sup>School of Materials Engineering, Universiti Malaysia Perlis, Perlis, Malaysia.

<sup>5</sup>Physics Department, Faculty of Sciences, University Sidi-Bel-Abbes, 22000, Algeria.

**Abstract:** Silicon carbide (SiC) is an attractive material for its excellent properties such as wide band gap, high chemical stability and thermal conductivity. The conventional method for the preparation of SiC is Acheson process, a time and energy consuming process. In this article, demonstration of SiC nanowhiskers synthesis has been done by using microwave heating. Silica and graphite in the ratio 1:3 were mixed in ultrasonic bath, dried on hot plate and cold pressed uniaxially into a pellet die. The pellets were heated by using laboratory microwaves furnace at 1350°C, 1400°C and 1450°C with heating rate of 20°C/min and soaked for 40 minutes. Different characterizations and testing were done to study the effect of heating temperature on the synthesis of SiC nanowhiskers. 1400°C is proved to be the most suitable temperature for the synthesis of SiC nanowhiskers.  $\beta$ -SiC appeared as the only phase in the x-ray diffraction pattern of SiC nanowhiskers formed at 1400°C with no traces of raw materials. Field emission scanning electron microscopy confirmed the presence of only a negligible amount of graphite or silica in SiC nanowhiskers synthesized at 1400°C. Furthermore, energy dispersive x-ray spectroscopy analysis revealed that only elemental C and Si were present in SiC nanowhiskers synthesized at 1400°C. Meanwhile, photoluminescence spectrum indicated the presence of single  $\beta$ -SiC peak at 440 nm which is associated with band gap of 2.8 eV. Single absorption bands of Si-C bond were detected at 803.5  $\text{cm}^{-1}$  in fourier transform infrared spectrum. SiCNWs produced in this study at 1400°C has good thermal stability with 6% of weight loss, indicates its potentiality for high temperature electronics.

**Keywords:** Microwave heating; Silicon carbide nanowhiskers; Synthesis; Graphite; Silica

## Sinteza nanodlačic iz silicijevega karbida z mikrovalovnim segrevanjem: Vpliv temperature gretja

**Izveček:** Silicijev karbid (SiC) je zelo zanimiv material zaradi svojih odličnih lastnosti, kot je široka energijska reža, kemijska stabilnost in termična prevodnost. Konvencionalen je SiC pridobiva z Acheson-ovim procesom, ki p a je energijsko in časovno izredno potraten. V članku predstavljamo sintezo nanodlačic SiC s pomočjo gretja z mikrovalovi. V ultrasonični kopeli je bil pripravljena mešanica silicija in grafita v razmerju 1:3, nato posušena na vroči plošči in hladno stisnjena matrico peleta. Peleti so bili nato segrevani z laboratorijsko mikrovalovno pečico pri 1350 °C, 1400 °C in 1450 °C s hitrostjo gretja 20 °C/min in trajanjem 40 min. Opravljene so bile različne karakterizacije nanodlačic. Izkazalo se je, da je temperature 1400 °C najprimernejša za izdelavo nanodlačic. V vzorcu sipanja x žarkov se izkazalo, da nanodlačice vsebujejo le  $\beta$ -SiC brez ostankov surovega materiala. Elektronska mikroskopija je potrdila prisotnost le zanemarljivega dela silicija in grafita. Fotoluminiscenca je nakazala le eden vrh signala pri 440 nm kar je v skladu z energijsko režo 2.8 eV. Absorpcijski pas je bil zaznan pri 803.5  $\text{cm}^{-1}$  v fourierjevi transformaciji infrardečega spektra. Izdelane nanodlačice so pokazale dobro termično stabilnost z 6 % izgubo teže, kar pomeni, da predstavljajo zanimiv material za visokotemperaturno elektroniko.

**Ključne besede:** mikrovalovno gretje; nanodlačice iz silicijevega karbida; sinteza; grafit; silicij

\* Corresponding Author's e-mail: chvoon@unimap.edu.my

## 1 Introduction

Silicon carbide (SiC) is a very attractive semiconductor due to its excellent properties such as high hardness, good flexibility, high thermal conductivity, high thermal stability, excellent chemical stability and large band gap. Because of these attractive properties, it possesses great potential for industrial and engineering applications such as abrasives [1, 2], high power electronics [3, 4], harsh environment electronics and composite reinforcements [5, 6]. SiC nanomaterials such as SiC nanocrystals and nanowhiskers have many potential electronic applications. For example, SiC nanocrystals (NCs) exhibit photoluminescence in the near-UV to the visible blue spectral region and making them attractive candidates for the fabrication of light-emitting devices [7]. Moreover, several field emission measurements on the SiCNWs suggested that SiCNWs are potential candidates for the cold cathode field emission device (FED) because of their unique electrical, chemical, and mechanical properties [1]. SiC has been produced by several methods, however, most SiC are produced now-a-days using the Acheson process [2]. This process produces SiC by heating mixture of quartz sand and powdered coke (carbon-based material) in an iron bowl using voltages 50,000 V for 20 hours at temperatures around 2200–2400°C. The drawbacks of this industrial production process include high energy consumption and the product has low purity. Moreover, this process is time consuming; therefore several alternative methods have been previously reported for SiC synthesis. Most commonly used methods for SiC synthesis are carbon thermal reduction [9], physical evaporation, sol-gel process [10, 11] and chemical vapor deposition [12]. However, there are still some drawbacks that limit the wide applications of these methods, such as high energy consumption, long processing time and extensive chemical usage, although these processes can successfully synthesize SiC.

Recently, researchers have applied microwave heating for the synthesis of inorganic materials [13-16]. From mid-1980s until 2007, hundreds of papers have been published regarding the applications of microwaves in chemical synthesis [16-21]. Development of new routes for the synthesis of inorganic material is an integral aspect of materials chemistry. The development of alternative synthesis methods is a continuing need for fast and energy-efficient techniques. Microwaves are electromagnetic radiation, whose wavelengths lie in the range of 1 mm to 1 m [16]. Microwave synthesis has emerged in recent years as a new method to synthesize a variety of materials that has shown significant advantages against conventional synthesis procedures. Microwaves can volumetrically heat materials and give sudden increase in the temperature

of the material comparing to conventional heating processes that rely on external radiant energy to heat materials by mode of conduction, convection and radiation. Microwave heating is a process in which the materials couple with microwave, absorb the electromagnetic energy volumetrically, and transform into heat [15]. The carbonaceous materials are among the most sensitive to microwaves irradiation [23]. This is due to the fact that carbon based materials generate heat from the motion of electron through joule heating within the grain of carbon when exposed to microwave irradiation, although carbon based materials have no freely-rotatable dipoles [23]. Materials scientists have identified several advantages of microwave processing of ceramics such as economical, rapid heating, large scale production and reduced cracking and thermal stress [14]. Other than that, Mingos et al. [12] proposed that synthesis of inorganic material using microwave heating can enhance the mechanical properties of the material since the sintering time is generally shortened and thus reduced the possibility of secondary crystallization.

Silicon carbide nanowhisker (SiCNW) is a silicon carbide 1-D nanostructure in whisker/needle form. One-dimensional silicon carbide (1D SiC) nanomaterials have shown unusual properties such as extremely high strength, good flexibility and fracture toughness, lead to many potential applications such as sensors, field emitting diodes and solar cells [1, 24]. 1-D nanostructure is also expected to play an important role as both interconnect and as functional units in fabrication of electronics, optoelectronics, electrochemical and electromechanical devices at nanoscale dimensions [1, 25, 26]. In particular,  $\beta$ -SiC nanowhiskers, with an energy band gap of 2.39 eV and relatively high electron mobility would be a suitable material for applications in nanoelectronic devices.

In this study, microwave heating was used to synthesize SiCNWs from the mixture of graphite and silica since it is generally faster, cleaner, and more economical than the conventional methods. The effect of heating temperature was studied to determine the most suitable temperature for the synthesis of SiCNWs from silica and graphite. Previously, several researches have studied the effect of heating temperature on the synthesis of silicon carbide from silica and carbon-based starting materials. For examples, Wang et al. [27] studied the synthesis of SiC whiskers on graphitic layers using expanded graphite (EG) by silicon vapor deposition without catalyst at temperature ranged from 1000 to 1400°C. Wang et al. [27] found that the amount of  $\beta$ -SiC on graphite increases with the temperature and the largest amount of  $\beta$ -SiC formed at 1400°C. Other than that, Jin Li et al. [28] have synthesized nanostructured

SiC particles and whiskers from rice husk by microwave heating at temperature ranged from 1100°C to 1500°C. They found that 1500 °C is the most ideal temperature for the synthesis of  $\beta$ -SiC. Therefore, heating temperature is believed to have significant effect on the quality and purity of the end products during the synthesis of SiCNWs. To the best of our knowledge, no study on the effect of heating temperature on the microwave synthesis of SiCNWs from graphite and silica was reported. Thus, in this study, the effect of heating temperature on the morphology, composition, optical properties and purity was studied and presented.

## 2 Material and Methods

### 2.1 Sample preparation

Silica (particle size  $\leq 50 \mu\text{m}$ ) and extra pure fine graphite powder (particle size  $\leq 50 \mu\text{m}$ ) were used as starting material. Mixture of silica and graphite in molar ratio of 1:3 with total of 1 gram was acquired. Ethanol was used as liquid medium to mix the raw material. Ultrasonic mixing bath was used as the external mean to generate vibration in the ethanol for the homogeneous mixing of the raw materials. The mixtures were then dried using hot plate to vaporize the ethanol. Before subjecting to microwave heating, the mixture was compressed to become pellet. The process of making pellet is essential to separate the mixture of  $\text{SiO}_2$  and graphite from the graphite powder placed around the pellet inside the crucible. The pressure that applied to the mixture during the compression process was 312.4 MPa to ensure mixtures were fully compressed.

### 2.2 Synthesis of SiCNWs by microwave heating

Microwave heating was performed in Synotherm microwave sintering furnace (MW-L0316V) with multi-

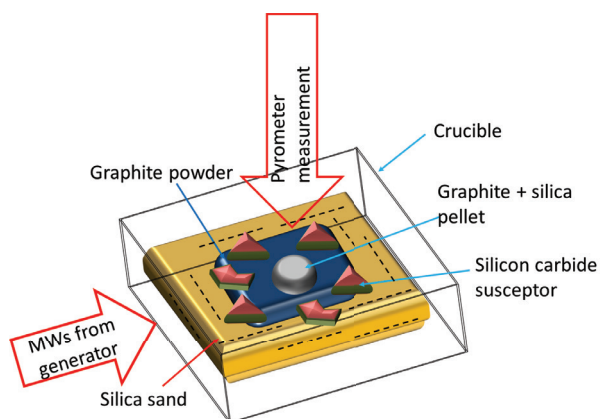


**Figure 1:** Setup for sample preparation inside the microwave cavity.

mode cavity in which 2.45 GHz microwave radiation was brought out through a waveguide.

The pellet was placed in silica crucible and it was placed in microwave cavity as shown in Fig. 1. Silica sand was used as heat insulator to prevent heat loss. SiC susceptor functioned as microwave absorber to absorb and convert electromagnetic energy to heat because SiC susceptor is a good microwave absorbing material. The pellets were heated to different temperatures of 1350°C, 1400°C and 1450°C with heating rate of 20°C/min and soaked for 40 minutes. The synthesis was performed under argon atmosphere.

### 2.3 Characterization of SiC nanowhiskers

After the microwave heating was conducted, samples were characterized by using x-ray diffraction (XRD), field emission scanning electron microscopy (FESEM), energy-dispersive x-ray spectroscopy (EDX), photoluminescence spectroscopy (PL), fourier transform infrared spectroscopy (FTIR) and thermo-gravimetric analysis (TGA).

The morphologies of samples were observed by using FESEM model Nova Nano 450 at magnification 200K and accelerating voltage of 5 kV while EDX (EDX OXFORD FM29142) was used to determine the elemental composition of the specimens. The samples in the powder form were added into ethanol and ultrasonicated for homogeneous dispersion. The dispersions were then dropped on the substrate and the substrate was heated by using hot plate to evaporate the ethanol. The samples on the substrate were then subjected to characterization using FESEM and EDX. The built in software for OXFORD FM29142 enables automatic correction and robust spectrum processing that works in non-flat sample measurement with no need for any background fitting adjustment. Meanwhile, XRD Siemens Diffractometer Model D-5000 using Cu K $\alpha$  radiation source in  $\theta/2\theta$  mode was used to investigate the composition of specimens. Measurements were made with fast duration scan (1s) and small step size (0.02°). Optical properties of SiCNWs synthesized from the mixtures were identified by using the photoluminescence spectroscopy (PL FL3-11 J81040) with xenon lamp at 400 watt and excitation wavelength at 360 nm and recorded from wavelength of 300 nm to 650 nm while FTIR (FTIR MAGNA550 kBr) was used to scan the samples from 500 to 4000  $\text{cm}^{-1}$  with spectrum resolution of 4  $\text{cm}^{-1}$ . Purity of SiCNWs was evaluated indirectly by using Perkin-Elmer Pyris 6 TGA analyzer. Samples about 10 mg were heated from 30 to 1300°C with the heating rate of 10 °C/min in atmospheric air to investigate the purity of the as synthesized SiCNWs.



### 3 Result and Discussions

#### 3.1 Characterization of SiCNWs using FESEM

Fig. 2 shows the FESEM images of SiO<sub>2</sub> and graphite subjected to microwaves heating at different temperatures. It can be seen that the heating temperature of SiO<sub>2</sub> and graphite significantly influenced the synthesis of SiCNWs. Fig. 2 (a) shows the mixture SiO<sub>2</sub> and graphite after subjected to microwaves heating at 1350°C. It can be observed that only a small amount of nanowhiskers were formed around particles that is believed to be unreacted SiO<sub>2</sub> and graphite. Besides, the nanowhiskers that formed from the reaction between silica

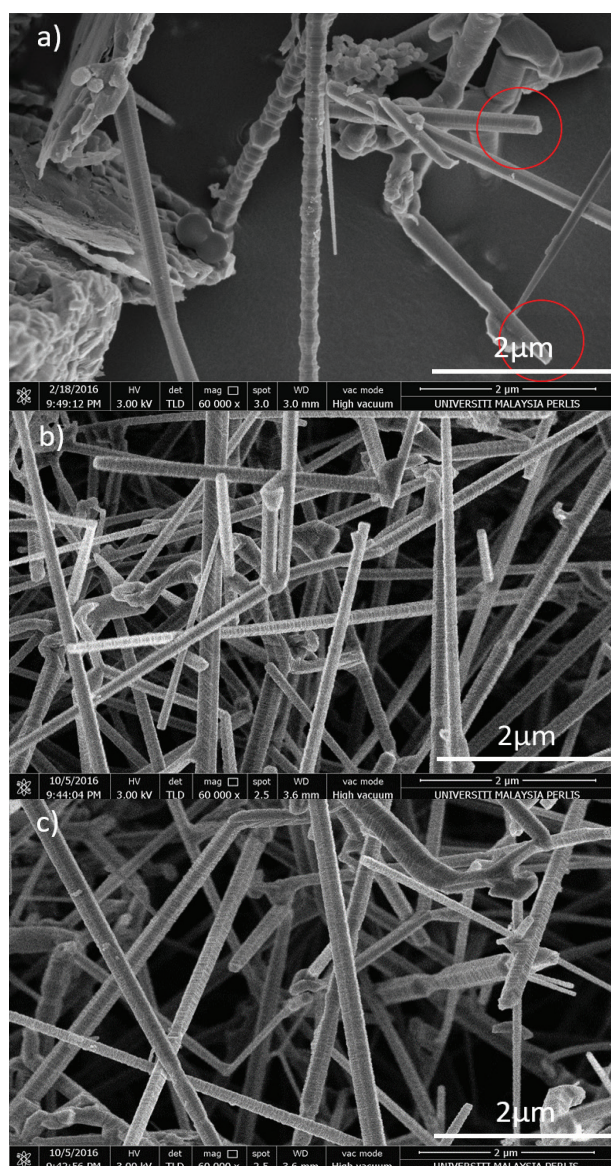


**Figure 2:** FESEM images of SiCNWs synthesized by microwave heating of mixture of SiO<sub>2</sub> and graphite at heating temperatures of a) 1350°C b) 1400°C and c) 1450°C.

and graphite were not fully grown as indicated by red circles in Fig. 2 (a). It is believed that this might be due to the fact that heating temperature at 1350°C was not sufficiently high to enable the full reaction between graphite and SiO<sub>2</sub> for the complete formation of SiC nanowhisker. Similar observation was reported by Wang et.al that hybridized silicon carbide (SiC) whiskers on graphitic layers in expanded graphite (EG) by silicon vapor deposition without catalyst. They reported that for the synthesis conducted at low heating temperature (1100°C to 1300°C), small amount of SiC was produced due to incomplete reactions [27].

Fig. 2 (b) shows the FESEM image of SiCNWs formed from the mixture of SiO<sub>2</sub> and graphite that was subjected to microwaves heating at 1400°C. SiC in the form of nanowhiskers can be observed clearly. The diameters of SiCNWs are uniform along the length of the nanowhiskers. Only small amount particles of graphite or silica were observed, such that almost all graphite and silica were converted to SiCNWs. Wang et.al [27] have also reported similar result in which large amount of SiC in the form of nanowhiskers were formed at 1400°C. The diameters of the nanowhisker were measured by using ImageJ version 1.48 and they were ranged between 70 nm and 100 nm.

Fig. 2 (c) shows the SiC whiskers formed by microwaves heating mixture of SiO<sub>2</sub> and graphite at 1450°C. It can be observed that the amount SiC whiskers are similar comparing to those formed at 1400°C in Fig. 2 (b). Large amount of SiCNWs can be observed. The diameter of the SiCNWs formed were measured and are ranged from 70 nm to 120 nm which are similar to SiCNWs in Fig. 2 (b). The diameter for the SiCNWs formed at 1450 °C are slightly larger and this might due to the increase of heating temperature. Similar result were also obtained by Wang et al [27]. They reported that the diameter of β-SiC nanowhiskers in the specimen treated at 1400 °C were larger than those treated below 1400 °C [27]. With the increasing heating temperature, the rate of reaction of SiC was increased. This caused higher SiC formation rate on the intially formed SiCNWs during the heating process, and led to larger diameter of SiCNWs at higher temperature.

#### 3.2 Characterization of SiCNWs using XRD

XRD patterns of SiCNWs synthesized from mixture of SiO<sub>2</sub> and graphite at different temperatures are shown in Fig. 3. For SiCNWs synthesized at 1350°C as shown in Fig. 3 (a), small peaks corresponding to SiO<sub>2</sub> at 2θ of 22.3° associated with plane (100) of SiO<sub>2</sub> (JCPDS card 01-089-3434) was observed. A peak of carbon phase was also observed at 27° corresponding to plane (002) of graphite (JCPDS card 03-065-6212).

Generally, the presence of carbon and  $\text{SiO}_2$  is due to the presence of unreacted graphite and silica. Peaks of  $\beta$ -SiC (111) and (220) were also observed at  $2\theta$  of  $36^\circ$  and  $61^\circ$ . This indicated that reaction of  $\text{SiO}_2$  and graphite to form SiCNWs at  $1350^\circ\text{C}$  was incomplete. This observation is in good agreement with the corresponding FESEM image in Fig. 2 (a) where only small amount of SiCNWs along with graphite and silica were observed.

Fig. 3 (b) shows the XRD pattern of SiCNWs synthesized from mixture of  $\text{SiO}_2$  and graphite at  $1400^\circ\text{C}$ . Three peaks that were corresponded to (111), (220) and (311) crystal planes of cubic  $\beta$ -SiC (JCPDS card 074-2307) were observed at  $2\theta$  of  $36^\circ$ ,  $61^\circ$  and  $72.5^\circ$ . Bin li et.al. [10] also reported similar result in which diffraction peaks of  $\beta$ -SiC at  $2\theta$  of  $35.8^\circ$ ,  $60^\circ$  and  $71.8^\circ$  corresponding to (111), (220) and (311) cubic reflections were obtained. No signal of either  $\text{SiO}_2$  or carbon was detected in this XRD pattern. It can be concluded that mixture of  $\text{SiO}_2$  and graphite were converted completely to SiCNWs when  $1400^\circ\text{C}$  was used such that the amounts of the raw materials were too small to be detected by XRD. This result is in good agreement with the FESEM images in Fig. 2 (b) in which only SiCNWs were observed.

For SiCNWs synthesized from mixture of  $\text{SiO}_2$  and graphite at  $1450^\circ\text{C}$ , as in Fig. 3 (c), peaks corresponded to  $\beta$ -SiC as major phase appeared at  $2\theta$  values of  $36^\circ$ ,  $61^\circ$  and  $72.5^\circ$ , respectively. The relative intensities of these peaks were similar compared to Fig. 3 (b). In good agreement with FESEM image of Fig 2 (c), SiCNWs were observed with only small amount of graphite or silica particles.

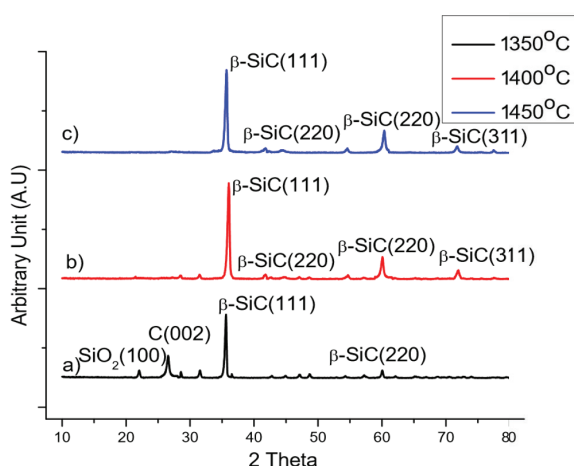


**Figure 3:** XRD patterns of SiCNW synthesized by microwave heating of mixture of  $\text{SiO}_2$  and graphite at heating temperatures of a)  $1350^\circ\text{C}$ , b)  $1400^\circ\text{C}$  and c)  $1450^\circ\text{C}$ .

### 3.3 Characterization of SiCNWs using EDX

Fig. 4 shows the EDX spectra of the SiCNWs synthesized by microwave heating at  $1350^\circ\text{C}$ ,  $1400^\circ\text{C}$  and  $1450^\circ\text{C}$ . Qualitative analysis was conducted to identify the elements that are present in the as synthesized SiCNWs. EDX spectra with high accuracy after subjecting to automatic correction and robust spectrum processing using the built in software were obtained. Fig. 4 (a) shows the EDX peak of SiCNWs that synthesized from mixture of silica and graphite at  $1350^\circ\text{C}$ . From the peak, 3 elements were detected which are Si, C and O. O element is corresponded to the presence of silica in the end product. This indicated that silica was not fully reacted in this process, and this is in good agreement with XRD result in Fig. 3 and FESEM images in Fig. 2 (a). Similar observation was reported by Quah et al. [29] and they attributed the presence of O element in the EDX spectrum to the presence of unreacted  $\text{SiO}_2$  in final product.

For EDX spectra of SiCNWs synthesized at  $1400^\circ\text{C}$  and  $1450^\circ\text{C}$ , peaks corresponded to Si and C elements were observed. This indicated that mixture of  $\text{SiO}_2$  and graphite reacted completely to form SiCNWs at  $1400^\circ\text{C}$  and  $1450^\circ\text{C}$ .

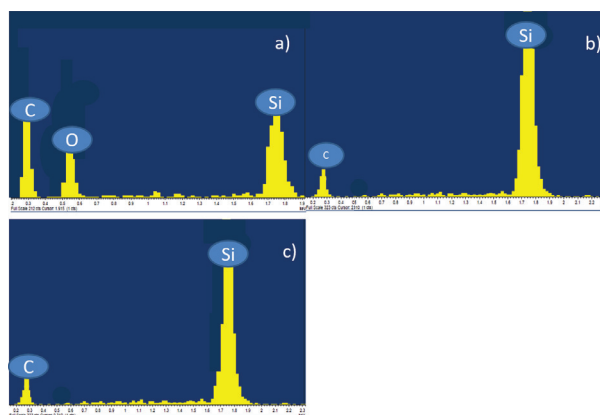


**Figure 4:** EDX spectra of SiCNWs synthesized by microwave heating of mixture of  $\text{SiO}_2$  and graphite at heating temperatures of a)  $1350^\circ\text{C}$ , b)  $1400^\circ\text{C}$  and c)  $1450^\circ\text{C}$ .

### 3.4 Characterization of SiCNWs using FTIR

FTIR transmission spectra of SiCNWs synthesized from mixture of graphite and  $\text{SiO}_2$  at different heating temperatures are shown in Fig. 5. From the spectra, it can be concluded that SiCNWs were successfully synthesized at all temperatures since FTIR peaks corresponded to Si-C stretching bond were present at around  $800\text{ cm}^{-1}$  in all FTIR spectra of SiCNWs. However, as in Fig. 5 a), it can be observed that SiCNWs at heating temperature of  $1350^\circ\text{C}$  has absorption band of relatively low intensity at  $801.7\text{ cm}^{-1}$  that indicates only small amount of SiCNWs were formed. FTIR peak corresponded to

stretching bond of Si-O bonding group was also observed at  $1097.28\text{ cm}^{-1}$ . The presence of this absorption band indicated the presence of unreacted  $\text{SiO}_2$ . Similar absorption bands were reported by Zhao et al. [30] and Rajarao et al. [31]. Zhao et al. [30] obtained such absorption peak at  $1080\text{ cm}^{-1}$  and they suggested that this peak was associated with the Si-O-Si bond of mesoporous silica. Rajarao et al. [31] also reported absorption band at  $1045\text{ cm}^{-1}$  and this peak was attributed to Si-O-Si bond. Absorption bands at  $1640.2\text{ cm}^{-1}$  were also observed in Fig. 5 (a) due to the presence of C=C bonds of graphite [32]. The presence of absorption bands of both  $\text{SiO}_2$  and graphite indicate that  $1350^\circ\text{C}$  was insufficient to enable complete reaction between  $\text{SiO}_2$  and graphite and thus some of the  $\text{SiO}_2$  and graphite were left unreacted.

For FTIR spectrum of SiCNWs formed at  $1400^\circ\text{C}$ , only one peak was observed at  $803.5\text{ cm}^{-1}$  corresponding to the presence of Si-C bond that indicated the successful synthesis of SiCNWs. This result is in good agreement with the XRD pattern of SiCNWs synthesized at  $1400^\circ\text{C}$  in Fig. 3 (b) which indicates the presence of single phase  $\beta$ -SiC and thus denotes complete conversion of graphite to SiCNWs. FTIR spectrum of SiCNWs synthesized at  $1450^\circ\text{C}$  as shown in Fig. 5 (c) also revealed the presence of single phase  $\beta$ -SiC due to the presence of absorption peak of Si-C stretching bonds centered at  $804.6\text{ cm}^{-1}$ .

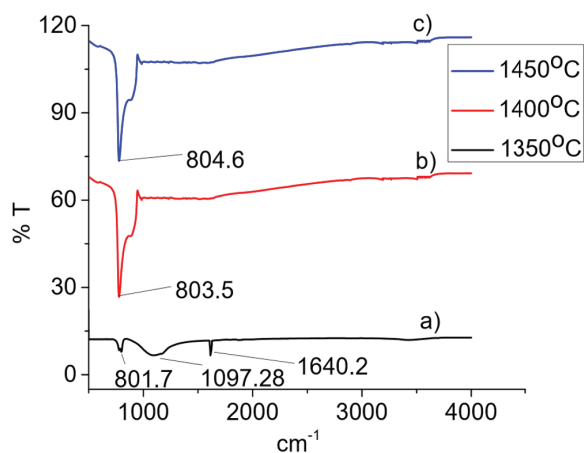


**Figure 5:** FTIR spectra of SiCNWs synthesized by microwave heating of mixture of  $\text{SiO}_2$  and graphite at heating temperatures of a)  $1350^\circ\text{C}$ , b)  $1400^\circ\text{C}$  and c)  $1450^\circ\text{C}$ .

### 3.5 Characterization of SiCNWs using PL

PL spectra of SiCNWs synthesized at different heating temperatures were showed in Fig. 6. Fig. 6 shows peaks of SiCNWs at  $440\text{ nm}$  ( $2.8\text{ eV}$ ) in all spectra. The peaks are obviously blue-shifted in comparison with the band gap of 3C-SiC ( $2.39\text{ eV}$ ). The blue shift of the PL

peak of 3C-SiC nanomaterials has been reported by several researchers [33,34,35]. For example, the peak at  $418\text{ nm}$  for 3C-SiC nanobelts has been reported by Wu et al [36]. They proposed that the location of this peak depends on the nanostructure, morphology and size of 3C-SiC materials. The collective influence of size confinement effect and defects lead to the blue shift of the peak. Thus, the peak emission appeared around  $440\text{ nm}$  may be due to size confinement effect and defects.

In Fig. 6 (a), PL spectrum of SiCNWs synthesized from blend of  $\text{SiO}_2$  and graphite at  $1350^\circ\text{C}$  shows the presence of PL peak attributed to oxygen discrepancy in  $\text{SiO}_2$  and carbon at wavelength about  $380$  and  $620\text{ nm}$  which corresponded to band gap of  $3.2\text{ eV}$  and  $2.0\text{ eV}$ , respectively. This PL spectrum result is in good agreement with the XRD result of SiCNWs synthesized at  $1350^\circ\text{C}$  which shows the presence of XRD peak corresponded to  $\text{SiO}_2$  and carbon. Nandanwar et al [37] reported the characterization of  $\text{SiO}_2$  nanoparticles and also reported PL peak of pure  $\text{SiO}_2$  at  $381.8\text{ nm}$ .

Fig. 6 (b) and (c) shows that in the PL spectra of SiCNWs synthesized at  $1400^\circ\text{C}$  and  $1450^\circ\text{C}$ , only one peak appeared at  $425\text{ nm}$  and this peak is corresponded to  $\beta$ -SiC. This indicated that only SiC is present in the SiCNWs synthesized at heating temperature  $1400^\circ\text{C}$  and  $1450^\circ\text{C}$ . This result is in good consistent with the XRD result in Fig. 3 (b) and (c) that graphite and  $\text{SiO}_2$  react completely to form single phase SiCNWs.

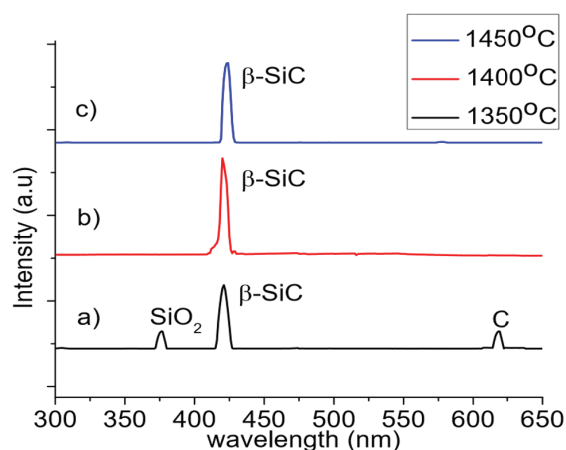


**Figure 6:** PL spectrum of SiCNWs synthesized by microwave heating of mixture of  $\text{SiO}_2$  and graphite at heating temperatures of a)  $1350^\circ\text{C}$ , b)  $1400^\circ\text{C}$  and c)  $1450^\circ\text{C}$ .

### 3.6 Thermal Gravimetric Analysis of SiCNWs

Thermal Gravimetric Analysis (TGA) curves of SiCNWs synthesized at different heating temperatures are presented in Fig. 7. TGA was conducted to evaluate indirectly the quantity of SiCNWs. For SiCNWs synthesized



at 1450°C in Fig. 7 (b), the weight loss started at 700°C with a total of 7 wt %. Similar weight loss occurred for SiCNWs synthesized at 1400°C with 6 wt% as shown in Fig. 7 (a). These small weight losses of SiCNWs can be attributed to the oxidation of small amount of unreacted carbon and loss of moisture. The presence of moisture may happen during the handling of sample since sample is powder which can easily absorb moisture. Corriu et al. [38] proposed that the weight loss which occurred at 450 °C to 750 °C domain was attributed to the air oxidation of the carbon. This indicated graphite was almost fully converted to SiCNWs with only very small amount of unreacted carbon for both SiCNWs synthesized at 1400 °C and 1450 °C. This result is in good agreement with XRD result in Fig. 3 a) and b) in which carbon and silica were too little to be detected. This high resistance toward oxidation for SiCNWs synthesized at 1400°C and 1450 °C is attributed to the formation of pure SiCNWs. TGA curves show no weight loss at temperature higher than 800 °C for both SiCNWs formed at 1400 and 1450 °C, indicating the remaining residue were SiCNWs.

Fig. 7 c) shows that for SiCNWs synthesized at 1350°C, a total of 45% of weight loss is observed starting at 700 to 950 °C and this weight loss was attributed to the oxidation of unreacted carbon in SiCNWs. These results are in good agreement with the XRD result displayed in Fig. 3 which showed the presence of peak of unreacted carbon in SiCNWs synthesized at 1350°C. This result demonstrated that SiCNWs produced at 1400°C and above has relatively high purity and good thermal stability.

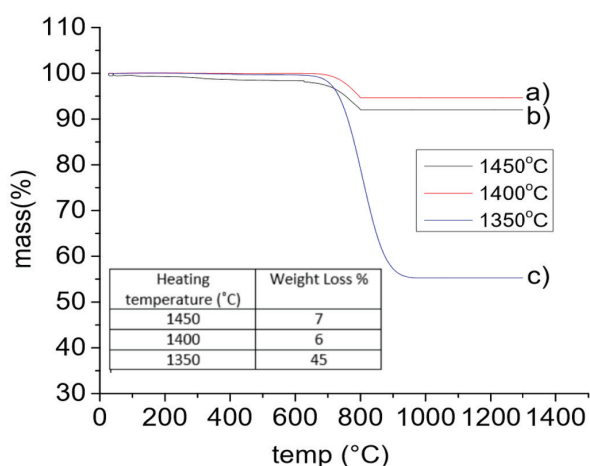


**Figure 7:** TGA curves of SiCNWs synthesized by microwave heating of mixture of SiO<sub>2</sub> and graphite at heating temperatures of a) 1400°C, b) 1450°C and c) 1350°C.

### 3.7 Mechanism of Synthesis of SiCNWs by Microwaves Heating

For this research, the interactions between carbon-based material (graphite) and microwave irradiation are important to generate heat thus give many advantages in many aspects to synthesize SiCNWs. Since the quartz materials are not sensitive to microwave, in this study we proposed that the heat from graphite (carbon based material) are transferred to silica via external means such as conduction, convection and radiation to assist the heating of silica. Lin He et al. [22] proposed that silica is an inorganic material that almost cannot react to microwave and the reaction are not as effective as carbon based material from the calorimetric study based on these materials. The homogeneous mixture between silica and graphite therefore significantly affects the uniformity of temperature increase for both materials. For this reason, ultrasonic mixing of graphite and silica using ethanol as medium provided homogeneous mixing.

The mechanism of microwave heating varies according to the interaction between the microwaves and target materials. Dielectric heating occurs when dielectric materials such as graphite interact with microwaves. Electric field component of electromagnetic interact with charged particles (electrons) of carbon causes the material to generate heat. Graphite is known as carbon-based material that contains charged particles which are free to move in a delimited region of the material [23, 39]. When electromagnetic field is subjected to the material such as graphite, current traveling in phase with the electromagnetic field is induced. The electron from the carbon material cannot couple to the changes of phase in the electric field and causes energy to dissipate in the form of heat. Fig. 8 shows the mechanism of dielectric heating that based on motion of electrons from carbon material to generate heat. Motion of electron from carbon through joule heating within the grain generates heat. This reaction is called Maxwell-Wagner effect and it is significantly different from the reaction between electromagnetic wave and

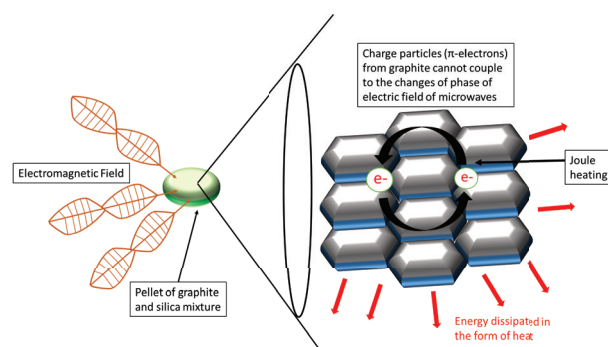
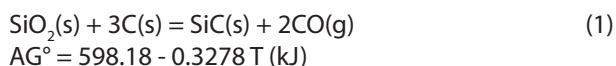


**Figure 8:** Interaction of microwave with graphite leads to dielectric heating of graphite.

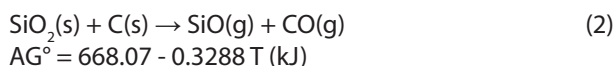


polar liquid such as water that heat up due to vibration of molecules [40,23].

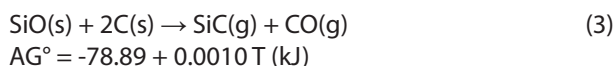
The overall reaction of formation for SiC through carbo-thermal reduction is generally written as [41]:



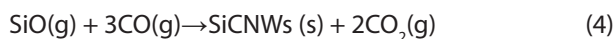
There are multiple reactions between silica and graphite before the formation of SiCNWs. First reaction is the solid-solid reaction between silica and graphite causing the carbothermal reduction of silica by graphite to form SiO and CO gases by following reaction [41]:



The vapour-solid (VS) mechanism was suggested to explain the formation of SiCNWs. From reaction (3), SiO gas reacts with C to produce SiC nuclei as follow [42]:



Cetinkaya et.al stated for VS mechanism, Si-containing vapors such as Si gas or SiO gas are believed to react with CO gas or C solid to form SiC nuclei [43]. Thus, SiC particles from reaction (3) are believed to serve as nucleation sites for VS mechanism to occur.



From reaction (4), the VS mechanism occurred when SiO vapour and CO vapour deposited at the tip of SiC nuclei that formed from reaction (3). Fig. 9 summarizes the overall reaction between graphite and silica for the formation of SiCNWs. The nanowhisker grows along the directions of the least stable plane and forms SiCNWs, as in Fig. 10. J. Wei et al. [44] and Dehghanzadeh [45] et al. have proposed that the nanowire growth might be attributed to the reaction between SiO and carbon gases. The effect of temperature for synthesis of SiCNWs

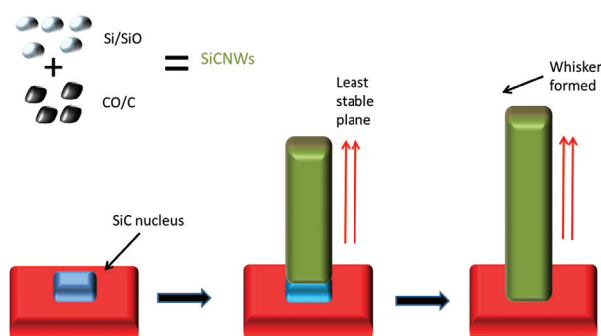


**Figure 9:** Schematic of SiCNWs growth from graphite and silica by microwaves heating.

has been studied by thermodynamic calculation. The Gibbs free energy for overall reaction in reaction (2) decreases with temperature thus denoted that the reaction is non-spontaneous reaction. Based on Gibbs free energy, reaction (2) is highly endothermic and the reaction is favorable to occur as the temperature increases [46]. Synthesis of SiC is basically dependent on the formation of SiO gas. Lee et al. also proposed that SiC is synthesized through the formation of intermediate SiO [47].

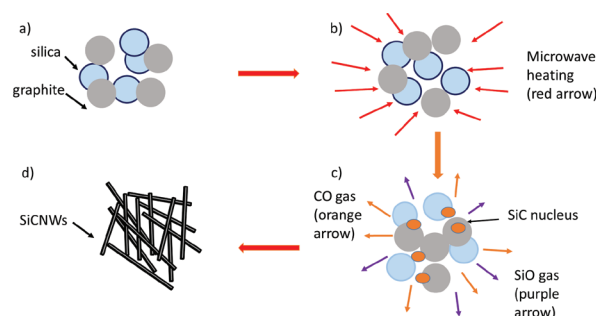


**Figure 10:** Schematic of SiCNWs growth from graphite and silica by microwaves heating a) Mixture of graphite and silica b) Exposing mixture of SiO<sub>2</sub> and graphite to microwave irradiation until 1400°C c) Formation of SiO gas, Co gas and SiC nucleus after exposed to microwave irradiation at high temperature d) Formation of SiCNW.

The Gibbs free energy for the reaction between SiO gas and carbon as in reaction (3) is negative and thus the reaction is spontaneous, regardless of the temperature. Thus, the overall SiC formation is defined by SiO formation in reaction (2), since the Gibbs free energy decreases significantly on temperature. Furthermore, formation of SiO gas is the rate determining step for the overall reaction of SiC formation [48, 49]. Some researchers have studied the rate of reaction to synthesis SiC based on Arrhenius equation [49, 50].

$$k = Ae^{-E_a/RT} \quad (5)$$

Rate constant and activation energy are calculated based on the Arrhenius equation in equation (5). Kavitha et al. [50] studied the synthesis of nano silicon carbide powder from agricultural waste and calculated the activation energy during the synthesis of SiC using the Arrhenius equation. They reported that with the increasing of heating temperature, the activation energy decreased and caused the rate of reaction for the synthesis of SiC to increase. This explained the significant effect of temperature on the rate of reaction of the synthesis of SiC. Furthermore, for temperature at 1350°C, it is believed that the partial pressure of SiO gases produced was lower than those produced at temperature above 1400 °C. Y. Li et al. [51] reported that the partial

pressure of SiO as predominant gas increased with temperature which was originated from the oxidation of silica. Thus, the amount of nucleation sites produced from reaction of SiO gas and carbon (solid) at 1350 °C was expected to be lower comparing to those formed at 1400 °C and 1450 °C. SiO and CO gases as the product from reaction at (3) and (4), respectively, react to form SiCNWs but the reaction was incomplete due to the lack of reactant (SiO) at low temperature. This explained the incomplete formation of SiCNWs at 1350 °C when the heating duration was set to 40 minutes. For temperature above 1400 °C, as shown by the results, heating duration of 40 minutes was sufficient for complete synthesis.

#### 4 Conclusions

SiC nanowhiskers have been successfully synthesized by microwaves heating of mixture of SiO<sub>2</sub> and graphite in the ratio of 1:3. The effect of heating temperature during microwave heating was studied. SiCNWs were characterized by using X-ray diffraction (XRD), field emission scanning electron microscopy (FESEM), energy dispersive x-ray spectroscopy (EDX), photoluminescence spectroscopy (PL), fourier transform infrared (FTIR) and thermo-gravimetric analysis (TGA). 1400 °C is the most suitable temperature for the synthesis of SiCNWs because of complete reaction between silicon dioxide and graphite resulted in the formation of single phase β-SiC nanowhiskers in nanoscales as proven by the results obtained from characterization and testing. By using 1350 °C for the synthesis of SiCNWs, traces of unreacted graphite and SiO<sub>2</sub> were detected that indicated incomplete conversions of graphite and silica to SiCNWs while synthesis of SiCNWs at 1450 °C resulted in SiCNWs with diameter higher than 100 nm.

#### 5 Acknowledgments

The authors are grateful to the Department of Higher Education, Ministry of Higher Education, Malaysia for funding this research through the Fundamental Research Grant Scheme (FRGS) with the grant number [9003-00441]. The author also would like to acknowledge all the team members in Institute of Nano Electronic Engineering (INEE), Universiti Malaysia Perlis (UniMAP) for their guidance and help.

#### 6 References

1. Prakash, J., Venugopalan, R., Tripathi, B. M., Ghosh, S. K., Chakravarty, J. K., & Tyagi, A. K., Chemistry of one dimensional silicon carbide materials: Principle, production, application and future prospects, *Progress in Solid State Chemistry*, 43(3), 2015, pp. 98–122.
2. Yang, Y., Yang, K., Lin, Z. M., & Li, J. T., Mechanical-activation-assisted combustion synthesis of SiC, *Materials Letters*, 61(3), 2007, pp. 671–676.
3. Elyassi, B., Kim, T. W., Sahimi, M., & Tsotsis, T. T., Effect of polystyrene on the morphology and physical properties of silicon carbide nanofibers. *Materials Chemistry and Physics*, 118(1), 2009, pp. 259–263.
4. Jin, H. B., Li, J. T., Cao, M. S., & Agathopoulos, S. Influence of mechanical activation on combustion synthesis of fine silicon carbide (SiC) powder. *Powder Technology*, 196(2), 2009, pp. 229–232.
5. Krzysztof Górecki, J. Z, The Influence of Diodes and Transistors Made of Silicon and Silicon Carbide on the Nonisothermal Characteristics of Boost Converters. *Informacije MIDEM*, 42(3), 2012, pp. 176–184.
6. Sviličić, B., Mastropaolo, E., & Cheung, R. (2013). Two-port piezoelectric silicon carbide MEMS cantilever resonator. *Informacije MIDEM*, 43(1), 2013, pp. 22–26.
7. Zhu, J., Wu, H., Chen, H. T., Wu, X. L., & Xiong, X. Tunable violet–blue emission from 3C-SiC nanowires. *Physics Letters A*, 373(18–19), 2009, pp. 1697–1700.
8. Li, B., Song, Y.-C., Zhang, C.-R., & Yu, J.-S. Synthesis and characterization of nanostructured silicon carbide crystal whiskers by sol–gel process and carbothermal reduction. *Ceramics International*, 40(8), 2014, pp. 12613–12616.
9. Raman, V., Bahl, O. P., & Dhawan, U. Synthesis of silicon carbide through the sol-gel process from different precursors. *Journal of Materials Science*, 30, 1995, pp. 2686–2693
10. Lin, M., Loh, K. P., Boothroyd, C., & Du, A. Y. Nanocantilevers made of bent silicon carbide nanowire-in-silicon oxide nanocones. *Applied Physics Letters*, 85(22), 2004, pp. 5388–5390.
11. Agrawal, D. K. Microwave processing of ceramics. *Current Opinion in Solid State and Materials Science*, 3(5), 1998, pp. 480–485.
12. Mingos, D. M. P. Microwave syntheses of inorganic materials. *Advanced Materials*, 5(11), 1993, pp. 857–859.
13. Oghbaei, M., & Mirzaee, O. Microwave versus conventional sintering: A review of fundamentals, advantages and applications. *Journal of Alloys and Compounds*, 494(1–2), 2010, pp. 175–189.

14. Rao, K. J., Vaidhyanathan, B., Ganguli, M., & Ramakrishnan, P. a. Synthesis of Inorganic Solids Using Microwaves. *Chemistry of Materials*, 11, 1999, pp. 882–895.
15. Millos, C. J., Gavin Whittaker, A., & Brechin, E. K. Microwave heating - A new synthetic tool for cluster synthesis. *Polyhedron*, 26(9–11), 2007, pp. 1927–1933.
16. Belmonte, T., Henrion, G., Cardoso, R. P., Noel, C., Arnoult, G., & Kosior, F. (2008). Microwave Plasmas at Atmospheric Pressure: New Theoretical Developments and Applications in Surface Science. *Informacije MIDEM*, 38(4), 2008, pp. 272–276.
17. Vesel, A., Mozetic, M., & Balat-Pichelin, M. (2011). Absorption of microwave power in nitrogen plasma at moderately low pressure. *Informacije MIDEM*, 41(1), 2011, pp. 18–21.
18. Kepenienė, V., Tamašiūnaitė, L. T., Ienė, J. J., Vaičiūnienė, J., Kondrotas, R., & As, V. P. Platinum-Niobium (V) Oxide / Carbon Nanocomposites Prepared By Microwave Synthesis For Ethanol Oxidation. *Materials Science*, 22(2), 2016: pp 243–248.
19. Meng, F., Wang, X., Jiang, D., & Ma, R. Microwave Absorbing and Magnetic Properties of the Polyaniline-. *Materials Science*, 22(3), 2016: pp 354–357.
20. Zong, B., Wu, Y., Phuoc, N. N., Ho, P., Qiu, J., Yang, Y., Han, G. Quick fabrication of appropriate morphology and composition CoFe films with desirable microwave properties. *Int. J. Mater. Res.*, (110), pp. 1077–1085.
21. Xing, R., Guo, J., Miao, C., Liu, S., & Pan, H. Fabrication of protein-coated CdS nanocrystals via microwave-assisted hydrothermal method. *Journal of Experimental Nanoscience*, 9(6), 2014, pp. 582–587.
22. He, C. L., & Chen, Y. Q. Calorimetry Study of Microwave Absorption of Some Solid Materials. *Journal of Microwave Power and Electromagnetic Energy*, 47(4), 2013, pp. 251–261.
23. Kim, T., Lee, J., & Lee, K.-H. Microwave heating of carbon-based solid materials. *Carbon letters*, 15(1), 2014, pp. 15–24.
24. Koguchi, M., Kakibayashi, H., Yazawa, M., Hiruma, K., & Katsuyama, T. Crystal Structure Change of GaAs and InAs Whiskers from Zinc-Blende to Wurtzite Type. *Japanese Journal of Applied Physics*, 31(7R), 1992, pp. 2061.
25. Martin, A., Schopf, C., Pescaglini, A., O’Riordan, A., & Iacopino, D. Synthesis, optical properties and self-assembly of gold nanorods. *Journal of Experimental Nanoscience*, 7(6), 2012, pp. 688–702.
26. Fung, M. K., Ng, A. M. C., Djurišić, A. B., Chan, W. K., & Wang, H. Preparation of 8-hydroxyquinoline wires by decomposition of tris(8-hydroxyquinoline) aluminium. *Journal of Experimental Nanoscience*, 7(5), 2012, pp. 578–585.
27. Wang, Q., Li, Y., Jin, S., & Sang, S. Catalyst-free hybridization of silicon carbide whiskers and expanded graphite by vapor deposition method. *Ceramics International*, 41(10), 2015, pp. 14359–14366.
28. Li, J., Shirai, T., & Fuji, M. Rapid carbothermal synthesis of nanostructured silicon carbide particles and whiskers from rice husk by microwave heating method. *Advanced Powder Technology*, 24(5), 2013, pp. 838–843.
29. Quah, H.-J., Cheong, K. Y., & Lockman, Z. Stimulation of silicon carbide nanotubes formation using different ratios of carbon nanotubes to silicon dioxide nanopowders. *Journal of Alloys and Compounds*, 475(1–2), 2008: pp 565–568.
30. Zhao, B., Zhang, H., Tao, H., Tan, Z., Jiao, Z., & Wu, M. Low temperature synthesis of mesoporous silicon carbide via magnesiothermic reduction. *Materials Letters*, 65(11), 2011: pp 1552–1555.
31. Rajarao, R., Ferreira, R., Sadi, S. H. F., Khanna, R., & Sahajwalla, V. Synthesis of silicon carbide nanoparticles by using electronic waste as a carbon source. *Materials Letters*, 120, 2014: pp 65–68.
32. Coates, J. Interpretation of Infrared Spectra, A Practical Approach. *Encyclopedia of Analytical Chemistry*, 2000: pp 10815–10837.
33. Chiu, S.-C., & Li, Y.-Y. SiC nanowires in large quantities: Synthesis, band gap characterization, and photoluminescence properties. *Journal of Crystal Growth*, 311(4), 2009: pp 1036–1041.
34. Li, Y., Chen, C., Li, J.-T., Yang, Y., & Lin, Z.-M. Surface charges and optical characteristic of colloidal cubic SiC nanocrystals. *Nanoscale research letters*, 6(1), 2011: pp 454.
35. y. Verd Francisco Arredondo. *Cerámica y vidrio*, 279(c), 1969: pp 279–284
36. RenbingWu, LinglingWu, Guangyi Yang, Yi Pan, Jianjun Chen, R. Z. and J. L. Fabrication and photoluminescence of bicrystalline SiC nanobelts. *Journal of Physics D: Applied Physics*, 40(12), 2007: pp 3697.
37. Nandawar, R., Purnima, S., & Fozia, Z. H. Synthesis and characterization of SiO<sub>2</sub> nanoparticles by sol-gel process. *Indian Journal of Science*, 1(1), 2012: pp 6–10.
38. Corriu, R. J. P., Gerbier, P., Guérin, C., & Henner, B. Poly[(silylene)diacetylene]/fine metal oxide powder dispersions: use as precursors to silicon-based composite ceramics. *Journal of Materials Chemistry*, 10(9), 2000: pp 2173–2182.
39. Menéndez, J. a, Abdul Rahman, R., Arenillas, B. F., Y. Fernández, L. Z., E.G.Calvo, & J.M.Bermúdez. Microwave heating processes involving carbon materials. *Fuel Processing Technology*, 91(1), 2010, pp. 1–8.
40. Stuerger, D. Microwave-Material Interactions and Dielectric Properties, Key Ingredients for Mastery of Chemical Microwave Processes. In *Microwaves*

- in *Organic Synthesis* (Vol. 1, pp. 1–61). 2008, pp. Weinheim, Germany: Wiley-VCH Verlag GmbH.
41. Li, X., Zhang, G., Tang, K., Ostrovski, O., & Tronstad, R. synthesis of silicon carbide by carbothermal reduction of quartz in h<sub>2</sub>-ar gas mixtures, 2015, pp. 548–554.
  42. Li, X., Zhang, G., Tang, K., Ostrovski, O., & Tronstad, R. Carbothermal Reduction of Quartz in Different Gas Atmospheres. *Metallurgical and Materials Transactions B: Process Metallurgy and Materials Processing Science*, 46(3), 2015, pp. 1343–1352.
  43. Cetinkaya, S., & Eroglu, S. Chemical vapor deposition of C on SiO<sub>2</sub> and subsequent carbothermal reduction for the synthesis of nanocrystalline SiC particles/whiskers. *Journal of the European Ceramic Society*, 31(5), 2011, pp. 869–876.
  44. Fu, Q.-G., Li, H.-J., Shi, X.-H., Li, K.-Z., Wei, J., & Hu, Z.-B. Synthesis of silicon carbide nanowires by CVD without using a metallic catalyst. *Materials Chemistry and Physics*, 100(1), 2006, pp. 108–111.
  45. Dehghanzadeh, M., Ataie & Heshmati-Manesh, S. synthesis of nanosize silicon carbide powder by carbothermal reduction of sio<sub>2</sub>. *International Journal of Modern Physics: Conference Series*, 5, 2012, pp. 263–269.
  46. Weimer, A. W., Nilsen, K. J., Cochran, G. A., & Roach, R. P. Kinetics of carbothermal reduction synthesis of beta silicon carbide. *AIChE Journal*, 39(3), 1991, pp. 493–503.
  47. Lee, J. G., Miller, P. D., & Cutler, I. B. carbothermal reduction of silica Department of Materials Science and Engineering University of Utah, Salt Lake City, Utah 84112 (U.S.A.), 84112(1), pp. 707–711.
  48. Changhong, D., Xianpeng, Z., Jinsong, Z., Yongjin, Y., Lihua, C., & Fei, X. The synthesis of ultrafine SiC powder by the microwave heating technique. *Journal of Materials Science*, 32(9), 1997, pp. 2469–2472.
  49. Dijen, F. K. Van. The Chemistry of the Carbothermal Synthesis of / 3-SiC : Reaction Mechanism , Reaction Rate and Grain Growth, 7(199 I), 1991, pp. 177–184.
  50. Kavitha, N., Balasubramanian, M., & Vashistha, Y. D. Synthesis and Characterization of Nano Silicon Carbide Powder from Agricultural Waste. *Transactions of the Indian Ceramic Society*, 70(3), 2011, pp. 115–118.
  51. Li, Y., Wang, Q., Fan, H., Sang, S., Li, Y., & Zhao, L. Synthesis of silicon carbide whiskers using reactive graphite as template. *Ceramics International*, 40(1), 2014, pp. 1481–1488.

Arrived: 15. 03. 2017

Accepted: 26. 07. 2017





# *A Compact Radio Telescope for the 21 cm Neutral-Hydrogen Line*

*Tadeja Saje, Matjaž Vidmar*

**Abstract:** Thanks to the many independent technological achievements in the recent years, serious radio astronomy is again within reach of amateur astronomers. Observation of the  $\lambda=21$  cm neutral-hydrogen line is relatively straightforward, since the strongest hydrogen clouds in our galaxy achieve an equivalent back-body brightness temperature of around  $T \approx 100$  K. Yet such observation provides important information about the structure and velocity of our galaxy. In this article the design, construction and calibration of a suitable radio telescope is discussed in detail making efficient use of available hardware and software. Important practical details like radio-interference mitigation in an urban environment are also discussed. Finally, the results obtained with the prototype radio telescope are presented both as the hydrogen spectra in selected directions as well as a 3D map (galactic longitude, galactic latitude and velocity profile) of our Milky Way galaxy visible from our latitude  $46^\circ$  north.

**Keywords:** radio telescope; LNA; band-pass filter; hydrogen line; radio astronomy; feed horn.

## *Radioteleskop za 21 cm vodikovo črto*

**Izvleček:** Številni med sabo neodvisni tehnološki dosežki zadnjih nekaj let omogočajo, da je resna radioastronomija ponovno dostopna amaterskim astronomom. Opazovanje spektralne črte atomarnega vodika  $\lambda=21$  cm je razmeroma preprosto, saj spektralna svetlost najmočnejših oblakov vodika v naši galaksiji dosega enakovredno temperaturo sevanja črnega telesa okoli  $T \approx 100$  K. Hkrati takšno opazovanje daje pomembne informacije o sestavi in hitrosti naše galaksije. V tem prispevku so podrobno opisani načrtovanje, izgradnja in umerjanje primerne radioteleskopa ob učinkoviti uporabi razpoložljive strojne in programske opreme. Opisane so tudi pomembne praktične podrobnosti, kot je izogibanje radijskim motnjam v mestnem okolju. Končno, rezultati meritev z izdelanim prototipom radioteleskopa so prikazani kot spektri atomarnega vodika v izbranih smereh in kot 3D zemljevid (galaktična dolžina, galaktična širina in profil hitrosti) naše galaksije Rimske ceste, kot jo vidimo iz naše zemljepisne širine  $46^\circ$  severno.

**Ključne besede:** radioteleskop; LNA; pasovno prepustno frekvenčno sito; vodikova črta; radioastronomija, žarilec.

\* Corresponding Author's e-mail: [tadeja.saje@gmail.com](mailto:tadeja.saje@gmail.com)

### *1 Amateur radio astronomy*

For many thousand years, astronomy was limited to optical observations in the visible part of the electromagnetic spectrum. Finally, in middle of the 20<sup>th</sup> century the first successful observations of celestial radio and microwave sources were made. Today astronomical observations are made over all of the electromagnetic spectrum. Space-based telescopes may be required at wavelengths where the Earth's atmosphere is opaque to electromagnetic waves.

Visible-light observations remain the most popular even today. Large and extremely expensive professional instruments are located at carefully-selected remote sites with clear skies and low levels of light pollution. Besides these large professional instruments, amateur optical observations with much smaller instruments lo-

cated at non-perfect sites still play an important role in the science of astronomy. For example, most new asteroids are discovered by amateur observers.

Although the very first radio map of the sky was plotted by an amateur astronomer, Grote Reber in 1938-1946 [1], radio astronomy quickly evolved into using extremely large antennas and sophisticated signal processing, all of them out of reach of amateurs. On the other side, it is worth noting that the most important discoveries of early radio astronomy like the non-thermal radiation of many celestial sources including the Sun, the  $\lambda=21$  cm neutral-hydrogen line or the cosmic background radiation were made with relatively simple equipment originally designed for a completely different purpose.

Things started changing in favor of amateur radio astronomy after about 1990. The widespread deployment of satellite television made medium-size parabolic antennas and corresponding positioners available to amateurs. The semiconductor industry mastered III-V semiconductors, in particular GaAs based HEMTs allowing exceptionally low-noise receivers operating at room temperature well into the microwave region. Both allowed successful amateur observations of the  $\lambda=21\text{cm}$  neutral-hydrogen line [2].

At the turn of the century, television broadcasting shifted from analog to digital. Several analog microwave point-to-point link and analog satellite-television antennas were decommissioned since large antennas are no longer required by the new, more efficient digital modulations. The computing power of personal computers and corresponding interfaces increased to allow the comprehensive signal processing required for digital-television reception. Both allowed very successful radio-astronomical observations with amateur means [3, 4].

Radio astronomy excels in interferometry, especially VLBI. While smaller baseline interferometers could work with dedicated microwave point-to-point links, VLBI usually required sophisticated synchronization with atomic clocks and physical transfer of high-capacity magnetic-tape recordings for further processing. Today global navigation satellite systems (GPS, GLONASS and similar) offer precise worldwide synchronization of local clocks as well as local correction for unwanted propagation effects like ionospheric or tropospheric delays. The fiber-optic network offers high-capacity worldwide internet connectivity. Since both inexpensive synchronization and inexpensive data transfer is available to amateurs, the major achievements of amateur radio astronomy are yet to come.

In this article the design, construction and calibration of a compact radio telescope is discussed in detail. The latter can produce 3D maps of the hydrogen distribution in our galaxy. Much of the described hardware and software can be used to observe other celestial sources, like point and distributed continuum sources, a few neighbor galaxies, some of the strongest pulsars etc. Finally, several such radio telescopes could be combined into a powerful interferometer.

## 2 Radio-telescope design

### 2.1 System requirements

The  $\lambda=21\text{cm}$  neutral-hydrogen line is not emitted by dense celestial objects like stars, but by lone hydrogen

atoms in the interstellar medium. The density of the interstellar medium in a galaxy may be very low, just a few thousand particles in a cubic meter of space. Most of this interstellar matter is atomic hydrogen. This hydrogen has two energy levels in its electronic ground state with an energy difference corresponding to a frequency of  $f_0=1420405751.7667\text{Hz}$ . The upper level can be excited by the collision of two atoms. This excited level then decays after an average lifetime of 11 million years by emitting a photon at the frequency mentioned.

Yet our Milky Way and other galaxies are very large objects. Although the interstellar space can be considered rather high vacuum, the few lone hydrogen atoms represent a significant fraction of the total mass of a galaxy or other celestial body. The mass ratio varies: there are celestial objects with lots of sparse hydrogen atoms and few visible stars and the opposite is also possible. Due to the huge size of interstellar space, the radiation at  $\lambda=21\text{cm}$  sums up to significant and detectable values.

Since relative velocities between different parts of our Milky Way galaxy span up to  $\Delta v \approx \pm 200\text{km/s}$ , the expected Doppler shift is in the range of  $\Delta f \approx \pm 1\text{MHz}$  around a central frequency of  $f_0 \approx 1420.4\text{MHz}$ . Other galaxies are moving at even higher velocities with respect to us resulting in much larger Doppler shifts. Most important of all, the Doppler shift of the hydrogen line allows precise velocity measurements revealing the motions of celestial objects. The frequency band from  $f_{MIN} = 1400\text{MHz}$  to  $f_{MAX} = 1427\text{MHz}$  is therefore protected worldwide for radio-astronomy use.

The  $\lambda=21\text{cm}$  neutral-hydrogen radiation from the Milky Way is coming from distributed sources with angular diameters of several degrees and an equivalent back-body brightness temperature of up to  $T \approx 100\text{K}$ . Such sources can be reliably detected with rather small antennas with a diameter above  $d > 1\text{m} \approx 5\lambda$ . Using a slightly larger antenna  $d \approx 3\text{m} \approx 15\lambda$  already reveals the spiral structure of the Milky Way.

The receiving system of any radio telescope should add the lowest possible own noise to the weak celestial signals. The receiving system noise includes the antenna noise and the receiver electronics noise. The antenna noise mainly comes from unwanted side lobes of its radiation pattern picking up thermal radiation of the warm neighborhood. Modern semiconductor devices produce a similar amount of noise when operated at room temperature. The sum of both is in the range  $T_s = 50\text{...}100\text{K}$  for relatively small antennas  $d \approx 15\lambda$  and available low-noise amplifiers.

### 2.2 Block diagram

The design of the described compact radio telescope is based on available components: a 3.1m (10 feet) diameter surplus parabolic mesh reflector originally manufactured by EchoStar and intended for satellite-television reception in the 4GHz band. The parabolic dish is installed on an EGIS azimuth/elevation rotor EPR-203. Its corresponding control unit EPS-103 allows computer control through an RS-232 interface. A convenient solution is to run Python scripts on a personal computer to track a selected object in the sky and/or scan the galactic plane as shown on Figure 1.

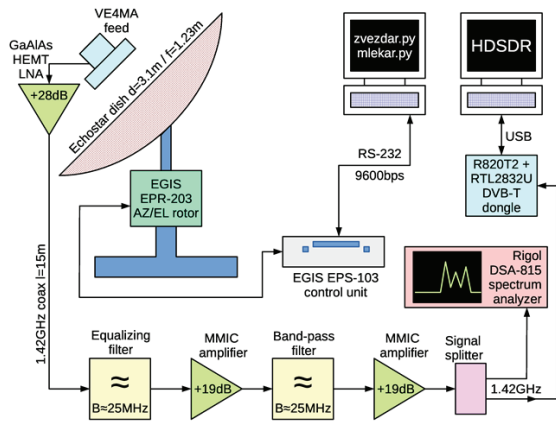


**Figure 1:** Block diagram of a compact hydrogen-line radio telescope.

Other parts of the radio telescope have to be custom designed and built. The VE4MA antenna-feed design is a good compromise among parabolic-mirror illumination efficiency, unwanted side lobes picking up noise and aperture blocking. Of course, the best available HEMTs have to be used in the low-noise amplifier. Since 1.42GHz is not a particularly high frequency for modern electronics, frequency conversions are not required. The custom signal processing only includes custom-designed band-pass filters for 1.42GHz and additional amplifiers to overcome the relatively high noise of available receivers.

Further signal processing is split into two independent branches. A quick look at the received signal as well as interference threats is provided by a standard, scanning-receiver type spectrum analyzer Rigol DSA-815. Much more efficient signal processing can be performed with a FFT spectrum analyzer once the wide dynamic range of a scanning-receiver spectrum analyzer is no longer required. FFT spectrum analysis can be performed efficiently on modern personal computers using an inexpensive DVB-T dongle as the analog interface.

### 2.3 Antenna and positioner

The antenna of a radio telescope requires an unobstructed view to a much larger part of the sky than a typical satellite-television antenna covering the geostationary arc. In particular, on the northern hemisphere a radio telescope should have an unobstructed view in the direction south. It therefore makes sense to install a small radio telescope on the roof or other elevated place to avoid local obstacles as shown on Figure 2.



**Figure 2:** Mesh reflector with feed, LNA and azimuth/elevation positioner.

The spatial resolution of any radio telescope depends on the antenna size. Assuming an uniform illumination of the antenna aperture, the spatial resolution of the described single-antenna radio telescope is estimated as:

$$\alpha = 1.22 \cdot \frac{\lambda}{d} = 1.22 \cdot \frac{0.21m}{3.1m} = 0.083rd \approx 4.7^\circ \quad (1)$$

In the case of a radio telescope, the antenna requires two-axis rotation. An azimuth/elevation or X/Y rotator can be used to keep the antenna pointed to a particular source in the sky in spite of the rotation of the Earth. On the other hand, the rotation of the Earth is frequently used in many radio-telescope designs as an additional axis of rotation. In the described radio telescope, all three available axis of rotation (two-axis positioner and Earth) can be used depending on the desired scan operation. The EGIS azimuth/elevation rotor EPR-203 is equipped with gears for 360° azimuth range and 90° elevation range.

### 2.4 Feed design

In the microwave frequency range, the sky noise is usually much lower than the ground noise. The equivalent

black-body temperature of the sky may be less than  $T_{SKY} < 10K$  while the ground noise is close to  $T_{GROUND} \approx 290K$ . Large satellite-receiving antennas and radio telescopes are designed to avoid collecting ground noise through side lobes of their radiation patterns. Antennas larger than  $d > 100 \lambda$  are frequently built as dual-reflector Cassegrain telescopes. In this way any spillover of the feed sees the cold sky over the edge of the secondary reflector.

An alternative solution is to control the radiation pattern of the feed using a corrugated horn or a corrugated flange. Neither solution is practical with small, rotational-symmetric parabolic mirrors due to the blockage of the relatively large secondary mirror or corrugated feed. An efficient solution for small  $d < 30 \lambda$  parabolic mirrors is a simple circular-waveguide horn with the Kumar choke [5], also known as the VE4MA feed [6] as shown on Figure 3.

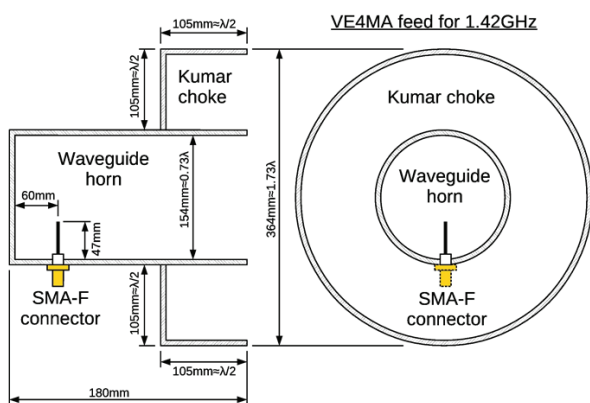


Figure 3: VE4MA feed design.

Changing the diameter of the circular waveguide, the dimensions of the Kumar choke as well as its position relative to the horn aperture allows optimizing the VE4MA feed for deep, rotational-symmetric parabolic mirrors with focal-to-diameter ratios in the range  $f/d = 0.3 \dots 0.5$ . The dimensions shown on Figure 3 should be close to optimal for our EchoStar mesh dish with a focal-to-diameter ratio of  $f/d = 0.4$  at a central frequency of  $f_0 = 1.42GHz$ .

The described VE4MA feed was practically implemented from pieces of thin aluminum sheet bolted together with several M3 screws as shown on Figure 4. The position of the Kumar choke with respect to the horn aperture was adjusted experimentally for the lowest system noise temperature  $T_s$  as shown on Figure 4.

The efficiency of the Kumar choke was further checked by measuring the radiation pattern of the feed both with the Kumar collar and the bare waveguide horn with the choke removed. The measurements also show important side effects that might impair the performance of the radio- telescope antenna.



Figure 4: Practical implementation of the VE4MA feed.

For example, a circular waveguide only supports the propagation of its fundamental  $TE_{11}$  mode when its diameter exceeds  $d_{TE11} > 0.586 \lambda$ . Using a simple, non-symmetric probe to excite the fundamental  $TE_{11}$  mode, higher order modes may also be excited. The next higher mode is the  $TM_{01}$  mode that appears at  $d_{TM01} > 0.765 \lambda$ . Since the circular-waveguide diameter was selected as  $d = 0.73 \lambda$  rather close to the  $TM_{01}$  cutoff, the latter does not receive much attenuation in a short waveguide horn. The final result is a squint of the waveguide-horn main radiation lobe in the E plane. Fortunately the Kumar choke in the VE4MA feed is able to correct this defect as shown on Figure 5.

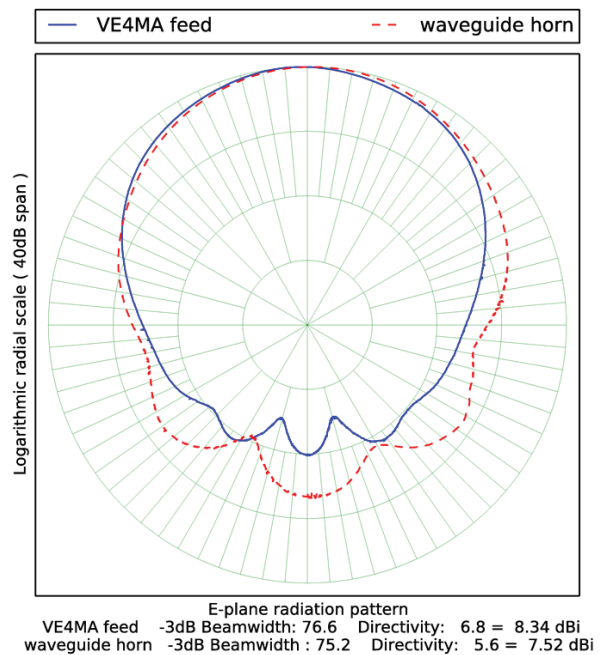
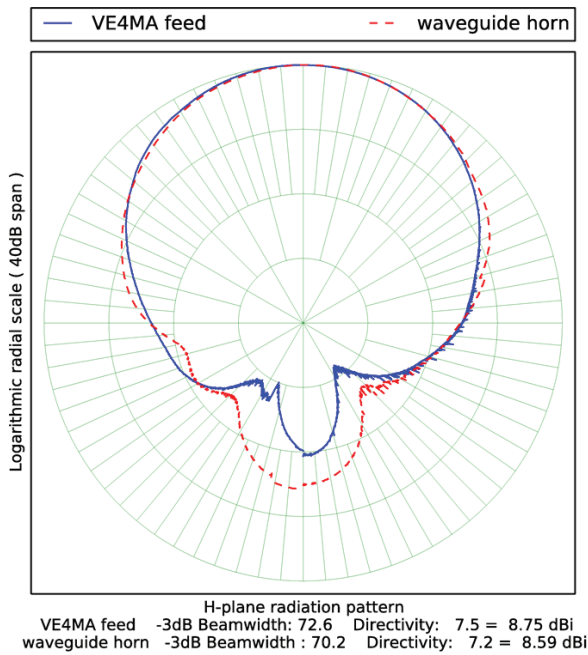


Figure 5: Measured feed E-plane radiation pattern.

Little if any squint is visible in the measured H-plane radiation pattern of the bare waveguide horn as compared to the VE4MA feed on Figure 6.





**Figure 6:** Measured feed H-plane radiation pattern.

In both E and H planes, the Kumar choke provides a substantial improvement of the feed radiation pattern resulting in a more than 5dB decrease of its unwanted side lobes. Further, the VE4MA feed exhibits a much better rotational symmetry than the bare waveguide horn. The improved feed radiation pattern allows a substantially lower system noise as measured during the calibration in section 3.2. of this article.

The radio emissions of certain celestial sources are polarized, while radio emissions from other celestial sources are not polarized. The radio emission of neutral hydrogen atoms at  $\lambda=21\text{ cm}$  is not polarized. Therefore the polarization of a simple radio telescope for the neutral-hydrogen line may be arbitrary. The simplest solution is to use linear polarization as with the described linearly-polarized VE4MA feed. Both horizontal linear polarization and vertical linear polarization were experimented with identical results.

While using linearly-polarized feeds with relatively small  $d < 30 \lambda$ , rotational-symmetric parabolic mirrors, a new problem appears. A significant part of the feed radiation is reflected by the parabolic mirror back into the same feed. Considering the described mesh dish with a focal  $f=1.23\text{ m}$  and the described VE4MA feed with a gain of about  $G \approx 8.55\text{ dBi} \approx 7.15$  at  $\lambda=21\text{ cm}$ , the magnitude of the described reflection can not be neglected:

$$|\Gamma| = \frac{G \cdot \lambda}{4\pi \cdot f} \approx 0.097 \approx -20.3\text{ dB} \quad (2)$$

This additional reflection may either degrade or improve the feed impedance matching, since the overall antenna return loss is a phasor sum of the different reflections involved. On the other hand, the noise performance of very low-noise microwave receivers is very sensitive to the source (antenna) impedance matching. Some low-noise receivers may even become unstable when connected to a badly mismatched antenna.

The return loss of the described bare VE4MA feed in free space was measured as  $|\Gamma| = -13.4\text{ dB}$  using a directional coupler with a measured directivity better than  $-30\text{ dB}$ . After installing the feed in the focal point of the parabolic mirror, the return loss of the whole antenna improved to  $|\Gamma| = -17.8\text{ dB}$  at  $f_0 = 1.42\text{ GHz}$ . This return loss was considered good enough so that any further modifications to the feed were considered unnecessary.

The above discussion is no longer valid if a parabolic mirror with a different focal length from ours is used, since the phase of the reflection from the dish changes really quickly and is proportional to twice the focal length! Using an arbitrary parabolic mirror, the impedance matching of the complete antenna should always be checked. In the worst case, the feed design, in particular the probe length and its position inside the waveguide horn may need to be changed.

### 2.5 LNA design

The semiconductor devices of choice for microwave low-noise amplifiers (LNAs) are high- electron mobility transistors (HEMTs) based on GaAs. The best commercially-available devices are designed to operate in a  $Z_k = 50\Omega$  characteristic-impedance environment in the frequency range around  $f_0 = 12\text{ GHz}$  for satellite-television reception. Such devices are therefore not optimized for operation at the neutral-hydrogen frequency of  $f_0 = 1.42\text{ GHz}$ .

Similar HEMT structures with a much wider gate are required for low-noise operation in a  $Z_k = 50 \Omega$  environment at L-band frequencies. Besides not being volume-production items, wider-gate devices operate at higher currents increasing the power dissipation. The latter increases the chip temperature impairing their noise performance. It therefore makes sense to use standard 12GHz HEMT devices even at much lower frequencies but in a higher-impedance environment as described in [7].

The circuit published in [7] was originally designed for GaAs MESFETs that operated at about  $V_{DS} \approx 4\text{ V}$ . Modern low-noise GaAlAs/GaAs HEMTs operate at much lower voltages  $V_{DS} \approx 1.5\text{ V}$ . Operation of a low-noise HEMT at higher voltages may affect its reliability and trigger

long-term degradation effects. In order to improve the reliability with HEMT devices, the simple source-bias resistor from [7] was replaced with an active bias circuit including a low-frequency silicon NPN transistor.

When a Ku-band HEMT or MESFET is operated at L band, an efficient input-impedance match for lowest noise is a series inductor with the gate while no special output-impedance matching at the drain is required. A two-stage amplifier design offers around  $G_{LNA} \approx 30\text{dB}$  of gain at reasonable stability. Both gain and stability can be adjusted with the inter-stage match. A GaAs MESFET can be used in the second stage as shown on Figure 7.

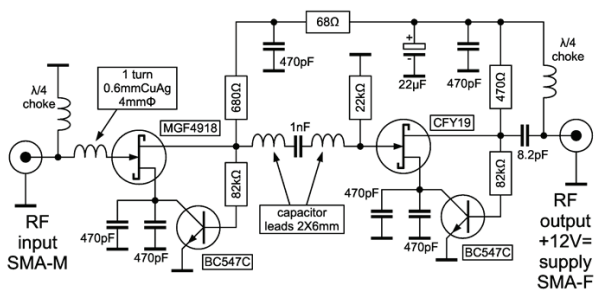


**Figure 7:** LNA circuit diagram.

In order to operate at higher impedances, the circuit of the LNA is not built on a printed- circuit board. The circuit of the LNA is supported in free air by several lead-less 470pF ceramic disc capacitors soldered to the bottom of a small brass box. The remaining components are traditional parts (not SMD) with wire leads. Although such a design is not suitable for volume production, it makes sense to achieve top performance of the radio telescope. The supply voltage +12V= is fed through the output SMA connector using a bias tee at the other end of some 15m of coaxial cable feeding the indoor equipment. The input connector is a male SMA to be screwed directly on the antenna feed to avoid any feed-line losses as shown on Figure 8.



**Figure 8:** Practical implementation of the LNA.

Many LNA prototypes were built using different GaAs devices either in the original circuit [7] or with the modified bias as shown above. Both MESFETs and HEMTs could readily achieve noise temperatures in the  $T_{LNA} \approx 30\text{K}$  range as measured with a HP8970 noise-figure meter equipped with a HP364A ENR $\approx 5\text{dB}$  calibrated noise source. The best LNA samples could reach even  $T_{LNA} = 25\text{K}$  at a room temperature of 20°C (293K)

after carefully adjusting the input impedance match. HEMTs typically provide much more gain than MESFETs, therefore using HEMTs in both stages may lead to instability.

The LNA is followed by the indoor receiver with a noise temperature in the  $T_{RX} \approx 290\text{K}$  (room temperature) range. Considering an  $a_{COAX} = -10\text{dB}$  cable loss to the rooftop antenna and a LNA gain of  $G_{LNA} \approx 30\text{dB}$ , the indoor receiver adds about  $T_{RX}' \approx 3\text{K}$  of noise to the whole radio telescope noise temperature.

### 2.6 Signal processing and distribution

A carefully-designed LNA may contribute less than  $T_{LNA} \approx 30\text{K}$  to the total system noise of the radio telescope, but other components may be much noisier. For example, a good radio- frequency spectrum analyzer has a noise figure in the  $F_{SA} \approx 25\text{dB}$  range corresponding to a noise temperature of about  $T_{SA} \approx 10^5\text{K}$ . A  $G_{LNA} \approx 30\text{dB}$  LNA followed by  $a_{COAX} = -10\text{dB}$  cable loss sets the contribution of the spectrum analyzer to an unacceptable  $T_{RX}' \approx 1000\text{K}$  to the total system noise or in other words more than one order of magnitude larger than any other noise source in the system.

Additional low-noise amplification is therefore required in front of spectrum analyzers and other “deaf” instrumentation. Additional amplification brings a new problem: a high-gain amplifier chain may easily be driven into saturation by strong terrestrial radio transmitters operating at nearby frequencies. The whole signal processing and distribution chain includes a bias tee for the LNA, a first band-pass filter, a MMIC amplifier, another band-pass filter, another MMIC amplifier, a power splitter and a SDR receiver front-end as shown on Figure 9.

Microwave filters can be built in many different technologies. For the radio-astronomy frequency band at

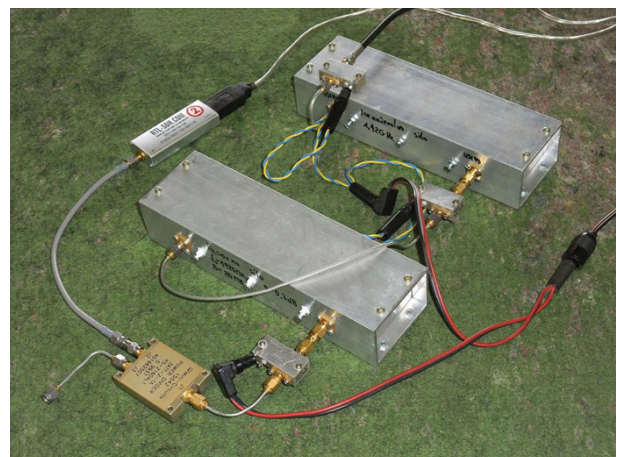


**Figure 9:** Signal processing and distribution chain.

1.42GHz any filters have to be custom designed and built therefore excluding high-volume technologies like SAW devices. Considering low-volume applications, cavity filters are simple to manufacture from standard aluminum tubing yet individual  $\lambda/4$  resonators achieve an unloaded quality in excess of  $Q_U > 1000$ . A comb arrangement of the individual  $\lambda/4$  resonators allows a more compact band-pass filter than an interdigital design. Considering the filtering requirements of the radio telescope, two separate but almost identical comb filters with three  $\lambda/4$  resonators each are required as shown on Figure 10.

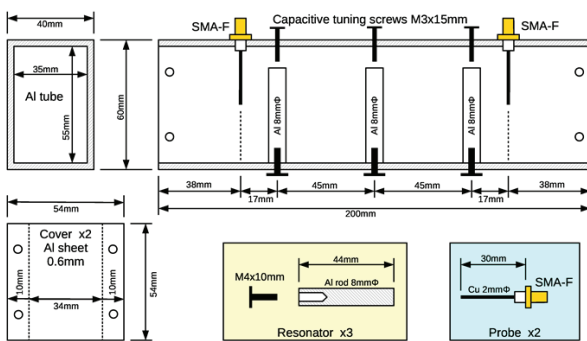


**Figure 10:** Comb-filter design.

The input and output coupling is achieved with probes similar to the one used to excite the waveguide horn. The three resonators are made from 8mm diameter aluminum rod, while the cavity is made from standard aluminum tube of rectangular cross-section of 40mmX60 mm and 2.5mm thick walls. The rectangular tube extends 38mm beyond the probe positions so that the electromagnetic field already decays inside the tube. Covers on both sides of the tube are only required to keep dust and dirt outside of the filter cavity as shown on Figure 11.

The described simple all-aluminum construction with few junctions provides excellent electrical performanc-



**Figure 11:** Inside the comb-filter cavity.

es that stay stable in time. The  $\lambda/4$  resonators are tuned to the exact frequency with capacitive tuning screws in the opposite wall of the cavity. The bandwidth is selected to cover the whole 1.42GHz radio-astronomy frequency band. An order-of-magnitude narrower filter could be used to observe the neutral-hydrogen radiation only from our Milky Way galaxy.

At a pass-band bandwidth of  $B \approx 25\text{MHz}$  the high unloaded quality of the individual resonators allows a low insertion loss of the whole three-stage filter in the  $a_{BPF} \approx -0.5\text{dB}$  range. The exact value of the latter is a function of the actual filter alignment as visible on the measured response on Figure 12.

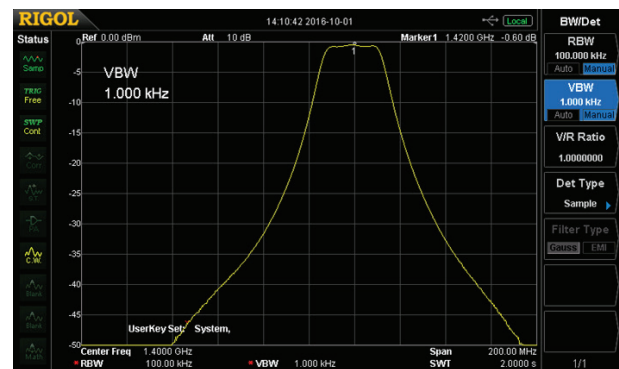


**Figure 12:** Measured comb-filter response.

Unfortunately, other components of the radio telescope do not exhibit such a flat frequency response over the 1.42GHz radio-astronomy band. Since most of the ripple comes from the reflections at both ends of the relatively long coaxial cable between the outdoor LNA and the indoor processing chain, it makes sense to adjust the first cavity filter to flatten the overall frequency response of the radio telescope. In this way the first filter is also used as an equalizing filter.

The additional signal gain is provided by two MMIC amplifiers manufactured by Mini-Circuits in InGaP HBT technology. The amplifier chips are packaged in SOT-89 plastic packages that provide good radio-frequency ant thermal performance at the same time. Both packaged amplifiers are installed on printed-circuit boards together with a few bias components. Finally both printed- circuit boards are installed in aluminum cases with SMA connectors as shown on Figure 13.

A low-noise MMIC Gali-52+ is used in the first stage providing a measured gain of  $G_{52} = 19.3\text{dB}$  with a measured noise figure of  $F_{52} = 2.8\text{dB}$  in the 1.42GHz band. A power MMIC Gali-5+ is used in the second stage providing a measured gain of  $G_5 = 19.1\text{dB}$  with a measured noise figure of  $F_5 = 4.1\text{dB}$  in the 1.42GHz band.



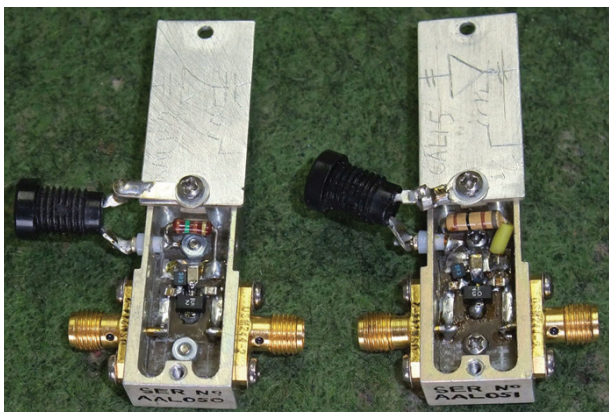


**Figure 13:** Packaged MMIC amplifiers.

The gain of the whole chain including two band-pass filters and two MMIC amplifiers approaches  $G \approx 37\text{dB}$ . The latter is high enough to neglect the noise contribution of a spectrum analyzer or software-defined radio (SDR) front end. A Wilkinson power divider with a splitting loss of  $a_w \approx -3\text{dB}$  is used to supply two independent instruments at the same time.

### 3 Instrument calibration

#### 3.1 Positioner calibration

No matter what directional antenna and corresponding positioner are used, after installation both need accurate mechanical calibration before they can be used for satellite communications and/or radio-astronomy work. In particular, the available EGIS azimuth/elevation rotor EPR-203 has a linear tooth-gear transmission for rotation in the azimuth plane and a non-linear worm-gear-plus-lever transmission for rotation in the elevation plane. The azimuth calibration is simply finding the offset constant from the reference position due to installation and rotor errors. Once found, the offset constant may simply be inserted in the corresponding EGIS control unit EPS-103.

The non-linear elevation transmission of the EGIS rotor EPR-203 is much more tricky. The look-up table correction built in the EPS-103 control unit was found rather inaccurate. Adjusting the remaining elevation offset constant did not solve the problem. A working solution was to derive our own elevation-correction table in 5-degree steps using a gravity inclinometer as shown on Figure 14.

Finally, linear interpolation between two neighbor correction-table points is implemented in the Python code controlling the antenna positioner.



**Figure 14:** Using the inclinometer.

The inclinometer is further used to correct small installation errors. The supporting mast of the antenna was found to deviate as much as one degree from vertical. Rather than performing mechanical adjustments on the antenna and/or its support structure, such small errors are easily corrected in Python code as vector rotations.

The final check of the antenna/rotor alignment is tracking the Sun. The position of the latter can be computed precisely at any time. The Sun is the strongest natural source of radio waves in the sky. Of course the Sun can be tracked optically, for example by checking the position of the feed shade on the parabolic reflector. Using rotational-symmetric parabolic reflectors, the feed shade should fall exactly in the center of the dish as shown on Figure 15.



**Figure 15:** Checking the feed shade.

#### 3.2 System noise temperature

A very important parameter of any satellite-receiving station and/or radio telescope is the system noise temperature. The latter describes the amount of noise added by the station hardware to the received signal.

The simplest procedure to measure the system noise temperature is to turn the antenna into two different targets radiating as black bodies at well known temperatures. The described hot/cold method yields the hot/cold power ratio:

$$Y = \frac{P_{HOT}}{P_{COLD}} = \frac{B \cdot k_B (T_{HOT} + T_S)}{B \cdot k_B (T_{COLD} + T_S)} = \frac{T_{HOT} + T_S}{T_{COLD} + T_S} \quad (3)$$

Both the receiver bandwidth  $B$  and the Boltzmann constant  $k_B \approx 1.38 \cdot 10^{-23} \text{J/K}$  cancel out in the hot/cold ratio. The radio-telescope antenna is first pointed to a cold part of the sky assuming  $T_{COLD} \approx 10\text{K}$ . The antenna is afterwards pointed to a forest (good microwave absorber if dry) assuming  $T_{HOT} \approx 290\text{K}$ . The described radio-telescope with the VE4MA feed achieved a hot/cold ratio  $Y \approx 7\text{dB} \approx 5$ . The measured system noise temperature is:

$$T_S = \frac{T_{HOT} - Y \cdot T_{COLD}}{Y - 1} = \frac{290\text{K} - 5 \cdot 10\text{K}}{5 - 1} = 60\text{K} \quad (4)$$

It is estimated that these 60K include about 32K coming from the LNA, about 3K coming from the remaining stages of indoor signal processing and about 25K from the antenna side lobes observing the warm Earth. Such a low antenna noise temperature of just 25K is an excellent result for the VE4MA feed and a relatively small  $d \approx 20 \lambda$  parabolic dish obstructed by the feed itself and its four metal supporting struts.

For comparison, the same measurement was also performed with the a simple waveguide- horn feed by removing the Kumar choke from the VE4MA feed. A hot/cold ratio of only  $Y \approx 5\text{dB} \approx 3.16$  was obtained in the latter case. The corresponding measured system noise temperature doubled to  $T_S \approx 120\text{K}$  therefore halving the sensitivity of the radio telescope! Removing the Kumar choke therefore increases the antenna temperature up to 85K due to the much larger side lobes of a simple waveguide horn.

### 3.3 Antenna illumination efficiency

Yet another important parameter to check is the antenna aperture-illumination efficiency. The latter may be impaired both due to an incorrect illumination (usually under-illumination) and/or due to mechanical defects of the parabolic-reflector surface. Neither can be detected with distributed sources like those used in the system-noise-temperature measurement described in the previous chapter.

A calibrated point source of radiation is required to measure the antenna aperture illumination efficiency.

The Sun is a strong natural radio source. The Sun is small enough to be considered a point source since its angular diameter  $\alpha_{SUN} \approx 0.5^\circ \ll \alpha \approx 4.7^\circ$  is much smaller than the resolution of the described radio telescope. Unfortunately the radio radiation from the Sun is changing with the Sun activity. Changes are different at different frequencies.

Fortunately for our measurement the activity of the Sun is monitored by several observatories around the world on many different frequencies. This data is regularly published on the internet [8]. In our case the most useful observation is at  $f_0 = 1415\text{MHz}$  and the most useful observatory is located in San Vito dei Normanni near Brindisi in Italy. The latter provides Sun data close to our local noon with the Sun high on the sky.

During our measurement San Vito reported a solar-flux spectral density of  $S/B = 69\text{SFU} = 69 \cdot 10^{-22} \text{W/m}^2/\text{Hz}$  at  $f_0 = 1415\text{MHz}$ . At the same time we measured a hot/cold ratio of  $Y \approx 13.5\text{dB} \approx 22.4$  while pointing the radio telescope both to the Sun and to a cold part of the sky. Considering that our antenna only receives half of the reported radiation on one polarization and that the cold sky radiates at  $T_{COLD} \approx 10\text{K}$  we obtain the effective area of our antenna as:

$$A_{eff} = \frac{2 \cdot k_B (Y - 1) \cdot (T_S + T_{COLD})}{S / B} \approx \frac{2 \cdot 1.38 \cdot 10^{-23} \text{W} / \text{Hz} / \text{K} \cdot (22.4 - 1) \cdot (60\text{K} + 10\text{K})}{6.9 \cdot 10^{-21} \text{W} / \text{m}^2 / \text{Hz}} \approx 5.99\text{m}^2 \quad (5)$$

Dividing the effective area with the physical area of our 3.1m parabolic dish we estimate the illumination efficiency as:

$$\eta = \frac{A_{eff}}{\pi (d / 2)^2} \approx \frac{5.99\text{m}^2}{\pi (3.1\text{m} / 2)^2} \approx 0.79 \quad (6)$$

An aperture illumination efficiency of 79% is an excellent result for a relatively small  $d \approx 20 \lambda$  parabolic dish obstructed by the VE4MA feed and its four metal supporting struts. This result also proves that the performance of our parabolic dish is not affected by mechanical distortions, at least at the given wavelength of  $\lambda = 21\text{cm}$ .

### 3.4 Radio-interference mitigation

An amateur radio-telescope builder usually has little if any choice to select the place where to place his instrument. Wind is a primary concern for a large antenna. Snow and ice loading may also be important factors.



While winds and precipitations have been observed and measured for many years, radio interference is a big unknown in a constantly changing world of electromagnetic pollution of any kind.

Traditional amateur astronomers usually prefer remote places to avoid optical pollution. Such places may have high winds and receive lots of precipitations in winter. An amateur radio telescope likely has to be placed in an urban environment where meteorological constraints are less severe. The level of radio interference in an urban environment may span over several orders of magnitude. Therefore at least some rough interference measurements are recommended in site before building such an instrument.

In our case the radio telescope is placed in a suburb of a town in a closed valley protected from winds. Interestingly, no radio interference from radio transmitters was found in the 1.42GHz protected astronomy band. The nearest radio transmission was found at about 1436MHz outside the protected band. It looks like certified radio transmitters are shielded and filtered enough not to cause harmful radio interference. As a precaution, a radio-frequency spectrum analyzer covering a 50MHz wide span around 1.42GHz is always connected to the radio telescope to check for interference as shown on Figure 16.

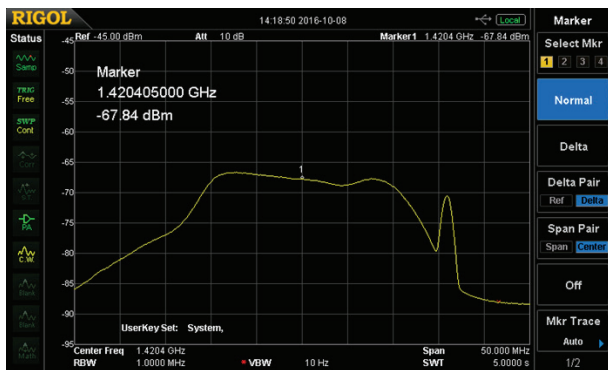


**Figure 16:** Pass-band around 1420.4MHz and interference at 1436MHz.

On the other hand, different kinds of radio interference were experienced from electronic and electrical equipment not intended to transmit any radio frequency at all. Live-video IP cameras from different manufacturers, cheap and expensive products alike, were identified as the worst source of radio interference, radiating harmonics of all clocks used by their internal digital circuits. Unlike suggested in many articles and websites, video IP cameras can not be used to help aiming the antenna of a radio telescope!

Most electronic equipment containing digital circuits causes narrow-band interference around 1420.000MHz

+/- tolerances of their internal crystal oscillator. This interference may be a high-order harmonic of an internal clock operating at 10.000MHz or 20.000MHz. A simple countermeasure is to move all computers and network devices at least two concrete floors below the radio-telescope antenna. Such unintentional interference also decays quickly with distance. Of course all unnecessary electronic equipment may simply be switched off when the radio telescope is operating...

Finally, we could not identify the source of some kind of wide-band interference that appears periodically. It may be coming from a spark-ignition system, most likely natural-gas heater, since its occurrence and period was found correlated with low outside temperatures. It should be noted that both narrow-band and wide-band low level interference could only be detected using software- defined-radio (SDR) techniques and very long integration times.

## 4 Hydrogen spectrum measurements

### 4.1 Spectrum analyzer

Our first experiments were performed with a conventional, scanning-receiver type spectrum analyzer Rigol DSA-815. Such an instrument has a better dynamic range than its all-digital FFT- based counterparts. On the other hand, a scanning receiver uses the incoming signal rather inefficiently. Most of the signal energy is lost while the scanning receiver dwells on other frequencies.

In the case of radio astronomy, the signal-to-noise ratio is low. The signal coming from celestial sources is random just like thermal noise. Measuring the average power  $\langle P \rangle$  of random signals requires lots of averaging. The fluctuation (intended as standard deviation) of the result  $\Delta P$  only decreases with the square root of the number of measurements  $N$  according to the Dicke equation [9]:

$$\frac{\Delta P}{\langle P \rangle} = \frac{1}{\sqrt{N}} = \frac{1}{\sqrt{B \cdot \tau}} = \sqrt{\frac{B_{VIDEO}}{B}} = \frac{\Delta T}{\langle T \rangle} \tag{7}$$

In the case of a radio receiver, the number of independent measurements  $N = B \cdot \tau$  is the product of the receiver bandwidth and measurement time. Most scanning-receiver type spectrum analyzers have built-in averaging in the form of a low-pass video filter with a cutoff frequency  $B_{VIDEO} \ll B$  much smaller than their resolution bandwidth.

To observe the neutral-hydrogen radiation at  $\lambda = 21\text{cm}$  a sensible setting is a resolution bandwidth of  $B = 10\text{kHz}$ .

Setting the video bandwidth to  $B_{VIDEO}=10\text{Hz}$  is equivalent to an averaging factor of  $N=1000$ . The fluctuation of the result is thus reduced by a factor of  $\sqrt{1000}\approx 31.6$ . The typical  $\sim 10\text{dB}$  noise “grass” of a spectrum analyzer is reduced to  $\sim 0.3\text{dB}$ . Considering the noise sources in our radio telescope  $T=T_{SKY}+T_S\approx 10\text{K}+60\text{K}=70\text{K}$ , the standard deviation  $\Delta T=\langle T \rangle/\sqrt{N}=2.2\text{K}$  is a good estimate for the minimum observable signal coming from celestial sources.

Unfortunately such a measurement becomes very slow due to the inefficient use of the incoming signal energy by a scanning receiver. Observing the hydrogen frequency band of our Milky Way galaxy requires scanning a band of  $\Delta f=2\text{MHz}$ . A single observation requires 20s although only 100ms are effectively used:

$$t = \frac{\tau \cdot \Delta f}{B} = \frac{\Delta f}{B_{VIDEO} \cdot B} = 20\text{s} \quad \tau = \frac{1}{B_{VIDEO}} = 100\text{ms} \quad (8)$$

On the other hand, if the same measurement is performed with a FFT spectrum analyzer, the latter making full use of the incoming signal energy, the observation time reduces to  $t = \tau = 1/B_{VIDEO} = 100\text{ms}$ .

Considering the rotation of the Earth and the beam width of the antenna used, a correction of the antenna direction is required about once per minute to track a selected deep-space radio source. A simple Python script “zvezdar.py” transforms the requested right ascension (celestial longitude) and declination (celestial latitude) into azimuth and elevation for a particular location of the observer. Corrections for mechanical imperfections of the antenna rotor EPR-203 are included. Since its corresponding control unit EPS-103 only allows one command at a time, elevation and azimuth commands are sent by the Python script alternatively every 25 seconds through an RS-232 interface at 9600bps.

#### 4.2 Sample measured spectra

A radio telescope for the neutral-hydrogen line does not see much radiation coming from dense, optically bright stars, but the radiation from sparse, lone hydrogen atoms. In the direction of the star Deneb (constellation Cygnus) three (outer) arms of our Milky Way galaxy can be seen due to their different Doppler shifts. Our Solar system is approaching all three (outer) arms (positive Doppler shift) at different relative velocities as shown on Figure 17.

The equivalent black-body brightness temperature of a hydrogen cloud  $T(f)=T_{HOT}-T_{COLD}$  can be calculated by reversing equation (3) to obtain  $T_{HOT}$  from known values of  $T_{COLD}$  and  $T_S$  as well as the measured ratio  $Y(f)$  with the

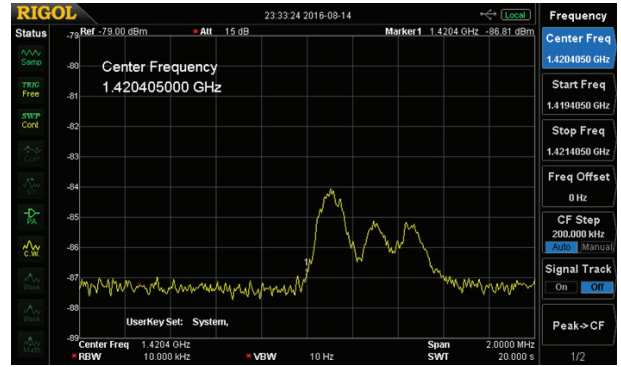


Figure 17: Neutral-hydrogen spectrum from the direction of the star Deneb.

spectrum analyzer. In particular, the measured ratios on Figure 17 are about  $Y(f)\approx 3\text{dB}$  for the first arm of the Milky Way and about  $Y(f)\approx 2\text{dB}$  for the second and third arm.

On the other hand, the central part of our Milky Way galaxy is much denser resulting in a continuous neutral-hydrogen spectrum. Individual (inner) arms can hardly be resolved. Due to the rotation of our galaxy, the region in the direction of the constellation Scutum is moving away from our Solar system resulting in a negative Doppler shift as shown on Figure 18.

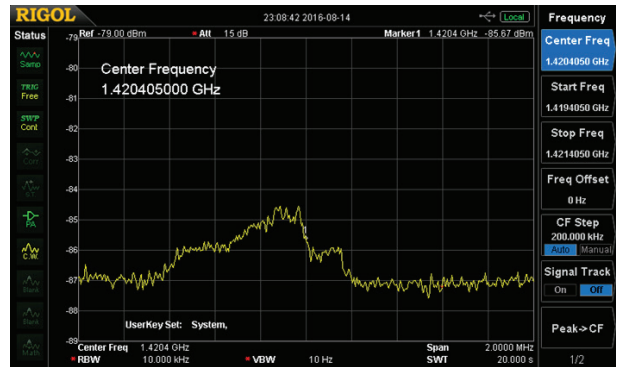


Figure 18: Neutral-hydrogen spectrum from the direction of the star  $\alpha$  Scutum.

#### 4.3 Measured hydrogen column density

Integrating the neutral-hydrogen power spectrum represented as the equivalent black-body brightness temperature  $T(f)$ , the total column density of neutral-hydrogen atoms can be derived:

$$\eta_H = \frac{8\pi \cdot k_B \cdot \tau_{1/2}}{h \cdot c \cdot \lambda \cdot \ln 2} \cdot \int_{f_{MIN}}^{f_{MAX}} T(f) df \quad (9)$$

Inserting the physical constants in the above equation: the Boltzmann constant  $k_B \approx 1.38 \cdot 10^{-23} \text{ J/K}$ , the Planck constant  $h \approx 6.63 \cdot 10^{-34} \text{ Js}$ , the speed of light  $c_0 \approx 3 \cdot 10^8 \text{ m/s}$ ,

the excited neutral-hydrogen half life  $\tau_{1/2} \approx 3.3 \cdot 10^{14} \text{s}$  (~11 million years), the wavelength  $\lambda = 21 \text{cm}$  and referring the observed equivalent black-body brightness temperature  $T(v)$  to the relative velocity in place of frequency  $T(f)$ , the above equation can be simplified into [10]:

$$\eta_H = 1.82 \cdot 10^{18} \cdot \frac{\text{atoms}}{\text{cm}^2} \cdot \int_{v_{MIN}}^{v_{MAX}} \frac{T(v)}{K} \cdot \frac{dv}{\text{km/s}} \quad (10)$$

Figure 19 shows the equivalent black-body brightness temperature  $T(v)$  as a function of velocity calculated from the observed frequency spectrum in the direction of the star Deneb.

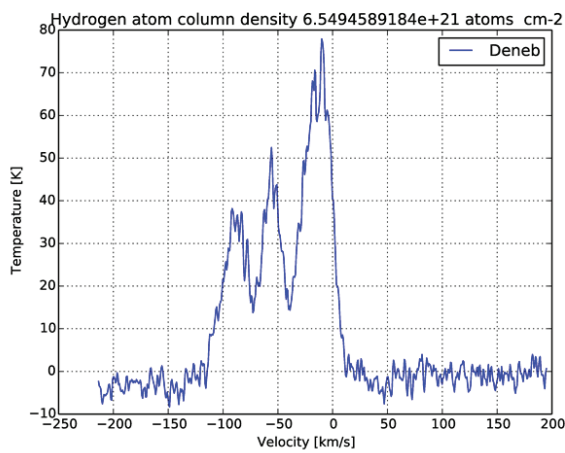


**Figure 19:** Neutral-hydrogen velocity and column density.

The integrated hydrogen-atom column density is about  $\eta_H \approx 6.6 \cdot 10^{21} \text{ atoms/cm}^2$  spread over a distance of approximately  $35000 \text{ light-years} \approx 3.3 \cdot 10^{20} \text{ m} = 3.3 \cdot 10^{22} \text{ cm}$ . The average hydrogen density in the interstellar space is therefore very low, just  $N \approx 0.2 \text{ atoms/cm}^3 = 2 \cdot 10^5 \text{ atoms/m}^3$  or very good vacuum indeed...

## 5 Hydrogen mapping of our galaxy

### 5.1 Software signal processing

Radio astronomy and in particular interferometry were one of the first large-scale applications of digital-signal processing. The reason is very simple: the signal-to-noise ratio in radio astronomy is always low. Therefore just a few bits of resolution are required to adequately represent and process the signals, simplifying the hardware.

Rather than using exotic hardware in the described radio telescope, an inexpensive DVB-T USB dongle based on the RTL2832U chip was used for frequency down conversion and A/D conversion. Besides a dedi-

cated DVB-T demodulator, the RTL2832U chip includes a straightforward 8-bit A/D converter for analog radio reception. The latter is well supported both with drivers, application software and development tools in all known operating systems on personal computers. The A/D converter can process signal bandwidths up to  $B \approx 2.4 \text{MHz}$ . The latter is more than sufficient to observe the neutral-hydrogen spectrum of our Milky Way galaxy.

The RTL2832U chip is frequently coupled with the R820T2 tuner (down converter) chip. Although the latter is only specified up to  $f_{MAX} \geq 1 \text{GHz}$ , most chips exceed  $f_{MAX} \geq 1.7 \text{GHz}$  at room temperature. The R820T2+RTL2832U combination therefore allows direct processing of the amplified and filtered 1.42GHz hydrogen-line signal provided that the tuner chip R820T2 is kept at a constant room temperature. An improved version of the DVB-T dongle is used in our radio telescope featuring a TCXO frequency reference in an aluminum case. The latter provides both shielding and cooling of all internal components as shown on Figure 20.

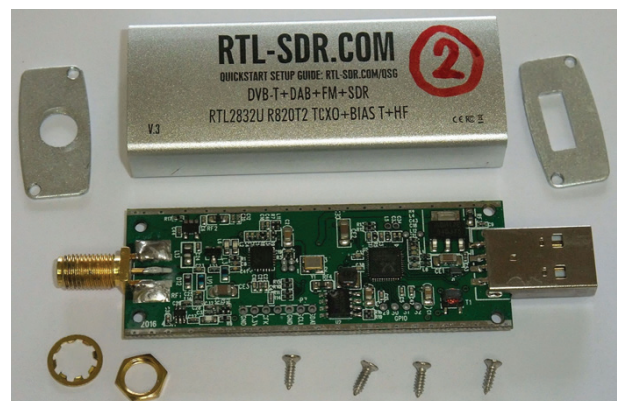


**Figure 20:** Inexpensive SDR front-end.

Although excellent open-source development tools exist for the R820T2+RTL2832U combination, ready-made software was tried first with excellent results. In particular we successfully experimented the freeware “HSDR version 2.76” [11] running on “WindowsXP”. The DVB-T dongle requires its own low-level USB driver “zadig\_xp.exe” and the corresponding interface “ExtIO\_RTL2832.dll” to HSDR. The main advantage of HSDR over other similar software is the ability to use large averaging factors and display small amplitude differences, both of them very necessary for radio astronomy.

We only used the radio-frequency FFT spectrum analyzer included besides several other receiver functions in HSDR. A center frequency of  $f_0 = 1420.405 \text{MHz}$  and an observation span of  $\Delta f = 1.44 \text{MHz}$  are good choices for hydrogen-line observations of our Milky way galaxy. The optimum FFT size was found experimentally



as  $2^{14} = 16384$  to separate easily hydrogen spectra from narrow-band interference.

The spectrum is first averaged by a factor of 2048 inside HSDR. The averaged spectrum is displayed on a 1280-pixel wide LCD screen, therefore 16384 spectrum lines are further averaged by a factor of about 13 to 1280 display columns. All this averaging reduces the power (temperature) fluctuations to approximately  $10\text{dB} / \sqrt{2048 \cdot 13} \approx 0.06\text{dB}$ .

The “HSDR” software can display the averaged spectrum plot as a function of frequency or as a spectrum waterfall with different colors indicating signal intensity. Further, the waterfall can be made slow enough to allow mechanical scanning of the sky and its color scale can be selected to show intensity changes of less than 0.5dB. One of the first experiments with “HSDR” running independently on two personal computers showing 2D images (galactic longitude and relative velocity) of our Milky Way galaxy is shown on Figure 21.



**Figure 21:** Waterfall display with HSDR software.

The A/D converter inside the RTL2832U chip includes an analog anti-aliasing filter on its input. The latter has a ripple of about  $\pm 0.5\text{dB}$  over the central three quarters of the observed frequency span and rolls off sharply (about  $-3\text{dB}$ ) at both span edges. This is an excellent result for an analog filter and in most applications goes unnoticed. On the other hand, radio astronomy requires measuring very small differences of signal levels. Unfortunately the current version of the HSDR free-ware does not include a normalization of the response nor other countermeasures to correct the above-mentioned pass-band ripple.

## 5.2 Galactic-plane scanning

One of the most important historical discoveries of hydrogen-line observations is that our Milky Way is a spiral galaxy. The plane of the Milky Way is currently inclined by  $62.8^\circ$  with respect to the equatorial plane. This inclination is slowly increasing due to the precession of the

Earth’s rotation axis. Most of the hydrogen-line radiation comes from the plane of our galaxy. Hydrogen-line radiation from other directions is much weaker. Therefore the plane of the Milky Way is the target of choice to begin with hydrogen-line observations.

The whole galactic plane is not visible from our latitude  $46^\circ$  north. Considering the beam width of a 3.1m-diameter antenna at 1.42GHz, celestial objects can only be observed at elevations larger than  $EL \geq 10^\circ$  above the local horizon to avoid thermal noise radiated by the warm ground. In our case we were lucky enough not to have any obstacles nor interference sources in the direction south where the most difficult-to-see celestial objects appear at particular times during the day.

Galactic coordinates, galactic longitude and galactic latitude, are the coordinates of choice for hydrogen-line observations. The galactic plane of our Milky Way galaxy is by definition galactic latitude zero  $GLAT = 0$ . Galactic longitude zero  $GLON = 0$  is defined by radio observations as the radio source Sagittarius A\*, supposed to be a super-massive black hole in the center of our galaxy. Galactic longitude increases in the opposite direction of the rotation of our galaxy. The angular velocities of different parts of our galaxy are different resulting in Doppler shifts.

Our scanning of the galactic plane is explained using the artist’s impression of the Milky Way [12]. Sagittarius A has a declination of about  $\delta \approx -29^\circ$ , therefore it reaches a elevation of just  $15^\circ$  above the southern horizon at our latitude  $46^\circ$  north. It therefore makes sense to start the galactic-plane scanning just before Sagittarius A at a galactic longitude of about  $GLON = -10^\circ$ . The observed galactic longitude is then increased at a carefully selected rate for about 12 hours to end our scanning around galactic longitude  $GLON = 265^\circ$  as shown on Figure 22:

In this way the whole visible galactic arc is observed during one single scan with plenty of time for data averaging. Considering the rotation of the Earth such a scan both starts and ends at the southern horizon. The direction of the scan is important. Scanning by increasing the galactic longitude the galactic equator appears high above the local horizon at our latitude  $46^\circ$  north. On the other hand, scanning in the opposite direction, decreasing the galactic longitude from  $GLON = 265^\circ$  to  $GLON = -10^\circ$ , the galactic equator appears rather low above our northern horizon. Unfortunately local obstructions at our micro location preclude such scanning. Besides steering the antenna positioner to scan the galactic plane, the Python script “mlekar.py” also records the times and corresponding galactic longitudes and latitudes in a text file. On the



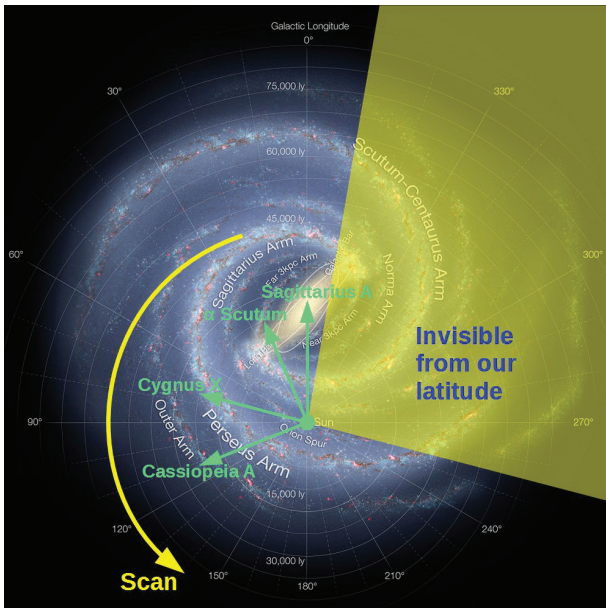


**Figure 22:** Galactic-plane scanning from our latitude.

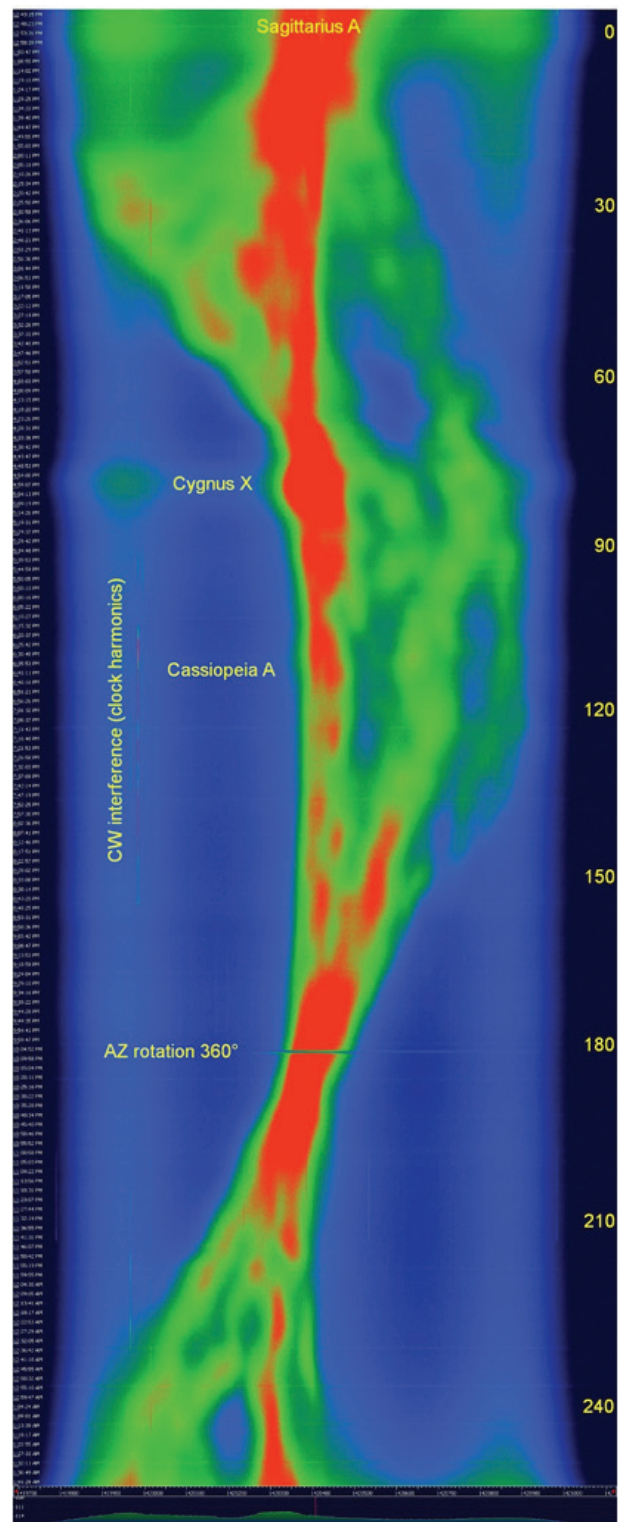
other hand, the “HSDR” software puts time tags on the waterfall display. By combining both, the waterfall can be referenced to the galactic longitude. Since the computer screen is not high enough, periodic screen-shots are taken with the “Chronolapse” software and the final result is stitched together with the “IrfanView” image-processing software as shown on Figure 23.

Figure 23 shows unprocessed and uncorrected data. Besides the hydrogen spectrum, continuum (broadband) celestial sources are also visible as wide horizontal features like the center of our galaxy (always well visible), the star-forming region Cygnus X or the supernova remnant Cassiopeia A (barely visible on some scans).

Some artifacts are caused by the pass-band ripple of the analog anti-aliasing filter of our receiver. Ground thermal noise is visible at the beginning and at the end of the scan. Narrow-band CW interference (clock harmonics from digital equipment) is visible as narrow spectral lines around 1420.000MHz. Periodic wide-band interference (likely spark ignition) is visible towards the end of the scan. The interruption at galactic longitude 180° is due to our programming mistake of the rotor control unit EPS-103 causing a 360° rotation of our antenna.

### 5.3 3D map of the Milky way

Performing several galactic-longitude scans at different galactic latitudes, a 3D map of our galaxy can be built. Considering the beam width of our antenna, separate scans were made in 5° galactic-latitude steps. A map composed of five such scans at galactic latitudes of -10°, -5°, 0°, +5° and +10° is shown on Figure 24.



**Figure 23:** Waterfall display with HSDR software.

Observing southern galactic latitudes becomes increasingly more difficult from the northern hemisphere. Missing data at galactic latitude -10° (south) had to be replaced with a gray bar at the beginning of the scan. On the other hand, the time of year of the galactic-longitude

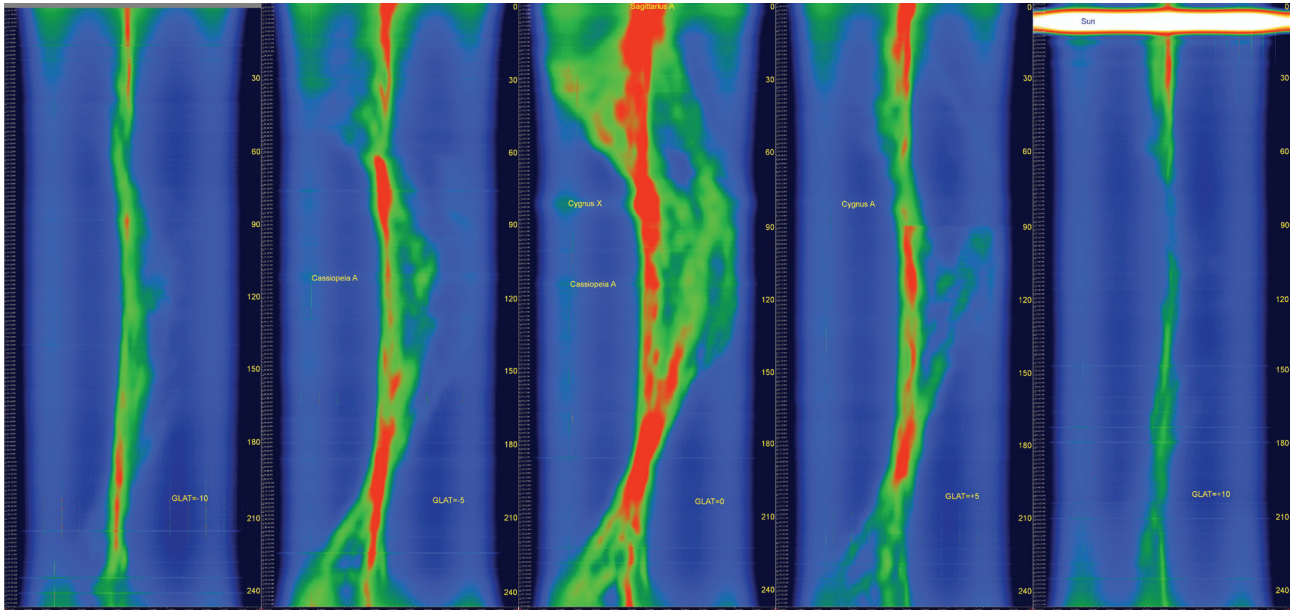


**Figure 24:** Measured 3D map of the Milky Way.

gitude scan at galactic latitude  $+10^\circ$  (north) was intentionally selected to cross the Sun.

The most interesting scan is in the galactic plane (galactic latitude  $0^\circ$ ) showing even distant arms of our galaxy with large Doppler shifts of the hydrogen line. Moving away from the galactic plane either south or north the amount of visible hydrogen decreases. Even more important, moving away from the galactic plane only local hydrogen with a relatively small Doppler shift remains visible.

## 6 Conclusion

In order to understand the difficulties in operating a radio telescope, it is fair to compare its performance a well-known device like a GSM phone operating in the nearby 1.8GHz frequency band. Both the hydrogen line of a single galactic arm and the GSM signal have a similar bandwidth of about  $B \approx 200\text{kHz}$ . While the GSM phone requires a signal with the equivalent black-body brightness temperature of  $T_{\text{GSM}} \approx 30000\text{K}$ , the arms of our galaxy on average reach  $T_{\text{GALAXY}} \approx 30\text{K}$ . GSM signals are therefore stronger by a factor of  $1000=30\text{dB}$  than hydrogen- line signals.

The presented compact radio telescope has an antenna with an effective area about  $10000=40\text{dB}$  times larger than a GSM phone. Large professional radio telescopes have effective areas about  $1000=30\text{dB}$  times larger than our radio telescope. In total, our compact radio telescope is about  $70\text{dB}$  more sensitive than a GSM

phone and about  $30\text{dB}$  less sensitive than a large professional radio telescope.

Nevertheless we were able to obtain a 3D map, intensity versus galactic longitude, galactic latitude and Doppler shift of our Milky Way galaxy with our compact radio telescope. Such a 3D map lead to the discovery of the spiral structure of our galaxy some 60 years ago using much larger instruments. A further limitation of our compact radio telescope is its location at  $46^\circ$  northern latitude while the most interesting features of our galaxy and neighbor celestial objects are located in the southern sky.

Our results were obtained using signal-processing software that was not originally designed for radio-astronomical observations. Much improvement could be obtained by writing or own code to allow response normalization, arbitrary averaging factors and known radio-interference rejection. In this was the hydrogen spectra of less bright celestial objects could be observed like the Andromeda galaxy as well as many continuum sources like some of the strongest pulsars. Of course, the most ambitious goal are radio interferometers with arbitrary baselines including several similar compact radio telescopes, synchronized using GNSS (global satellite navigation systems) and linked via internet.

## 7 References

1. Grote Reber: "Galactic Radio Waves", *Sky and Telescope*, Vol.8, No.6, April, 1949.
2. Mal Wilkinson, John Kennwell: "Hydrogen-line observations of the Galaxy and the Magellanic Clouds", *Australian Journal of Astronomy*, Vol.5, No.4, pp 121-133, 1994.
3. Jean-Jacques Maintoux: "Radioastronomie", [http://f1ehn.pagesperso-orange.fr/fr/f\\_radioastro.htm](http://f1ehn.pagesperso-orange.fr/fr/f_radioastro.htm)
4. Nguyen Van Hiep, Pham Tuan Anh, Pham Ngoc Diep, Pham Ngoc Dong, Do Thi Hoai, Pham Thi Tuyet Nhung, Nguyen Thi Thao, Pierre Darriulat: "The VATLY Radio Telescope", *Communications in Physics*, Vol.22, No.4, pp 365-374, 2012.
5. A. Kumar, "Reduce Cross-Polarization in Reflector-Type Antennas," *Microwaves*, pp 48-51, March 1978.
6. B.W. Malowanchuk, VE4MA, "Use of Small TVRO Dishes for EME," *Proceedings of the 21<sup>st</sup> Conference of the Central States VHF Society, ARRL*, pp 68-77, 1987.
7. Matjaž Vidmar: "Ein sehr rauscharmer Antennenverstärker fuer das L-band", pp 163-169, *UKW Berichte*, 3/1991, or "A Very Low Noise Aerial Amplifier", pp 90-96, *VHF Communications*, 1992/2.
8. Solar Radio Data, U.S. Dept. of Commerce, NOAA, Space Weather Prediction Center, [http://legacy-www.swpc.noaa.gov/ftpdir/lists/radio/7day\\_rad.txt](http://legacy-www.swpc.noaa.gov/ftpdir/lists/radio/7day_rad.txt)
9. Robert H. Dicke: "The Measurement of Thermal Radiation at Microwave Frequencies.", *The Review of Scientific Instruments*, Vol.17, No.7, pp 268-275, 1946.
10. James J. Condon, Scott M. Ransom, NRAO: "The HI 21 cm Line", <http://www.cv.nrao.edu/course/astr534/HILine.html>
11. High Definition Software Defined Radio, <http://www.hdsdr.de/> [12] Artist's impression of the Milky Way (updated - annotated), [https://commons.wikimedia.org/wiki/File:Artist's\\_impression\\_of\\_the\\_Milky\\_Way\\_\(updated\\_annotated\).jpg](https://commons.wikimedia.org/wiki/File:Artist's_impression_of_the_Milky_Way_(updated_annotated).jpg)

Arrived: 13. 03.2017

Accepted: 01. 08. 2017

# Highly Efficient Photocatalytic Activity in the Visible Region of Hydrothermally Synthesized N-doped TiO<sub>2</sub>

Maja Lešnik<sup>1</sup>, Dejan Verhovšek<sup>1</sup>, Nika Veronovski<sup>1</sup>, Srđan Gatarić<sup>1</sup>, Mihael Drofenik<sup>2</sup>, Janez Kovač<sup>3</sup>

<sup>1</sup>Cinkarna Celje, d.d. Inc., Celje, Slovenia

<sup>2</sup>University of Maribor, Faculty of Chemistry and Chemical Engineering, Maribor, Slovenia

<sup>3</sup>Jozef Stefan Institute, Department of Surface Engineering and Optoelectronics, Ljubljana, Slovenia

**Abstract:** Nanocrystalline rutile titanium dioxide (TiO<sub>2</sub>) samples doped with various amounts of nitrogen (N) atoms were prepared using a hydrothermal synthesis route and a polycrystalline TiO<sub>2</sub> precursor. The doped rutile nanocrystallites were analysed with transmission electron microscopy (TEM), X-ray photoelectron spectroscopy (XPS) and UV-Vis spectroscopy. The Kubelka-Munk band-gap calculation were used to examine the UV-Vis reflectance spectra. The measurements of the photocatalytic activity were performed utilizing FT-IR. A remarkable increase in the photocatalytic activity of the doped rutile nanocrystallites was detected, when applying the isopropanol degradation method with UV-Vis light irradiation.

**Keywords:** Nanoparticles, TiO<sub>2</sub>, Rutile, Visible photocatalyst

## Hidrotermalno sintentiziran TiO<sub>2</sub> dopiran z N z visoko fotokatalitsko aktivnostjo v vidnem delu svetlobnega spektra

**Izleček:** Z uporabo hidrotermalne sinteze in polikristalinične rutilne oblike nanodelcev TiO<sub>2</sub> smo pripravili monokristalinične rutilne delce, dopirane z različnimi koncentracijami dopanta N. Za analizo dopiranih rutilnih TiO<sub>2</sub> nanodelcev smo uporabili elektronsko mikroskopijo (TEM), fotoelektronsko spektroskopijo (XPS), rentgensko praškovo difrakcijo (XRD), UV-VIS spektroskopijo in kalkulacijo energijskih vrzeli s Kubelka Munk. Pri merjenju fotokatalitske aktivnosti z metodo degradacije izporopropanola v alkohol smo ugotovili, da dopiranje rutilnega TiO<sub>2</sub> z N povzroči izrazit premik delovanja fotokatalitske aktivnosti na vidni svetlobi svetlobnega spektra.

**Ključne besede:** Nanodelci, TiO<sub>2</sub>, rutil, vidni fotokatalizator

\* Corresponding Author's e-mail: maja.lesnik@cinkarna.si

### 1 Introduction

Nanocrystalline titanium dioxide (TiO<sub>2</sub>) is the most widely investigated n-type semiconductor due to its high photocatalytic activity under UV light, which is important for numerous outdoor applications, such as wastewater treatment, air purification and self-cleaning applications (walls, concretes). [1-8] Recently, new insights have been presented in the development of TiO<sub>2</sub> photocatalysts that could efficiently utilize not

only the UV light but also the visible light in the solar spectrum and could therefore be appropriate for interior photochemical applications. [8-16] Chemical modifications of the TiO<sub>2</sub> crystal lattice achieved by doping with cations or anions appear to be the most promising approach to enhance the visible-light absorption power. [17]



The dopants can be interstitially or substitutionally incorporated into the  $\text{TiO}_2$  crystal lattice. Different concentration levels of these dopants might influence the new electronic states localized in the gap or the electronic band edge narrowing, leading to an increase in the visible-light absorption efficiency. [14, 17] However, it is well known that the photocatalytic activity under exposure to visible light, associated with the mobility of the excited electrons and holes and their recombination rate, differs, depending on the dopant type, its concentration and the lattice position that it occupies. [14, 17] On the other hand, anion doping has a tremendous effect on visible-light photocatalytically active  $\text{TiO}_2$ . [18, 19] Among all the attempts at non-metal doping in  $\text{TiO}_2$ , nitrogen doping has shown the greatest promise for achieving visible-light active photocatalysts. The incorporation of nitrogen into the  $\text{TiO}_2$  crystal lattice is advantageous, due to it having a similar atomic radius to oxygen and a lower electronegativity than oxygen. [20] The modification mechanism of N-doped  $\text{TiO}_2$ , its ability to absorb visible light and visible-light photocatalysis is still under investigation. There are three different hypotheses that could explain the phenomena. Firstly, in N-doped  $\text{TiO}_2$  the energies of the N 2p and O 2p states are similar. The consequence of this is band-gap narrowing and the ability to absorb visible light. [22] Secondly, oxygen sites are substituted by nitrogen atoms and the intermediate energy level is formed below the conductive band edge. [21] Thirdly, doping with nitrogen forms oxygen-vacancy defect sites, which are the major factor in visible-light photocatalytic activity. [23, 24] Rutile, as an n-type  $\text{TiO}_2$  semiconductor, exhibits oxygen vacancies on the surface. Nitrogen doping introduces additional oxygen vacancies, which leads to an even more efficient photocatalytic activity. [25]

It is well known that the absorption properties of N-doped anatase and raw rutile  $\text{TiO}_2$  are distinguishable. The structures of anatase and rutile differ in the position of the octahedron, resulting in a tetragonal structure for both modifications. [3] The other reason for the different absorption is the electron density of the N-doped anatase or rutile. [26] Doping with nitrogen provides N 2p states located above the O 2p valence band. Since rutile has a smaller band gap than anatase, this furthermore enhances the valence band. [27] The same findings were confirmed by Yang and co-authors in their DFT calculations on nitrogen-doped structures of rutile crystals. [15] Liu, in his work, demonstrated that nitrogen-doped  $\text{TiO}_2$  with more rutile phase has more defects than the nitrogen-doped  $\text{TiO}_2$  with less rutile phase, which enhances the photocatalytic efficiency. [25] The photocatalytic efficiencies of rutile and anatase are related to the formation of hydroxyl radicals that prevent electron-hole recombination during

exposure to sunlight. Some studies have demonstrated that the rutile crystal phase exhibits enough hydroxyl groups, which are believed to act as light photocatalysts, i.e., to accept the holes generated by UV illumination and form hydroxyl radicals and thus prevent electron-hole recombination. [28, 29]

The selection of nitrogen doping for the rutile crystal structure was based on theoretical studies published recently in the open literature, particularly on the numerous advantages of visible-light absorption and enhanced photocatalytic activity. [26-29]

In the present study we report a new synthesis procedure of N- $\text{TiO}_2$  visible-light photocatalyst based on the hydrothermal synthesis using the polycrystalline rutile  $\text{TiO}_2$  nanocrystallites.

## 2 Experimental

### 2.1 Preparation method

The hydrothermal synthesis of N-doped rutile  $\text{TiO}_2$  nanocrystallites was performed in a Teflon-lined, stainless-steel autoclave with a volume of 80 mL. To prepare the  $\text{TiO}_2$ -doped sample the reactor was loaded with a 50-mL aqueous suspension of polycrystalline rutile  $\text{TiO}_2$  nanocrystallites provided by Cinkarna Celje, Inc., having a mass concentration between 60-150 g/L (calculated as  $\text{TiO}_2$ ) and 1 mass % (based on  $\text{TiO}_2$  content) of urea ( $(\text{NH}_2)_2\text{CO}$ , 99% w/w, Merck). The mixture of polycrystalline rutile  $\text{TiO}_2$  nanocrystallites and dopant was then stirred for at least 15 minutes. The autoclave was put into a preheated oven and was hydrothermal treated at 180 °C for 24 hours. At the end of the heating process the autoclave was taken out of the oven and left to cool to room temperature. The as-prepared product was diluted with distilled water, washed on a laboratory centrifuge (MPW 350 – Med. Instruments, High brushless centrifuge, 4000 rpm, 20 minutes). The washing was continued until the conductivity of the effluent was less than 900  $\mu\text{S}/\text{cm}$ . The final product was an aqueous suspension of doped rutile having 10 mass % of  $\text{TiO}_2$  nanocrystallites. Samples with urea/ $\text{TiO}_2$  ratios of 0.01, 0.02, 0.03, 0.06, 0.08 w/w, labelled as samples: B, C and D, E, F, were then prepared using the same process by varying the content of added urea. The sample A was prepared using the same process, but without the addition of urea as a dopant.

### 2.2 Characterization of samples

The crystallinity of the particles was examined using X-ray diffraction (XRD) performed on a Cubi X PRO PW

3800 instrument (PANalytical) (Cu-K $\alpha$  radiation ( $\lambda = 1.5418\text{\AA}$ )). In order to acquire the TiO<sub>2</sub> powders for the X-ray powder-diffraction (XRD) measurement, the suspensions were dried at 80 °C, ground and the powder pressed into pellets that were used to perform the measurements.

The average crystallite size was determined using diffraction-peak (100) broadening and Scherrer's formula based on the FWHM (Full Width at Half Maximum) of the XRD peak.

The specific surface areas ( $S_{\text{BET}}$ ) of particles were determined using Tristar 3000, the automatic gas analyser (Micromeritics Instrument Co.).

The morphology and the size of the particles were examined with a transmission electron microscope (TEM, Jeol JEM-2100, Jeol Ltd., Tokyo, Japan). The samples for the TEM specimens were ultrasonically dispersed and the suspensions were collected using carbon-supported copper grids.

The UV-Vis diffuse reflectance spectra were collected on an Agilent-Cary 300 UV-Vis spectrophotometer equipped with an integrating sphere (Varian Inc., USA).

The measurements of the photocatalytic activity were performed in a sealed gas-solid reactor at room temperature and a relative humidity of 60%, utilizing FT-IR spectroscopy (Spectrum BX model Perkin Elmer spectrometer). The model pollutant was isopropanol in the gas phase. During the photocatalytic reaction the isopropanol oxidizes to acetone and subsequently to carbon dioxide and water under UV irradiation (Xe lamp, 300 W). The light imitates the solar spectrum and emits both ultraviolet (UV) and visible (VIS) light. The reactor is at a distance of 4 cm from the lamp. The samples were dried under ambient conditions and prepared by milling 50 mg of the material. To perform the measurements, 20  $\mu\text{L}$  of isopropanol was injected into the system. This volume represents around 2000 ppm of gas phase for the isopropanol in the system. The amount and ratio of isopropanol and the formed acetone were monitored in real time. The evaluation of the photocatalytic activity is based on the acetone-formation kinetics and is given in ppm/h. [33]

The chemical composition of the surfaces was determined by X-ray photoelectron spectroscopy (XPS). XPS analyses were performed with a TFA XPS spectrometer, produced by Physical Electronics Inc., equipped with a monochromated Al-K $\alpha$  X-ray source (1486.6 eV), under ultra-high vacuum ( $10^{-7}$  Pa). Samples in the form of powders were deposited on the adhesive carbon tape. The analyzed area was 0.4 mm in diameter and

the analyzed depth was 3–5 nm. The high-energy resolution spectra were acquired with an energy analyzer operating at a resolution of about 0.6 eV and a pass energy of 29 eV. The XPS spectra were processed with the software MultiPak. Prior to the spectra processing, the same spectra were referenced to the C-C/C-H peak in the C 1s core level at a binding energy of 284.8 eV. The accuracy of the binding energies was about  $\pm 0.2$  eV. Quantification of the surface composition was based on the XPS peak intensities, taking into account the relative sensitivity factors provided by the instrument manufacturer. [38] Three different places were analyzed on each sample and the data were averaged.

### 3 Results and discussion

#### 3.1 The crystallite phase and size of rutile particles

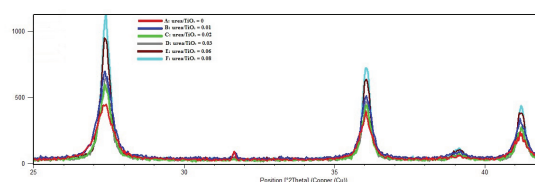


**Figure 1:** XRD patterns of undoped and N-doped TiO<sub>2</sub> samples with different ratios of urea to TiO<sub>2</sub>.

Figure 1 presents the XRD patterns of the samples prepared using a modified hydrothermal process and various ratios of urea to TiO<sub>2</sub>. The presence of specific peaks ( $2\theta = 27.38^\circ, 36.06^\circ, 41.19^\circ$ ) was taken as an attributive indicator of rutile titania. [20, 31] However, no N-derived peak is detected for N-TiO<sub>2</sub>, even when the ratio of urea to TiO<sub>2</sub> was 0.08. It can also be seen from the XRD patterns that the nitrogen-doped samples show more intensive diffraction peaks, indicating a more pronounced crystallinity for the N-doped crystallites.

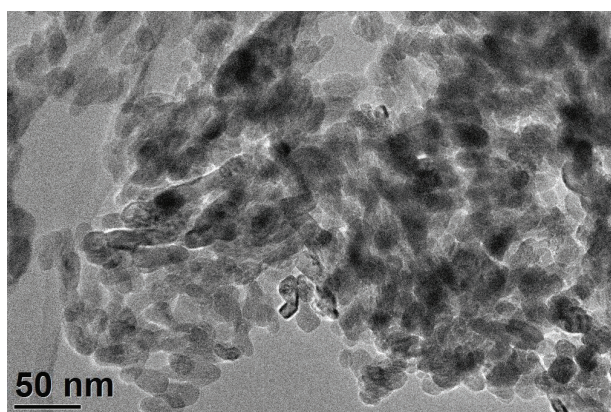
From Table 1 it is clear that the crystallite size increases with the amount of urea in the precursor suspension, i.e., the ratio of urea to polycrystalline TiO<sub>2</sub> (w/w) precursor changes from 0.01 to 0.08. The increase of the crystallite size, for identical hydrothermal conditions, due to a larger amount of urea, can be assigned to the vigorous thermally assisted decomposition reaction of the urea, which enhances the kinetics of mass transport during the dissolution, precipitation and growth of TiO<sub>2</sub> nano-crystallites. Thus, a crystallite-size increase is straightforward and proportional to the amount of urea in the starting suspension. On the other hand, when the addition is a compound that is stable during the hydrothermal synthesis conditions it would, as expected, hinder the crystallite growth and thus decrease

the final crystallite size, which is the case when the suppression of crystallites size is planned.

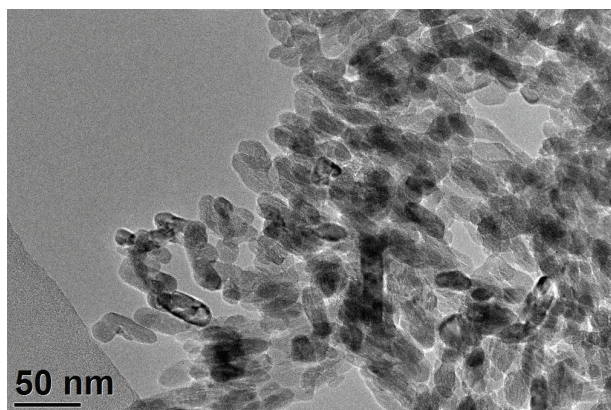
As a consequence, the specific surface areas ( $S_{\text{BET}}$ ) show a steady decrease in parallel with the crystallite size increase. Here, an exception proves sample *B* with a much smaller specific surface regarding the general trend in the sequence, which might be a consequence of the exaggerated crystallite agglomeration. However, in general the morphology of the crystallites follows the general expectation.

**Table 1:** Average crystallite size, specific surface area and band-gap energies for various N-doped  $\text{TiO}_2$  samples.

Sample	Urea/ $\text{TiO}_2$	Specific surface area ( $\text{m}^2/\text{g}$ )	Crystallite size (100) (nm)	Band gap (eV)
A	-	70.1	16.7	3.01
B	0.01	42.5	23.6	3.04
C	0.02	68.1	27.6	3.03
D	0.03	63.7	33.0	3.03
E	0.06	56.9	42.6	3.04
F	0.08	51.0	48.7	3.02



(a)



(b)

**Figure 2:** TEM micrographs of samples prepared with different ratios of urea to  $\text{TiO}_2$ : (a) undoped  $\text{TiO}_2$  and (b) urea/ $\text{TiO}_2 = 0.02$ .

### 3.2 The morphology of the doped $\text{TiO}_2$ particles

The morphologies of the N-doped  $\text{TiO}_2$  are shown in the TEM micrographs of Figure 2. The hydrothermally synthesized, doped, rutile  $\text{TiO}_2$  nanocrystallites have an oval/spherical morphology and are uniform in size. The crystallite sizes observed with the TEM match with those obtained from the Scherrer estimation using the peak broadening of the XRD spectra, which has shown a comparable crystallite size up to a urea/ $\text{TiO}_2$  ratio of 0.03.

On the other hand, the morphologies of samples E and F, prepared at ratios of urea to  $\text{TiO}_2$  of 0.06 and 0.08, respectively, exhibit a larger crystallite size (TEM images not shown).

### 3.3 UV-Vis diffuse reflectance spectra

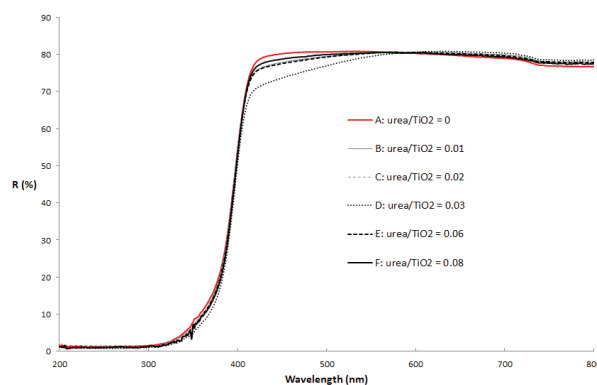


**Figure 3:** UV-Vis reflectance spectra of the undoped  $\text{TiO}_2$  and the  $\text{TiO}_2$  doped with different urea-to- $\text{TiO}_2$  ratios, indicated in the legend.

For the examination of the effects of doping on  $\text{TiO}_2$ , an evaluation of the optical properties is the most appropriate method. UV-Vis spectroscopy and diffuse reflectance spectroscopy were chosen as the techniques for the optical studies of N-doped  $\text{TiO}_2$ . In our work diffuse reflectance spectroscopy was used to examine the visible-light sensitivity. The influence of nitrogen doping on the UV-Vis spectra properties for the rutile  $\text{TiO}_2$  is demonstrated in Figure 3. The reflectivity dependence of the wavelength of the pure  $\text{TiO}_2$  has a typical sharp edge of reflection at around 420–400 nm. Compared with the spectrum of undoped  $\text{TiO}_2$ , the N-doped sam-



ples exhibit a very similar curve progression; however, there is a small but distinguishable shift in the absorbance region of the visible range 400–550 nm. [30, 31, 34] The N-doped samples exhibit a slightly difference in the colour, which could provide a small absorbance in visible region. [41] An exception is observed for the 0.03-doped sample *D*, which shows a more notable red shift. So, based on the intensity of absorption for all the samples we can assume that the nitrogen entered the TiO<sub>2</sub> crystal lattice under the reported hydrothermal condition. The same finding was reported by Huang. [31]

It was reported that the visible-light absorption could be brought about by band-gap narrowing. However, it was also reported that the localized N states within the band gap and the Ti<sup>3+</sup> defects could also provide the absorption red shift. [34, 35] In addition, Hu showed that the band gaps of the doped samples were the same, indicating that N doping did not change the band gap of the TiO<sub>2</sub>. [32] The doping of TiO<sub>2</sub> with N atoms improved its visible-light absorption, increased the numbers of photons in the photocatalytic reaction and thus enhanced the photocatalytic activity in the visible region.

The band-gap energies of the rutile nanocrystallites, estimated using Kubelka–Munk model are summarised in Table 1. [35, 36] The values of the band-gap energies of the doped samples were compared with a control sample (undoped rutile nanocrystallites), which was calculated to have a band gap of 3.01 eV. The calculated value for the undoped rutile nanocrystallites is in agreement with the theoretical value of 3.0 eV for the rutile modification. [37] The results show that the band-gap energies of all the N-doped samples are practically the same as the control sample. A possible explanation is that the visible-light absorption occurs due to the colour centres formed by the N-doping process rather than by a narrowing of the band gap. The research was conducted on various N-doped metal-oxide nanoparticles. The band-gap narrowing does not occur, even for significantly high doping levels, such as 25 % doping. [32, 34]. It can be concluded that the main effect of N doping is a slightly improved absorption at long wavelengths, which enhances the visible photocatalytic activity of these material. It could be concluded that the main effect of N doping is the improved absorption at long wavelengths due to the shallow trap states inside the TiO<sub>2</sub> crystal lattice, which enhances the visible photocatalytic activity of these materials. [22, 24, 25]

### 3.4 Investigation of chemical states of TiO<sub>2</sub> samples

The surface chemical composition and the chemical states of the TiO<sub>2</sub> samples were analyzed by means of XPS. The survey spectra (not shown) are similar and indi-

cate the presence of Ti, O and C in all the samples, while N is visible only in the spectra from the urea-modified TiO<sub>2</sub> samples and confirms a successful treatment. The surface chemical compositions are presented in Table 2. The carbon on the surface of the undoped sample can be related to the surface contamination and the synthesis conditions. For the TiO<sub>2</sub> samples treated with urea a nitrogen signal appeared. The highest nitrogen concentration (0.8 at.%) was observed on the surface of the TiO<sub>2</sub> sample *D* (urea/TiO<sub>2</sub> ratio 0.03). On the sample treated with a higher urea concentration, sample *F* (urea/TiO<sub>2</sub> ratio 0.08), we observed less nitrogen (~ 0.3 at.%). The amount of nitrogen on the surfaces of the analyzed samples correlates with the photocatalytic activity.

High-energy-resolution C 1s, O 1s, N 1s and Ti 2p XPS spectra were acquired to further understand the chemical bonding. In the high-energy-resolution O 1s spectra (not shown here) we were able to observe the presence of two different components by using a fitting procedure. The main contribution is attributed to the Ti-O in the TiO<sub>2</sub> (529.9 eV) and the other minor peak can be ascribed to the surface hydroxyl Ti-OH (531.4 eV). [39] A comparison of the O 1s spectra from the undoped sample with the treated samples shows no major differences.

Nitrogen was only detected in the urea-treated TiO<sub>2</sub> samples. High-energy-resolution N 1s XPS spectra from the undoped TiO<sub>2</sub> and the TiO<sub>2</sub>/urea ratio of 0.03 are shown on Figure 4. The maxima of the N 1s spectra, for all the treated samples, are located at 400 eV, which indicates interstitial nitrogen integrated into the TiO<sub>2</sub> lattice. It is known that the peak at around 400 eV is related to the N-O, N-C or N-N type of bonds. [40]

A comparison of the high-energy-resolution Ti 2p spectra from all the analysed samples is shown in Figure 5. In the acquired Ti 2p spectra a doublet peak is visible, containing both Ti 2p<sub>3/2</sub> and Ti 2p<sub>1/2</sub> components, which appear at 458.6 eV and 464.3 eV, respectively, with 5.7 eV spin-orbital splitting. This corresponds to a Ti<sup>4+</sup> va-

**Table 2:** Surface composition in at. % of the undoped TiO<sub>2</sub> and TiO<sub>2</sub> modified with urea using different concentrations.

Sample	Urea/TiO <sub>2</sub>	C	O	Ti	N
A	-	26.1	52.2	21.7	
B	0.01	21.5	55.8	22.3	0.3
C	0.02	23.4	54.6	21.4	0.7
D	0.03	24.8	53.4	21.1	0.8
E	0.06	20.0	56.7	22.7	0.6
F	0.08	25.2	53.1	21.4	0.3



lence state. The peaks are narrow and no significant differences, like shifting in the binding energy, between the undoped and treated samples were observed (Figure 5).

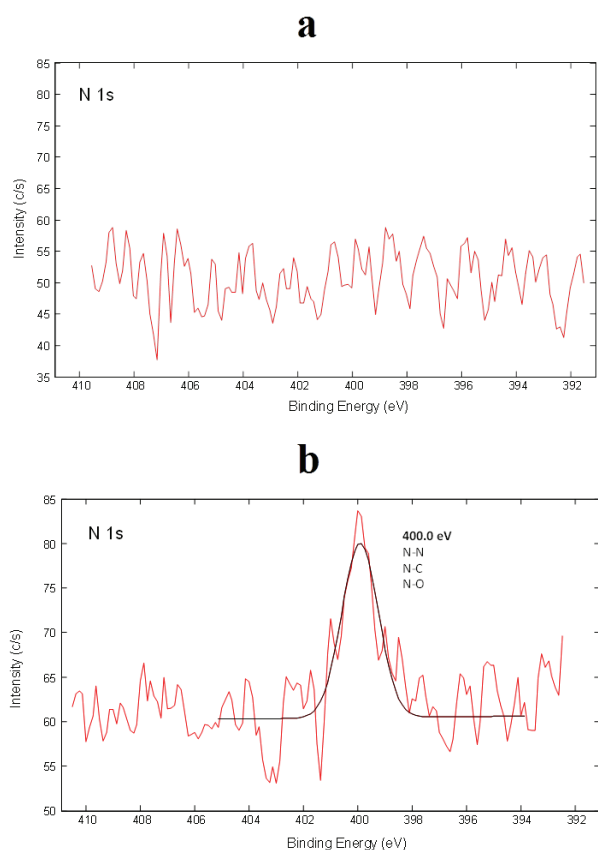


**Figure 4:** N 1s XPS spectrum of undoped TiO<sub>2</sub> (a) and TiO<sub>2</sub> modified with a TiO<sub>2</sub>/urea ratio = 0.03 (b).

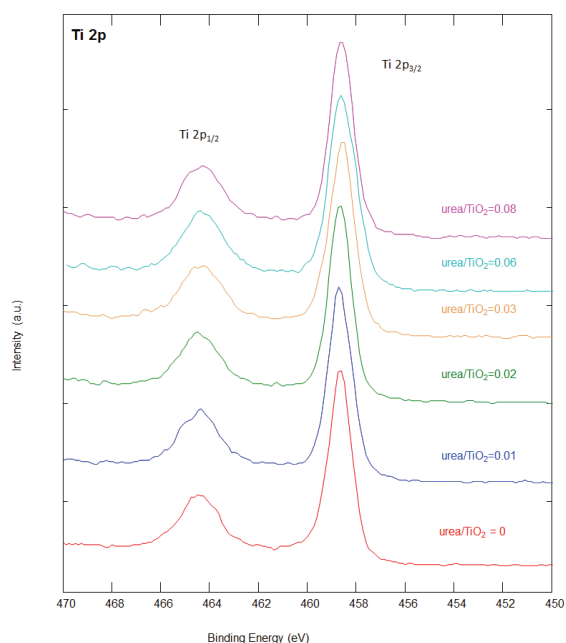
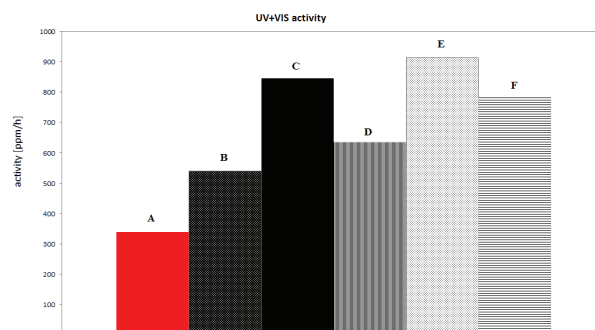


**Figure 5:** XPS spectra of Ti 2p from all the samples.

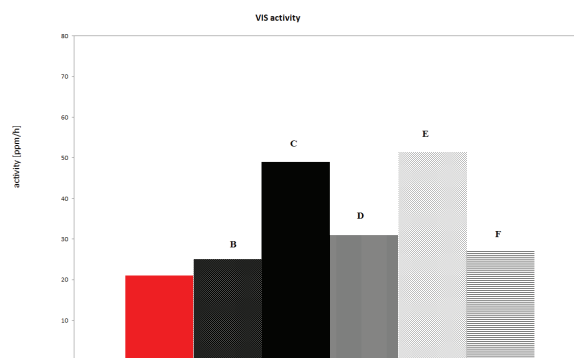
### 3.5 Photocatalytic activity measurements

To evaluate the photocatalytic activity of the undoped and N-doped TiO<sub>2</sub> in the visible range, the degradation of isopropanol under UV+VIS and Vis irradiation was investigated. The results of the photocatalytic activities are presented in Figure 6, based on the acetone-formation kinetics, and are given in ppm/h. As illustrated in Figure 6, different N-doped TiO<sub>2</sub> catalysts differ in the degradation of isopropanol under the same experimental conditions. One can see that i) in general, N-doped TiO<sub>2</sub> samples achieve a higher photocatalytic activity than the undoped TiO<sub>2</sub> samples and ii) the photocatalytic activity increases with the surface-nitrogen concentration.

Among all of the investigated N-doped TiO<sub>2</sub> samples, sample E, with a urea/TiO<sub>2</sub> ratio of 0.06 and a corresponding surface-nitrogen concentration of 0.6 at %, displays the highest photocatalytic efficiency for isopropanol degradation. Nearly the same photocatalytic efficiency was also detected with the sample C, having otherwise a lower urea/TiO<sub>2</sub> ratio of 0.02; however, it exhibits a similar surface-nitrogen concentration of 0.7 at %. In addition, sample E exhibits a lower specific surface area than the sample C with a urea/TiO<sub>2</sub> ratio of



(a)



(b)

**Figure 6:** Photocatalytic activity of undoped TiO<sub>2</sub> and TiO<sub>2</sub> doped with different ratios of urea under a) UV+Vis irradiation and b) Vis irradiation.

0.02, Table 1. Therefore, the high photocatalytic activity of sample C with a surface nitrogen concentration of 0.7 at % is not a consequence of a higher specific surface area, but the result of a high surface-nitrogen concentration. This is in accordance with the general trend that the N centres enhanced the photocatalytic activity in the visible range.

As a result, an increase in the surface area does not automatically produce an increase in the photocatalytic activity, demonstrating that the higher activity is a consequence of a high surface-nitrogen concentration and not of the surface-regulated process. On the other hand, a greater surface area provides more active sites on the TiO<sub>2</sub> surface for the degradation of the organic pollutant. [20, 32]

#### 4 Conclusions

N-doped rutile TiO<sub>2</sub> nanocrystallites that exhibit a strong increase in their photocatalytic activity were successfully prepared using the hydrothermal method. The absorbance of N-TiO<sub>2</sub> in the visible-light region is the most important when concerning the material's application since it can be activated with solar light and thus exhibits an enhanced photocatalytic visible-light activity. The narrowing of the band gap does not occur, indicating that the major effects of N doping are an enhanced absorption at long wavelengths and the hole-trapping sites, which retards the hole–electron recombination and might be useful in enhancing the visible photocatalytic activity of these materials. The maxima of the N 1s spectra, for all the treated samples, indicate that the interstitial nitrogen is integrated into the TiO<sub>2</sub> lattice. The N-doped TiO<sub>2</sub> samples achieved a higher photocatalytic activity in the UV and visible-light regions than the undoped sample. This higher photocatalytic activity has a close correlation with the enhanced visible-light absorption of the doped samples.

#### 5 Acknowledgment

This work is partially financially supported by the Ministry of Education, Science and Sport of the Republic of Slovenia under the contract 34/2013-SOF. The authors declare that there is no conflict of interest regarding the publication of this paper.

#### 6 References

1. M. R. Hoffmann, S. T. Martin, W. Choi, D. W. Bahnemann, Environmental applications of semiconductor photocatalysis, *Chem. Rev.*, 1995, 95(1), 69-96
2. A. Fujishima, T. N. Rao, D. A. Tryk, Titanium dioxide photocatalysis, *Journal of Photochemistry and Photobiology C: Photochemistry*, 2000, 1, 1-21
3. M. Palaez, N. T. Nolan, S. C. Pillai, M. K. Seery, P. Falaras, A. G. Kontos, P. S. M. Dunlop, J. W. J. Hamilton, J. A. Byrne, K. O'Shea, M. H. Entezari, D. D. Dionysiou, A review on the visible light active titanium dioxide photocatalysts for environmental applications, *Applied Catalysts B: Environmental*, 2012, 125, 331-349
4. X. Chen, S. S. Mao, Titanium dioxide nanomaterials: synthesis, properties, modifications and applications, *Chem. Rev.*, 2007, 107, 2891-2959
5. D. P. Macwan, P. N. Dave, S. Chatuverdi, A review on nano-TiO<sub>2</sub> sol gel synthesis and its applications, *J. Mater. Science*, 2011, 46, 3669-3686
6. S. Banerjee, D. D. Dionysiou, S. C. Pillai, Self-cleaning applications of TiO<sub>2</sub> by photo-induced hydrophilicity and photocatalysis, *Applied Catalysis B: Environmental*, 2015, 176-177, 396-428
7. W. Shen, C. Zhang, Q. Li, W. Zhang, L. Cao, J. Ye, Preparation of titanium dioxide nano particle modified photo catalytic self-cleaning concrete, *Journal of cleaner production*, 2015, 87, 762-765
8. S. M. Gupta, M. Tripathi, A review of TiO<sub>2</sub> nanoparticles, *Chinese Science Bulletin*, 2011, 56 (16), 1639-1657
9. S. Banerjee, S. C. Pillai, P. Falaras, K. E. O'Shea, J. A. Byrne, D. D. Dionysiou, New insights into the mechanism of visible light photocatalysis, *The Journal of Physical Chemistry Letters*, 2014, 5, 2543-2554
10. H. Feng, M. Zhang, L. E Yu, Hydrothermal synthesis and photocatalytic performance of metal-ions doped TiO<sub>2</sub>, *Applied Catalysis A: General*, 2012, 413-414, 238-244
11. G. Liu, L. Wang, H. Gui Hang, H.-M. Cheng, G. Q. Lu, Titania-based photocatalysts-crystal growth, doping and heterostructuring, *Journal of Materials Chemistry*, 2010, 20, 831-843
12. A. Zaleska, Doped-TiO<sub>2</sub>: A review, *Recent Patents on Engineering*, 2008, 2, 157-164
13. S. G. Kumar, L. G. Devi, Review on modified TiO<sub>2</sub> photocatalysis under UV/visible light selected results and related mechanisms on interfacial charge carrier transfer dynamics, *The Journal of Physical Chemistry A*, 2011, 115, 13211-13241
14. M. V. Dozzi, E. Selli, Doping TiO<sub>2</sub> with p-block elements: Effects on photo catalytic activity, *Journal*

- of Photochemistry and Photobiology C: Photochemistry, 2013, 14, 13-28
15. Y. Dai, K. Yang, B. Huang, S. Han, Theoretical study of N-doped TiO<sub>2</sub> rutile crystals, *J. Phys. Chem B*, 2006, 110, 24011-24014
  16. S. Rehman, R. Ullah, A. M. Butt, N.D. Gohar, Strategies of making TiO<sub>2</sub> and ZnO visible light active, *Journal of Hazardous Materials*, 2009, 170, 560-569
  17. M. Fernandez-Garcia, A. Martinez-Arias, J. C. Conesa, Visible light – responsive titanium oxide photocatalysts: preparation based on chemical method, *Environmentally Benign Photocatalysts*, Nanostructure Science and Technology, 2010
  18. C. Burda, Y. Lou, X. Chen, A. C. S. Samia, J. Stout, J. L. Gole, Enhanced nitrogen doping in TiO<sub>2</sub> nanoparticles, *Nano Letters*, 2003, 3 (8), 1049-1051
  19. M. Long, W. Cai, Visible light responsive TiO<sub>2</sub> modification with non-metal elements, *Frontiers of Chemistry in China*, 2011, DOI 10.1007/s11458-011-0243-8
  20. J. Ananpattarachai, P. Kajitvichyanukul, S. Seraphin, Visible light absorption ability and photocatalytic oxidation activity of various interstitial N-doped TiO<sub>2</sub> prepared from different nitrogen dopants, *Journal of Hazardous Materials*, 2009, 168, 253-261
  21. Z. L. Zeng, First principle study on the structural and electronic properties of N atoms doped rutile TiO<sub>2</sub> of oxygen vacancies, *Advances in Materials Science and Engineering*, 2014, 2015, 10 pages
  22. M. Batzill, E. H. Morales, U. Diebold, Influence of nitrogen doping on the defect formation and surface properties of TiO<sub>2</sub> rutile and anatase, *Physical Review Letters*, 2006, 96 (2), 026103 (4)
  23. B. Ohtani, Titania photocatalysis beyond recombination: A critical review, *Catalysts*, 2013, 3, 942-953
  24. T. Ihara, M. Miyoshi, Y. Iriyama, O. Matsumoto, S. Sugihara, Visible light active titanium dioxide photocatalyst realized by an oxygen-deficient structure and by nitrogen doping, *Applied Catalysis B: Environmental*, 2003, 42, 403-409
  25. G. Liu, X. Wang, Z. Chen, H. M. Cheng, G. Q. Lu, The role of crystal phase in determining photocatalytic activity of nitrogen doped TiO<sub>2</sub>, *Journal of Colloid and Interface Surface*, 2009, 329, 331-338
  26. C. Di Valentin, G. Pacchioni, A. Selloni, Origin of the different photocatalytic activity of N-doped anatase and rutile TiO<sub>2</sub>, *Physical review B*, 2004, 70, 085116
  27. O. Diwald, T. L. Thompson, E. G. Goralski, S. D. Walck, J. T. Yates, Jr., The effect of nitrogen ion implantation on the photocatalytic activity of TiO<sub>2</sub> rutile single crystals, *J. Phys. Chem B*, 2004, 108, 52-57
  28. J. Lin, J. C. Yu, D. Lo, S. K. Lam, Photocatalytic activity of rutile Ti<sub>1-x</sub>Sn<sub>x</sub>O<sub>2</sub> solid solutions, *Journal of Catalysis*, 1999, 183, 368-372
  29. H. Liu, L. Gao, Codoped rutile TiO<sub>2</sub> as a new photocatalyst for visible light irradiation, *Chemistry Letters*, 2004, 33 (6), 730-731
  30. F. Peng, L. Cai, L. Huang, H. Yu, H. Wang, Preparation of nitrogen-doped titanium dioxide with visible light photocatalytic activity using a facile hydrothermal method, *Journal of Physics and Chemistry of Solids*, 2008, 69, 1657-1664
  31. D. Huang, S. Liao, S. Quan, L. Liu, Z. He, J. Wan, W. Zhou, Synthesis and characterization of visible light responsive N-TiO<sub>2</sub> mixed crystal by a modified hydrothermal process, *Journal of Non-Crystalline Solids*, 2008, 354, 3965-3975
  32. S. Hu, A. Wang, X. Li, H. Löwe, Hydrothermal synthesis of well-dispersed ultrafine N-doped TiO<sub>2</sub> nanoparticles with enhanced photocatalytic activity under visible light, *Journal of Physics and Chemistry of Solids*, 2010, 71, 156-162
  33. M. Tashibi, U. Lavrenčič Štangar, A. Sever Škapin, A. Ristić, V. Kaučič, N. Novak Tušar, Titania-containing mesoporous silica powders: Structural properties and photocatalytic activity towards isopropanol degradation, *Journal of Photochemistry and photobiology A: Chemistry*, 2010, 216, 167-178
  34. X. Qiu, C. Burda, Chemically synthesized nitrogen doped metal oxide nanoparticles, *Chemical Physics*, 2007, 339, 1-10
  35. M. D'Arienzo, R. Scotti, L. Wahba, C. Battocchio, E. Bemporad, A. Nale, F. Morazzoni, Hydrothermal N-doped TiO<sub>2</sub>: Explaining photocatalytic properties by electronic and magnetic identification of N active sites, *Applied Catalysis B: Environmental*, 2009, 93, 149-155
  36. S. Valencia, J.M. Marin, G. Restrepo, Study of the bandgap of synthesized titanium dioxide nanoparticles using the sol-gel method and a hydrothermal treatment, *The Open Materials Science*, 2010, 4, 9-14
  37. M. Landmann, E. Rauls, W.S. Schmidt, The electronic structure and optical response of rutile, anatase and brookite TiO<sub>2</sub>, *J. Phys.: Condens. Matter*, 2012, 24 195503
  38. J. F. Moulder, W. F. Stickle, P. E. Sobol, K. D. Bomben, "Handbook of X-Ray Photoelectron Spectroscopy", Physical Electronics Inc., Eden Prairie, Minnesota, USA, 1995
  39. J. Yu, H. Yu, B. Cheng, M. Zhou, X. Zhao, Enhanced photocatalytic activity of TiO<sub>2</sub> powder (P 25) by hydrothermal treatment, *Journal of Molecular Catalysis A: Chemical*, 2006, 253, 112-118
  40. Y. Nosaka, M. Matsushita, J. Nishino, A. Y. Nosaka, Nitrogen doped titanium dioxide photocatalysts

for visible response prepared by using organic compounds, *Science and Technology of Advanced Materials*, 2005, 6, 143-148.

41. P. He, J. Tao, X. Hunag, J. Xue, Preparation and photocatalytic antibacterial property of nitrogen doped TiO<sub>2</sub> nanoparticles, *Sol-Gel Sci. Technol.* 2013, 68, 213-218

Arrived: 23. 05. 2017

Accepted: 01. 08. 2017





# *Doktorske disertacije na področju mikroelektronike, elektronskih sestavnih delov in materialov v Sloveniji v letu 2016*

## *Doctoral theses on Microelectronics, Electronic Components and Materials in Slovenia in 2016*

*Univerza v Ljubljani / University of Ljubljana*

*Fakulteta za elektrotehniko / Faculty of Electrical Engineering*

1	Avtor Author	Vladimir Furlan
	Naslov Title	<b>Frekvenčno nastavljiva antena z visokim izkoristkom na feroelektriku</b> Frequency-agile, highly-efficient antenna on ferroelectric substrate
	Mentor Supervisor	prof. dr. Matjaž Vidmar
2	Avtor Author	Mario Trifković
	Naslov Title	<b>Zmanjšanje preklopnega šuma v sinhronih digitalnih vezjih na osnovi razporejanja signala ure</b> Switching noise reduction in synchronous digital circuit based on clock skew scheduling
	Mentor Supervisor	prof. dr. Drago Strle
3	Avtor Author	Tine Dolžan
	Naslov Title	<b>Napredne membranske mikročrpalke s piezoelektričnim vzbujanjem na osnovi PDMS elastomera</b> Advanced piezoelectrically actuated membrane micropumps based on PDMS elastomer
	Mentor Supervisor	dr. Danilo Vrtačnik
4	Avtor Author	Matija Podhraški
	Naslov Title	<b>Integrirani mikrosenzorski sistemi z mikrotuljavicami</b> Integrated microsensor systems with microcoils
	Mentor Supervisor	prof. dr. Janez Trontelj

5	Avtor Author	Uroš Nahtigal
	Naslov Title	<b>Integrirani barvni senzor svetlobe z velikim dinamičnim območjem</b> Integrated color light sensor with high dynamic range
	Mentor Supervisor	prof. dr. Drago Strle
6	Avtor Author	Luka Bogataj
	Naslov Title	<b>Zasnova in izvedba visokostabilnega optoelektronskega oscilatorja</b> Design and implementation of a highly-stable optoelectronic oscillator
	Mentor Supervisor	prof. dr. Matjaž Vidmar
7	Avtor Author	Blaž Kirn
	Naslov Title	<b>Zmogljivost sončnih fotonapetostnih elektrarn skozi življenjski cikel</b> Life cycle performance of solar photovoltaic power plants
	Mentor Supervisor	prof. dr. Marko Topič

*Univerza v Mariboru / University of Maribor*

*Fakulteta za elektrotehniko, računalništvo in informatiko/Faculty of Electrical Engineering and Computer Science*

1	Avtor Author	Janko Horvat
	Naslov Title	<b>Regulirana prožilna stopnja za močnostne tranzistorje</b> Controlled gate driver for power transistors
	Mentor Supervisor	prof. dr. Miro Milanovič
2	Avtor Author	Aleksandar Dodić
	Naslov Title	<b>Korekcijski faktorji koeficientov digitalnih struktur pri spremembi frekvence vzorčenja</b> Correctio factors of digital structure coefficients at sampling frequency change
	Mentor Supervisor	prof. dr. Zmago Brezočnik

3	Avtor Author	Uroš Pešovič	
	Naslov Title	Model verjetnosti pogreškov IEEE 802.15.4 brezžičnega prenosa pri so-kanalski interferenci in šumu ozadja <b>Error probability model for IEEE 802.15.4 wireless transmission with co-channel interference and background noise</b>	
	Mentor Supervisor	prof. dr. Peter Planinšič	

4	Avtor Author	Marijan Španer	
	Naslov Title	<b>Superkondenzator in energijska izkoriščenost baterijsko napajanih vozil</b> Supercapacitor and energy efficiency of battery powered vehicles	
	Mentor Supervisor	prof. dr. Karel Jezernik	

*Mednarodna podiplomska šola Jožefa Stefana / Jožef Stefan*

*International Postgraduate School*

1	Avtor Author	Rok Rudež	
	Naslov Title	Razvoj debeloplastne oksidne elektronske keramike <b>Development of thick-film oxide-based electronic ceramics</b>	
	Mentor Supervisor	prof. dr. Slavko Bernik	

2	Avtor Author	Mojca Presečnik	
	Naslov Title	Mikrostrukturne in termoelektrične lastnosti keramike tipa p v sistemu Ca-Co-O <b>Microstructural and thermoelectric characteristics of p-type ceramics in the Ca-Co-O system</b>	
	Mentor Supervisor	prof. dr. Slavko Bernik	

3	Avtor Author	Tina Bakarič		
	Naslov Title	Priprava porozne keramike $\text{Pb}(\text{Zr}_{0.53}\text{Ti}_{0.47})\text{O}_3\text{Pb}(\text{Zr}_{0.53}\text{Ti}_{0.47})\text{O}_3$ z načrtovano mikrostrukturno in oblikovanje debelih plasti z brizgalnim tiskanjem <b>Processing of porous <math>\text{Pb}(\text{Zr}_{0.53}\text{Ti}_{0.47})\text{O}_3\text{Pb}(\text{Zr}_{0.53}\text{Ti}_{0.47})\text{O}_3</math> ceramics with a designed microstructure and patterning of thick films by inkjet printing</b>		
	Mentor Supervisor	Dr. Danjela Kuščer Hrovatin	Somentor Co-Supervisor	Dr. Tadej Rojac



4	Avtor Author	Jitka Hreščak		
	Naslov	Sinteza in karakterizacija nedopirane in s stroncijem dopirane keramike na osnovi kalijevega natrijevega niobata		
	Title	<b>Synthesis and characterization of undoped and strontium-doped potassium sodium niobate ceramics</b>		
	Mentor Supervisor	Dr. Andreja Benčan	Somentor Co-Supervisor	Prof. dr. Barbara Malič
5	Avtor Author	Marko Vrabelj		
	Naslov	Raziskave elektrokaličnega pojava v polikristaliničnem relaksorskem feroelektriku $0.9\text{Pb}(\text{Mg}_{1/3}\text{Nb}_{2/3})\text{O}_3-0.1\text{PbTiO}_3$ $0.9\text{Pb}(\text{Mg}_{1/3}\text{Nb}_{2/3})\text{O}_3-0.1\text{PbTiO}_3$		
	Title	<b>Investigations of the electrocaloric effect in the polycrystalline <math>0.9\text{Pb}(\text{Mg}_{1/3}\text{Nb}_{2/3})\text{O}_{3-0.1}\text{PbTiO}_{30.9}\text{Pb}(\text{Mg}_{1/3}\text{Nb}_{2/3})\text{O}_{3-0.1}\text{PbTiO}_3</math> relaxor ferroelectric</b>		
	Mentor Supervisor	Prof. dr. Barbara Malič		
6	Avtor Author	Tanja Pečnik		
	Naslov	Mikrostruktura in dielektrične lastnosti tankih plasti $(\text{Ba,Sr})\text{TiO}_3$ $(\text{Ba,Sr})\text{TiO}_3$ , pripravljenih s sintezo v raztopini		
	Title	<b>Microstructure and dielectric properties of solution-derived <math>(\text{Ba,Sr})\text{TiO}_3</math> <math>(\text{Ba,Sr})\text{TiO}_3</math> thin films</b>		
	Mentor Supervisor	Prof. dr. Barbara Malič		
7	Avtor Author	Evgeniya Khomyakova		
	Naslov	Integracija debelih plasti bizmutovega ferita na keramične in kovinske podlage z metodo sitotiska		
	Title	<b>Integration of screen-printed bismuth ferrite thick films onto ceramic and metal substrates</b>		
	Mentor Supervisor	Dr. Andreja Benčan Golob	Somentor Co-Supervisor	Dr. Tadej Rojac

Bold font is used for the original title of the thesis (and language in which the thesis is written), normal font for title translation.

# MIDEM 2017

## 53<sup>rd</sup> INTERNATIONAL CONFERENCE ON MICROELECTRONICS, DEVICES AND MATERIALS WITH THE WORKSHOP ON MATERIALS FOR ENERGY CONVERSION AND THEIR APPLICATIONS



### Announcement and Call for Papers

October 4<sup>th</sup> – 6<sup>th</sup>, 2017

Jožef Stefan Institute, Ljubljana, Slovenia

**ORGANIZER: MIDEM Society** - Society for Microelectronics, Electronic Components and Materials, Ljubljana, Slovenia

**CONFERENCE SPONSORS:** Slovenian Research Agency, Republic of Slovenia; IMAPS, Slovenia Chapter; IEEE, Slovenia Section;

#### GENERAL INFORMATION

The 53<sup>rd</sup> International Conference on Microelectronics, Electronic Components and Devices with the Workshop on Materials for Energy Conversion and Their Applications continues a successful tradition of the annual international conferences organised by the MIDEM Society, the Society for Microelectronics, Electronic Components and Materials. The conference will be held at **Jožef Stefan Institute, Ljubljana, Slovenia, leading Slovenian scientific research institute, from OCTOBER 4<sup>th</sup> – 6<sup>th</sup>, 2017.**

#### Topics of interest include but are not limited to:

- Workshop focus: Materials for Energy Conversion and Their Applications:
- Electrocalorics and Thermoelectrics
- Novel monolithic and hybrid circuit processing techniques,
- New device and circuit design,
- Process and device modelling,
- Semiconductor physics,
- Sensors and actuators,

- Electromechanical devices, Microsystems and nanosystems,
- Nanoelectronics
- Optoelectronics,
- Photonics,
- Photovoltaic devices,
- New electronic materials and applications,
- Electronic materials science and technology,
- Materials characterization techniques,
- Reliability and failure analysis,
- Education in microelectronics, devices and materials.

#### ABSTRACT AND PAPER SUBMISSION:

Prospective authors are cordially invited to submit up to 1 page abstract before **May 1<sup>st</sup>, 2017**. Please, identify the contact author with complete mailing address, phone and fax numbers and e-mail address. After notification of acceptance (**June 15<sup>th</sup>, 2017**), the authors are asked to prepare a full paper version of six pages maximum. Papers should be in black and white. Full paper deadline in PDF and DOC electronic format is: **August 31<sup>st</sup>, 2017**.

#### IMPORTANT DATES:

Abstract deadline: **May 1<sup>st</sup>, 2017** (1 page abstract or full paper)


Notification of acceptance: **June 15<sup>th</sup>, 2017**

Deadline for final version of manuscript: **August 31<sup>st</sup>, 2017**

Invited and accepted papers will be published in the conference proceedings.

Detailed and updated information about the MIDEM Conferences is available at

<http://www.midem-drustvo.si/> under Conferences.

 **Jožef Stefan  
 Institute  
 Ljubljana, Slovenija**





# *Boards of MIDEM Society | Organi društva MIDEM*

## *MIDEM Executive Board | Izvršilni odbor MIDEM*

### **President of the MIDEM Society | Predsednik društva MIDEM**

Prof. Dr. Marko Topič, University of Ljubljana, Faculty of Electrical Engineering, Slovenia

### **Vice-presidents | Podpredsednika**

Prof. Dr. Barbara Malič, Jožef Stefan Institute, Ljubljana, Slovenia

Dr. Iztok Šorli, MIKROIKS, d. o. o., Ljubljana, Slovenija

### **Secretary | Tajnik**

Olga Zakrajšek, UL, Faculty of Electrical Engineering, Ljubljana, Slovenija

### **MIDEM Executive Board Members | Člani izvršilnega odbora MIDEM**

Darko Belavič, In.Medica, d.o.o., Šentjernej, Slovenia

Dr. Slavko Bernik, Jožef Stefan Institute, Ljubljana, Slovenia

Dr. Miha Čekada, Jožef Stefan Institute, Ljubljana, Slovenia

Prof. DDr. Denis Donlagič, UM, Faculty of Electrical Engineering and Computer Science, Maribor, Slovenia

Prof. Dr. Leszek J. Golonka, Technical University Wroclaw, Poland

Dr. Vera Gradišnik, Tehnički fakultet Sveučilišta u Rijeci, Rijeka, Croatia

Leopold Knez, Iskra TELA d.d., Ljubljana, Slovenia

mag. Mitja Koprivšek, ETI Elektroelementi, Izlake, Slovenia

Prof. Dr. Miran Mozetič, Jožef Stefan Institute, Ljubljana, Slovenia

Prof. Dr. Janez Trontelj, UL, Faculty of Electrical Engineering, Ljubljana, Slovenia

Dr. Danilo Vrtačnik, UL, Faculty of Electrical Engineering, Slovenia

## *Supervisory Board | Nadzorni odbor*

Prof. Dr. Franc Smole, UL, Faculty of Electrical Engineering, Ljubljana, Slovenia

prof. dr. Drago Strle, UL, Faculty of Electrical Engineering, Ljubljana, Slovenia

Igor Pompe, Ljubljana, Slovenia

## *Court of honour | Častno razsodišče*

Emer. Prof. Dr. Jože Furlan, Slovenia

Dr. Marko Hrovat, Slovenia

Dr. Miloš Komac, Slovenia



**Informacije MIDE**

*Journal of Microelectronics, Electronic Components and Materials*

ISSN 0352-9045

*Publisher / Založnik:*

*MIDEM Society / Društvo MIDE*

*Society for Microelectronics, Electronic Components and Materials, Ljubljana, Slovenia*

*Strokovno društvo za mikroelektroniko, elektronske sestavne dele in materiale, Ljubljana, Slovenija*

**[www.midem-drustvo.si](http://www.midem-drustvo.si)**